

# Monday Morning, October 19, 2015

## Energy Frontiers Focus Topic

Room: 211B - Session EN+AS+EM+NS+SE+SS+TF-MoM

## Solar Cells I

Moderator: Jason Baxter, Drexel University, Chintalapalle Ramana, University of Texas at El Paso

8:20am EN+AS+EM+NS+SE+SS+TF-MoM1 **Elevated Temperature Phase Stability of CZTS-Se Thin Films for Solar Cells**, *E. Chagarov, K. Sardashti*, University of California at San Diego, *D.B. Mitzi*, Duke University, *R.A. Haight*, IBM T.J. Watson Research Center, *Andrew C. Kummel*, University of California at San Diego

Density-functional theory simulations of CZTS, CZTSe and CZTS<sub>0.25</sub>Se<sub>0.75</sub> photovoltaic compounds have been performed to investigate stability of CZTS<sub>0.25</sub>Se<sub>0.75</sub> alloy vs. decomposition to CZTS, CZTSe and other secondary compounds. The Gibbs energy for vibration contribution was estimated by calculating phonon spectra and thermodynamic properties at finite temperatures. It was demonstrated that CZTS<sub>0.25</sub>Se<sub>0.75</sub> alloy is stabilized not by enthalpy of formation but by vibration and mixing contributions to the Gibbs energy. A set of phase diagrams was built in multidimensional space of chemical potentials at 300K and 900K temperatures to demonstrate alloy stability and boundary compounds at various chemical conditions. The Gibbs energy gain/loss for several decomposition reactions was calculated as a function of temperature with/without Cu/Zn intermixing and vibration contributions to the Gibbs energy demonstrating CZTS<sub>0.25</sub>Se<sub>0.75</sub> that even defect-free (no Cu/Zn intermixing) CZTS<sub>0.25</sub>Se<sub>0.75</sub> can be stable at typical processing temperatures.

8:40am EN+AS+EM+NS+SE+SS+TF-MoM2 **Chemical and Electrical Characterization of Polycrystalline CZTS,Se and CIGS,Se Grain Boundaries by NanoAuger and Kelvin Probe Force Microscopy (KPFM)**, *Kasra Sardashti*, UC San Diego, *P.D. Antunez*, *R.A. Haight*, IBM T.J. Watson Research Center, *A.C. Kummel*, UC San Diego

Polycrystalline Copper-zinc-tin-sulfide/selenide (CZTS,Se) compounds have received wide research interest due to their potential as inexpensive absorber materials composed of earth-abundant elements. Photovoltaic devices fabricated on CZTS,Se have reached conversion efficiencies of 12.6 %. One of the key parameters to further boost the conversion efficiency is to control the concentration of recombination sites at the surface, secondary phase interfaces and in the grain boundaries. To determine the presence of secondary phases on the surface and composition of grain boundaries, this work has employed Auger nanoprobe electron spectroscopy (NanoAuger) with 8nm lateral resolution combined with high resolution ambient Kelvin Probe Force Microscopy (KPFM) with dual-lock-in setup. NanoAuger was performed in planar and cross-sectional modes on CZTS,Se surfaces before and after top surface oxide removal by NH<sub>4</sub>OH clean. Elemental maps before and after NH<sub>4</sub>OH clean show Sn-/O-rich and Cu-poor grain boundaries suggesting that grain boundaries are terminated by tin-oxide (SnOx). Secondary phases such as SnSe and ZnSe were observed in the cross-sectional maps. Kelvin probe force microscopy (KPFM) on the cleaned surfaces showed that SnOx-terminated grain boundaries have 80-200 mV larger work function than grains, resulting in upward band bending accompanied by the large valence band offset between the SnOx and CZTS,Se lead to relatively large energy barriers for both electrons and holes to travel into the grain boundaries and recombine. Comparison with the elemental maps for CIGSe (with device efficiencies as high as 18%) revealed the absence of the grain boundary oxide passivation.

9:40am EN+AS+EM+NS+SE+SS+TF-MoM5 **Spin Coating Thin Film CZTS for Efficient, Low-Cost Solar Cells on Flexible Glass Substrates**, *D. Kava*, *J. Galindo*, *C.O. Sana*, *S. Shahriar*, *Deidra Hodges*, University of Texas at El Paso

Photovoltaic's contribution to energy production continues to grow as costs continue to decrease. As silicon cells approach their limits, other materials are emerging. The development of Cu<sub>2</sub>ZnSnS<sub>4</sub> (CZTS) thin film solar cells using non-vacuum liquid-based spin coating techniques have been previously investigated. The focus of this paper is the optimization of p-type CZTS thin film solar cells onto flexible substrates. Flexible solar panel costs are higher than their traditional counterparts. CZTS currently reports only a 3.2% efficiency on flexible glass, while the record for CZTS on non-flexible substrates is 12.6%. The cells are created using a single solution ink sol-gel method. All metals are dissolved in a single step prior to deposition onto substrates (nickel foil and coming willow glass) as a thin film. Corning

Willow glass is a new material introduced recently to the market, while nickel is an inexpensive flexible reflective foil. The Corning Willow glass is coated with a molybdenum layer as a reflective back contact layer. By using a single step and a solution deposition method, lower production cost are achievable. For thin film deposition, we used a non-vacuum spin coater (WS650 spin processor, Laurell Technologies) with an optimized spin coat programming. Annealing took place under vacuum in a RTP furnace while time, temperature and ramp functions were varied. The other layers of the device consists of cadmium sulfide n-type window layer and a zinc oxide doped with aluminum transparent top contact layer. Characterization and analysis of the thin films were performed using Raman spectroscopy, scanning electron microscope (Zeiss NEON 40), X-ray diffraction (Philipps X'Pert), profilometer (Veeco Dektak 150), UV-Vis-NIR Spectrophotometer (Cary 5000), Hall Effect measurement system (HMS3000) and 4 point probe (Lucas Labs) measurements. Results show CZTS thin film solar cells on flexible glass is obtainable.

10:00am EN+AS+EM+NS+SE+SS+TF-MoM6 **Band Gap Profile of Cu(In,Ga)(Se,S) 2 Thin Films via High-Resolution Reflection Electron Energy Loss Spectroscopy**, *Sung Heo*, *H.I. Lee*, *J.B. Park*, *G.S. Park*, Samsung Advanced Institute of Technology, Republic of Korea, *D.H. Lee*, *J.G. Nam*, Samsung, Republic of Korea, *H.J. Kang*, Chungbuk National University, Republic of Korea, *B.D. Choi*, Sungkyunkwan University, Republic of Korea

Cu(In,Ga)Se<sub>2</sub> (CIGS)-based solar cells was investigated with an aim of enhancing cell performance because these cells provided high conversion efficiency at relatively low cost. The efficiency of CIGS cells has recently approached 19.7% at small sizes. In general, Cu(In<sub>1-x</sub>Ga<sub>x</sub>)(Se<sub>1-y</sub>S<sub>y</sub>)<sub>2</sub>(CIGSS) composition profiles are double-graded, and they can improve the open-circuit voltage (V<sub>OC</sub>) and the efficiency of solar cells because band gaps increase toward both the surface (i.e., with the increase of sulfur) and the bottom (i.e., with the increase of gallium). It is important to accurately measure the band gap at the top and the bottom of the CIGSS cell. Nevertheless, the band gap profile measurement of the CIGSS as a function of depth is challenging.

In this study, we obtained the depth profile of the CIGSS cell using the quantitative Auger Electron Spectroscopy method, for which the relative sensitivity factor was corrected using the inductively coupled plasma-atomic emission spectrometry (ICP-AES) method. We also measured the band gap directly using high-resolution reflection electron energy loss spectroscopy (HR-REELS) with a monochromatic electron gun, which has low electron energy at 300 eV.

For the direct measurement of a band gap profile, HR-REELS spectra were obtained as a function of depth during Ar ion sputtering at 3.0 kV. The band gap profile shows a double-graded band gap as a function of depth. The band gap values are 1.32 eV at the surface (E<sub>g1</sub>), 1.08 eV at the depth between 0.3 and 0.7μm (E<sub>g min,position</sub>), and 1.50 eV at the depth of about 2.2 μm (E<sub>g2</sub>), respectively. Our findings suggest a new analytical method which directly determines the band gap profile as function of depth.

10:40am EN+AS+EM+NS+SE+SS+TF-MoM8 **Spatial Atmospheric ALD of Zinc Oxysulfide Buffer Layers for CIGS Solar Cells**, *C. Frijters*, *P.J. Bolt*, *P. Poedt*, *Andrea Illiberi*, Solliance/TNO, Netherlands

Copper Indium Gallium di-Selenide (CIGS) solar cells are a promising approach in photovoltaic technology, having low production costs, high conversion efficiencies (> 20 %), as well as the possibility to manufacture them on flexible substrates. State-of-the-art in CIGS solar cells manufacturing is to use a stack of CdS, intrinsic ZnO (i-ZnO) and an Al-doped ZnO TCO on top of the CIGS film. Replacement of CdS by a non-toxic Cd-free layer with wider band gap (> 2.4 eV) would *a*) decrease the production cost by avoiding the expensive treatment of toxic wastes and *b*) increase the overall cell efficiency by enhancing the quantum efficiency in the blue range. Moreover, the use of a "soft" and highly conformal deposition technique is preferred to improve the electrical properties of the buffer layer/CIGS interface.

In this paper we present spatial atmospheric atomic layer deposition of a Zn(O,S) buffer layer as CdS replacement for CIGS solar cells. Spatial ALD is emerging as an industrially scalable deposition technique at atmospheric pressure which combines the advantages of temporal ALD, i.e. excellent control of film composition and uniformity on large area substrates, with high growth rates (up to nm/s). Films are grown by sequentially exposing the substrate to oxygen and sulfur precursors (H<sub>2</sub>O, H<sub>2</sub>S) and the zinc metal precursor (i.e., DEZn). By controlling the kinetics of surface reactions between evaporated precursors and reactive sites at the film surface, the composition of Zn(O,S) can be precisely tuned. The incorporation of S into

ZnO results in a bowing of the band gap in the range from 3.3 eV (ZnO) to 2.7 (S/O+S ~ 0.5) and 3.4 eV (ZnS), as measured by spectrophotometry. The morphology of the Zn(O<sub>x-1</sub>S<sub>x</sub>) films varies from polycrystalline (for 0<x<30 and 70<x<100) to amorphous (30<x<70), as measured by X-ray diffraction. CIGS solar cells with a Spatial ALD Zn(O,S) buffer layer show an increased spectral response around 400 nm compared to solar cells with a CdS buffer layer. The solar cells with the Zn(O,S) buffer layer had an efficiency of 15.9 %, compared to 15.5 % for the reference solar cells with a CdS buffer layer.

11:00am **EN+AS+EM+NS+SE+SS+TF-MoM9 Deep Level Electron Traps in Epitaxial CuInSe<sub>2</sub> Probed using Photo-Modulated X-ray Photoelectron Spectroscopy, Nicole Johnson**, University of Illinois at Urbana-Champaign, *P. Aydogan*, Bilkent University, Turkey, *A. Rockett*, University of Illinois at Urbana-Champaign, *S. Suzer*, Bilkent University, Turkey

Performance in a variety of electronic devices is largely controlled by minority carrier charge capture on point defects. To date there is no experimental method to directly identify these point defects in a chemically specific fashion. Photo-modulated X-ray Photoelectron Spectroscopy (XPS) utilizes the chemical and charge sensitivity of XPS to identify changes in peak shape due to changing atomic charge state from capture of light-generated minority carriers. Epitaxial thin films of CuInSe<sub>2</sub> (CIS) were chosen as a case study for this technique because their defect chemistry is still relatively unknown as compared to traditional solar cell materials. The 500-1000nm thick films were grown by a hybrid sputtering and evaporation technique on GaAs(001) substrates at 600-700°C. Aligned surface morphology features matching the substrate geometry in scanning electron microscopy (SEM) images indicate epitaxial growth, which was confirmed by x-ray diffraction (XRD). A layer of CdS was deposited on the CIS via chemical bath deposition to protect the CIS surface from oxidation in storage and to duplicate the heterojunction used in solar cells. Prior to loading in the XPS, the CdS was etched off to expose a Cd doped CIS surface for analysis. The photo-modulated XPS used monochromatic AlK $\alpha$  x-rays with a 532 nm laser as the illumination source. Under illumination, each film constituent was observed to exhibit unique binding energy shifts. Based on their peak shifts relative to the surface photovoltage profile, Cd and In were found to be right at the surface while Cu and Se were deeper into the film, consistent with a Cd-doped, In-rich surface. The technique is therefore shown to provide a chemically-sensitive depth profile non-destructively that can be obtained even on a relatively rough sample. Additionally, shape changes in the Se 3d doublet spectra indicate electron capture in a deep trap state that is likely due to cation vacancies. Measurements at varying temperatures indicate air-induced surface recombination states are passivated by annealing at 80C, allowing the surface photovoltage to persist. At 230C, an irreversible change happens in the surface properties such that the surface photovoltage gets much smaller and reverses sign. This work was supported by a joint NSF-TUBITAK collaborative research project (NSF Grant No: 1312539 TUBITAK Grant No: 212M051).

11:20am **EN+AS+EM+NS+SE+SS+TF-MoM10 The Role of ZnTe Buffer Layers on the Performance and Stability of CdTe Solar Cells, Jiaojiao Li**, Colorado School of Mines, *A. Abbas*, Loughborough University, UK, *D.M. Meysing*, *J.D. Beach*, *D.R. Diercks*, Colorado School of Mines, *M.O. Reese*, *T.M. Barnes*, National Renewable Energy Laboratory, *C.A. Wolden*, Colorado School of Mines, *J.M. Walls*, Loughborough University, UK

The use of ZnTe buffer layers at the back contact of CdTe solar cells has been credited with contributing to recent improvements in both record cell efficiency and module stability. To better understand the underlying reasons high resolution transmission microscopy (HR-TEM) and atom probe tomography (APT) were used to study the evolution of the back contact region before and after rapid thermal activation of this layer. During activation the 150 nm ZnTe layer, initially nanocrystalline and homogenous, transforms into a bilayer structure consisting of an amorphous region in contact with CdTe characterized by significant Cd-Zn interdiffusion, and a crystalline layer that shows evidence of grain growth and twin formation. This graded layer may passivate interface defects and account for the improved open circuit voltage and fill factor that accompanies the RTP activation step. Copper, co-evaporated uniformly within ZnTe, is found to segregate dramatically after rapid thermal activation, either collecting near the ZnTe|Au interface or forming Cu<sub>x</sub>Te clusters in CdTe at defects or grain boundaries near the interface. Further examination of the Cu<sub>x</sub>Te clusters revealed that they are encased in a thin layer of Zn, and it is postulated that this structure may limit the extent of diffusion into CdTe and play an important role in device stability.

11:40am **EN+AS+EM+NS+SE+SS+TF-MoM11 The Performance and Durability of Broadband Anti-Reflection Coatings for Thin Film CdTe Solar Cells, G. Womack, P.M. Kaminski, John Walls**, Loughborough University, UK

Light reflection from the glass surface of a photovoltaic (PV) module is a significant source of energy loss for crystalline silicon and all types of thin film PV devices. The reflection at the glass and air interface accounts for ~4% of the total energy. Single layer anti-reflection coatings using magnesium fluoride or porous silica with sufficiently low refractive index have been reported but these are only effective over a narrow range of wavelengths. In this paper we report on the design, deposition and testing of multilayer broadband anti-reflection coatings that reduce the weighted average reflection over the wavelength range used by thin film CdTe devices to ~1.22% resulting in a useful 3.6% increase in photocurrent. In this study we have used multilayer stacks consisting of silica and zirconia layers deposited using a reactive magnetron sputtering process. Details of the stack design, sputtering process parameters and the optical and micro-structural properties of the layers are provided.

Thin film CdTe devices pose a special problem because the anti-reflection coating is applied to one side of the glass while device layers are deposited directly on to the opposite glass surface in the superstrate configuration. In thin film CdTe production, the glass is exposed to high temperature processes during the absorber deposition and during the cadmium chloride activation treatment. If glass pre-coated with a broadband anti-reflection coating is to be used then the coating must withstand temperatures of up to ~550°C. Surprisingly, our studies have shown that multilayer silica/zirconia anti-reflection coatings on soda lime glass remain unaffected by temperatures up to 600 °C at which point mild crazing is observed. This is an important observation since it means that low cost glass which is pre-processed with a broadband anti-reflection coating by glass manufacturers is potentially useable in thin film CdTe module production

## Plasma Science and Technology

Room: 210A - Session PS+SE-MoM

### Atmospheric Pressure Plasma Processing I

Moderator: François Reniers, Université Libre de Bruxelles

9:00am **PS+SE-MoM3 Modeling Non-Equilibrium Plasma Jets at Atmospheric Pressure, Leanne Pitchford**, CNRS and University of Toulouse 3, France

INVITED

The considerable recent interest in 'microdischarges' (discharges in small, spatially-confined geometries) is largely due to their remarkable stability. That is, stable, non-thermal, atmospheric-pressure plasmas can be generated and maintained in electric discharges in small geometries. Further interest in microdischarges is due to the fact that 'plasma jets', initiated from microdischarges operating with pulsed or RF excitation and with an axial helium flow, can propagate in the helium jet which extends some distance (cm's) into the open air past the exit of the microdischarge, while causing little or no increase in the gas temperature. Fast imaging shows that most of the light emitted by the plasma jet is produced in a small 'plasma bullet' that propagates in the helium jet at speeds of some tens of kilometers per second. The possibility to generate non-thermal plasmas in ambient air has incited considerable interest for applications in the biomedical field, among others.

Modeling is an important tool for developing an understanding of microdischarges. It has been shown that the plasma jet is very similar to a cathode streamer (ionization wave) guided by air surrounding the more easily-ionized helium jet. This talk will focus on results from two-dimensional fluid modeling. The properties of the streamer in helium and of the plasma channel behind the streamer head as a function of parameters such as the electrode geometry and voltage pulse waveform will be discussed. We will focus in particular on the the configuration developed by the team of Vincent Puech at the Laboratoire de Physique des Gaz et des Plasmas at the Université Paris Sud in Orsay. This configuration consists of a dielectric tube, some mm in diameter, with an inner, hollow electrode (high voltage) and an outer ring electrode (ground). A discharge is initiated inside the dielectric tube by applying high voltage pulse (some kV's with 100 ns risetime) to the inner electrode. Models reproduce the main features of plasma jets observed experimentally, and quantities such as energy deposition in the plasma jet itself can be obtained from modeling, whereas it is much more difficult to extract such information from experiments. More work is needed to quantify the plasma chemistry triggered by the plasma jet and in particular of the influence of the remnant excitation and ionization on the properties of the subsequent plasma jets.

9:40am **PS+SE-MoM5 Vacuum Ultraviolet Polymer Etching and Modification by a Remote Atmospheric Pressure Plasma Jet.** *Andrew Knoll, P. Luan, E.A.J. Bartis, G.S. Oehrlein*, University of Maryland, College Park

In this study, we investigate the etching mechanism of atmospheric pressure plasma jet (APPJ) treated poly(methyl methacrylate)-based 193 nm photoresist polymer and polystyrene-based 248 nm photoresist polymer using *in situ* ellipsometry to monitor film thickness and refractive index in real time. The kHz-driven, two-ring electrode APPJ used in this work operated with low admixtures of O<sub>2</sub> and N<sub>2</sub> to Ar feed gas flowed at 2 slm. Additionally, we used attenuated total reflection Fourier transform infrared spectroscopy (ATR-FTIR) and x-ray photoelectron spectroscopy to characterize the surface modifications post treatment. With pure argon feed gas, we observed etching of the photoresist polymers even when the visible plume is not in direct contact with the polymer surface. This etching rate is sensitive to the Ar gas flow rate and local gas environment. APPJ treatments were compared to a surface microdischarge source with a O<sub>2</sub>/N<sub>2</sub> gas flow added but no etching was seen for that source. Furthermore, the etching was shown to be directional by placing a grounded mesh directly over the sample during treatment. No etching was seen without direct line of sight from source to sample. Optical filters were used to investigate the effect of high energy photons on polymer etching and modification. When a MgF<sub>2</sub> filter with a 114 nm cutoff wavelength is placed directly over the sample, etching still occurs. When a sapphire filter with cutoff wavelength of 142 nm is used, no etching is seen. Ar<sub>2</sub>\* excimer species are known to be created in atmospheric pressure plasma and emit photons at 128 nm. Vacuum-ultraviolet (VUV)-induced etching is further supported by experiments that show that etching increases in nitrogen environments compared to oxygen environments as oxygen more effectively absorbs VUV radiation. ATR-FTIR of treated samples shows comparable bulk modifications with or without MgF<sub>2</sub> filter over the sample. These results are consistent with photoresists treated with VUV from low pressure plasma. APPJs are sources of a variety of reactive chemical species which can be used for numerous industrial and medical applications. While the VUV effect of APPJ sources on biodeactivation has been investigated<sup>1,2</sup>, polymer etching has not been seen prior to this work. The authors gratefully acknowledge financial support by US Department of Energy (DE-SC0001939) and National Science Foundation (PHY-1415353).

<sup>1</sup> Lackmann, J. W., et al. (2013). Journal of the Royal Society Interface 10(89).

<sup>2</sup> Schneider, S., et al. (2011). Journal of Physics D-Applied Physics 44(29).

10:00am **PS+SE-MoM6 Recent Development and Application of Low Cost and Portable Atmospheric Pressure Microplasma Generation Devices.** *Cheng-Che Hsu, P.K. Kao, Y.J. Yang, Y.H. Huang*, National Taiwan University, Taiwan, Republic of China

Low cost and portable atmospheric pressure microplasma generation devices (MGD) offer great opportunities in several applications when plasmas in-situ, on-demand and/or in-field are desired. This study presents the development of simple and economical MGD made on copper clad laminate. This MGD can be sustained using a portable power supply (less than two pounds) that can be powered by 12V-batteries. Matching of the device capacitance with power arrangement is extremely important for this power to properly function. The use of such devices for gas conversion, selective area treatment, and fabrication microfluidic paper-based analytical device ( $\mu$ PAD) on demand will be presented. Such a MGD can be used to perform surface patterning of hydrophobic/hydrophilic contrasts with sub-mm spatial resolution and to effectively decompose CO<sub>2</sub> into CO. In addition, using this MGD to fabricate  $\mu$ PADs is demonstrated. With a proper design of the MGD electrode geometry,  $\mu$ PADs with 500  $\mu$ m-wide flow channels can be fabricated within 1 min and with a cost of less than \$USD 0.1/device. We then test the  $\mu$ PADs by performing quantitative colorimetric assays and establish calibration charts for detection of glucose and nitrite. The results show a linear response to glucose assay for 1 -50 mM and nitrite assay for 0.1 -5 mM. This low cost and portable MGD can be used for in-field diagnostic tests, and is believed to bring impact to the field of biomedical analysis, environmental monitoring, and food safety survey.

10:40am **PS+SE-MoM8 Experimental Study of Micron-Scale, Field Emission-Driven Microplasmas.** *Mihai Bilici, C.R. Boyle*, Case Western Reserve University, *D.B. Go*, University of Notre Dame, *R.M. Sankaran*, Case Western Reserve University

Microplasmas are miniaturized versions of low-pressure, direct-current glow discharges that can be stabilized at high pressures, up to and exceeding atmospheric pressure. In particular, atmospheric-operation has resulted in interest in their applications in materials processing, environmental remediation, and ionization sources for mass spectrometry. At these small electrode dimensions, new properties emerge that may also

be important for fundamental study. For example, as the electrode gap is reduced to less than  $\sim 10$   $\mu$ m, gas breakdown has been found to deviate from Paschen's law due to an additional contribution to electron emission from field emission. In addition, field emission leads to a "pre-breakdown" regime where gas-phase electrons can interact with the background gas and even ionize the gas before complete breakdown occurs. However, to date there is little experimental evidence of these field-emission driven microplasmas to support theoretical predictions.

Here, we present a study of field-emission driven microplasmas using a custom-built tip-to-plane microplasma setup with environmental control and nanometer-resolution stepper motor control. The tip electrode is mounted on a micro-positioning system (Model Newport SMC100CC) and approaches a planar substrate in precise increments of  $\sim 20$  nm. The entire setup is housed in an acrylic glove box that can be pumped to  $\sim 100$  Torr and backfilled with a desired gas such as argon. The gap between the electrodes and subsequent breakdown of the gas is imaged by a camera system (Model Dino-Lite AM4115ZTL). Current-voltage (I-V) measurements are obtained at each gap by a programmable voltage supply and a current monitoring system.

Our results show that at small gaps of less than  $\sim 10$   $\mu$ m, the I-V curves exhibit a turn-on voltage, defined as the voltage where a current above the noise of  $\sim 100$  nA is measured, followed by a non-linear, approximately exponential increase in current with applied voltage. The turn-on voltage is found to increase with gap from  $\sim 1$ -10  $\mu$ m. Above  $\sim 10$   $\mu$ m, the non-linear regime is not observed and the I-V curve abruptly increases as a result of complete gas breakdown. To analyze the results, we have fitted the I-V curves at small gaps to Fowler-Nordheim theory, confirming that the current is produced from field emission. However, a major challenge is reproducibility of the data because of tip and substrate damage which continually affect field-emission behavior. We will discuss these issues and show our efforts to connect the experimental data to existing theory.

Keywords: microplasmas, field emission

11:00am **PS+SE-MoM9 Precise Energy and Temperature Measurements in Dielectric Barrier Discharges (DBD) at Atmospheric Pressure.** *B. Nisol*, Groupe des Couches Minces (GCM) and Department of Engineering Physics, Polytechnique Montréal, Canada, *M. Archambault-Caron, H. Gagnon*, Groupe des Couches Minces (GCM) and Department of Engineering Physics, Polytechnique Montréal, *S. Lerouge*, Department of Mechanical Engineering, École de Technologie Supérieure (ETS), and Centre de Recherche du CHUM (CRCHUM), *Michael Wertheimer*, Groupe des Couches Minces (GCM) and Department of Engineering Physics, Polytechnique Montréal, Canada

A specially designed dielectric barrier discharge (DBD) cell and associated equipment has been used to carry out precise measurements of electrical energy,  $E_g$ , dissipated per discharge cycle of the applied a.c. voltage,  $V_a$ , over the frequency range  $5 \leq f \leq 50$  kHz. Twin pairs of several different dielectric materials (2.54 cm diameter discs, thicknesses = 2.0 or ca. 0.1 mm) with relative permittivities between  $2.1 \leq K \leq 9.5$  were used as dielectric barriers in DBDs of four different gases: He, Ne, Ar and N<sub>2</sub>. Much of the work relates to the study of atmospheric pressure glow discharge (APGD) plasma in flowing He gas; five separate thermometers (including fiber-optic probes immune to high voltage and high-frequency electromagnetic fields) have enabled us to perform a detailed calorimetric (heat balance) investigation in He APGD, believed to be the first of its kind. Fair agreement in the overall energy balance, which includes vacuum ultraviolet (VUV) light emission, lends strong support to the validity of both measurements and methodology. The latter includes refined algorithms that permit rapid data acquisition and processing. The present results are compared with literature, allowing several important conclusions / recommendations to emerge.

Next, we turn to the particular case of DBD in Ar in a pilot-scale reactor dedicated to deposition of thin organic films (PECVD) for biomedical applications. We have found that transfer of data from the small to the large (near 50-fold greater surface area) apparatus has been very successful, and that we can now precisely measure the amount of energy ( $\Delta E_g$ ) consumed in a particular PECVD process. We finish by presenting specific example reactions and link energy measurements with physico-chemical characteristics of deposits.

11:20am **PS+SE-MoM10 Plasma-Induced Conductivity in Dielectrics: A Study of Dielectric Barrier Discharges, Floran Peeters\***, FOM Institute DIFFER, Netherlands, *R.F. Rumphorst*, Eindhoven University of Technology, Netherlands, *M.C.M. van de Sanden*, FOM Institute DIFFER, Netherlands

In plasma devices, the surfaces bounding the plasma form an integral part of the system. Despite this, surfaces are generally described as perfect absorbers for electrons and ions, without any further consideration of potentially relevant processes taking place within the material. Dielectric surfaces, for instance, are treated as single capacitive elements, providing a wall potential. For most discharges this model is sufficiently accurate, but if the characteristic dimensions of dielectric and plasma are very dissimilar, such as in etched micro- and nanostructures or if the discharge itself is non-uniform, understanding the build-up of surface charges and their subsequent behavior becomes of paramount importance.

In our work, we use a typical non-uniform discharge to investigate the plasma-dielectric interaction: the dielectric barrier discharge (DBD) in filamentary mode. Filamentary DBDs can be described by an equivalent circuit which assumes discharging occurs uniformly across the surface, i.e. by treating the dielectric as a single continuous capacitive element. This is counter-intuitive, since DBD actually consists of many spatially and temporally separated, transient microdischarges. Studying the electrical characteristics of DBDs more closely, using both conventional  $Q-V$  diagrams combined with a circuit designed to record the transferred charge per filament, we developed an improved electrical model of the DBD. An extension to the electrical model for DBDs introduced by Manley in 1943, our model explicitly takes into account the localized nature of the discharge. Using this model, we find that individual filaments are always roughly equivalent; irrespective of the phase or amplitude of the applied voltage. We show that this leads to limited control over the chemical processing efficiency of DBD. The fundamental cause of the insensitivity of the discharge to the applied voltage is identified as the constant redistribution of surface charge on the dielectric.

Further investigation reveals that this redistribution of charge does not occur via the gas-phase of the residual plasma, as is often assumed, but is likely the result of excess charge carriers being introduced into the dielectric by the discharge. We provide corroborative evidence that these excess charge carriers, involving free electron and hole densities not normally seen in high-band gap materials, provide a boost to the conductivity of the material in locations affected by the plasma. As shown here for a DBD, this plasma-induced conductivity can have a significant effect on the behavior of the discharge and should be considered in any models of plasma involving dielectric surfaces.

11:40am **PS+SE-MoM11 Fabrication of Flexible, Electrically-Conductive Features by Microplasma Reduction of Cation-Cross-Linked Polyacrylic Acid (CCL-PAA) Films, Souvik Ghosh\***, *R. Yang, P.X.-L. Feng, C.A. Zorman, R.M. Sankaran*, Case Western Reserve University

Patterned metal formation on substrates is typically achieved by subtractive methods. Recently, additive manufacturing techniques have emerged that can selectively deposit materials to produce patterned structures. Examples of additive methods include ink-jet, aerosol, and screen printing. A common feature of all of these approaches is the ink, a solution of stabilized colloidal metal nanoparticles that is deposited onto an arbitrary substrate. Removal of the organic stabilizers is often carried out by annealing at high temperatures (>200 °C) to produce electrically conductive features, limiting what substrates can be used. There are also challenges with deposition of the inks associated with the viscosity and adhesion of the inks to the substrate.

An alternative approach to fabricating patterned metals in polymers is *in situ* reduction of metal containing polymers. Here, we present an atmospheric-pressure microplasma process for the selective reduction of metal ions in polymer films to produce flexible, electrically-conductive metal patterns [1]. The films are made from polyacrylic acid (PAA) which reversibly cross links with metal cations such as silver ( $Ag^+$ ). The films are subsequently exposed to a microplasma formed in a flowing argon gas on a two-dimensional scanning stage to “write” a desired pattern. Characterization of the films by X-ray diffraction (XRD) confirms that the  $Ag^+$  is reduced to crystalline Ag after exposure to the microplasma. Further materials analysis by scanning electron microscopy (SEM) and energy dispersive spectroscopy (EDX) show that reduction leads to the formation of Ag nanoparticles whose size and morphology depend on the exposure conditions (i.e. plasma current, scanning rate, etc.). Cross-sectional characterization of the films shows that the reduction does not penetrate through the film bulk. We suggest that the  $Ag^+$  diffuses to the film surface during reduction, leading to a near-surface layer of reduced crystalline Ag with bulk resistivity  $\sim 1$  m $\Omega$ -cm. Stretchable films have been produced by

casting PAA- $Ag^+$  films on top of a polydimethylsiloxane (PDMS) substrate, followed by exposure to the microplasma. Dynamic mechanical analysis (DMA) of the multilayer films yield a breaking force value of >3 MPa and the films can be stretched to >100%. Electrical measurements are performed on the films as a function of strain to analyze the change in resistivity with stretching. We will also present our recent efforts to reduce the size of the patterns, which is currently  $\sim 100$   $\mu$ m, to approximately 10  $\mu$ m by incorporating stencil masks.

[1] S. Ghosh *et al.*, ACS Appl. Mater. Interfaces **6**, 3099 (2014).

## Advanced Surface Engineering

Room: 212A - Session SE+AS+NS+TR-MoM

### Nanostructured Thin Films and Coatings

Moderator: Robert Franz, Montanuniversität Leoben,

Austria, Andrey Voevodin, Air Force Research Laboratory

8:20am **SE+AS+NS+TR-MoM1 Reactively Sputter Deposited Ternary AlN-based Coatings, Joerg Patscheider**, Empa, Switzerland, *E. Lewin*, Uppsala University, Sweden

The protection of surfaces against preventing premature failure by abrasion-resistant nitride coatings has been investigated and put into daily operation ever since. Despite these efforts, the wide range of available protective coatings cannot be used, when glass and other optically transparent materials have to be protected due to the opacity of transition metal nitrides for visible light. For such applications thin films based on Al-A-N with additions of elements from group 14 with A = Si, Ge or Sn are attractive candidate materials, as their transparency in the visible range opens new opportunities of applications. Furthermore, the addition of these elements causes the formation of solid solutions and of nanocomposites, leading to enhanced hardness in the case of A = Si and Ge. Once nanocomposites are formed, enhanced hardness of more than 30 GPa is observed in the case of Al-Si-N and more than 20 GPa for Al-Ge-N and Al-Sn-N. The choice of the additional A element allows for the preparation of highly transparent coatings for the case of Si and the control of color in the range from yellow to red by tuning of the UV absorption edge in the case of Ge and Sn. The role of deposition conditions and their implications on the structure these ternary nitride coatings will be discussed.

8:40am **SE+AS+NS+TR-MoM2 Mo<sub>2</sub>BC Coatings for Metal Forming: Interactions between Tool Surface and Aluminium by Theory and Experiment, Jochen Schneider**, RWTH Aachen University, Germany, *H. Bolvardi*, Oerlikon Balzers, Liechtenstein, *D. Music*, RWTH Aachen University, Germany

Low temperature growth strategies for Mo<sub>2</sub>BC coatings are reviewed and initial theoretical and experimental data pertaining to the applicability of these coatings during forming of Al based alloys are discussed. A Mo<sub>2</sub>BC(040) surface was exposed to O<sub>2</sub>. The gas interaction was investigated using *ab initio* molecular dynamics and x-ray photoelectron spectroscopy (XPS) of air exposed surfaces. The calculations suggest that the most dominating physical mechanism is dissociative O<sub>2</sub> adsorption whereby Mo - O, O - Mo - O and Mo<sub>2</sub> - C - O bond formation is observed. To validate these results, Mo<sub>2</sub>BC thin films were synthesised utilizing high power pulsed magnetron sputtering and air exposed surfaces were probed by XPS. MoO<sub>2</sub> and MoO<sub>3</sub> bond formation is observed and is consistent with here obtained *ab initio* data. Additionally, the interfacial interactions of O<sub>2</sub> exposed Mo<sub>2</sub>BC(040) surface with an Al nonamer is studied with *ab initio* molecular dynamics to describe on the atomic scale the interaction between this surface and Al to mimic the interface present during cold forming processes of Al based alloys. The Al nonamer was disrupted and Al forms chemical bonds with oxygen contained in the O<sub>2</sub> exposed Mo<sub>2</sub>BC(040) surface. Based on the comparison of here calculated adsorption energy with literature data, Al - Al bonds are shown to be significantly weaker than the Al - O bonds formed across the interface. Hence, Al-Al bond rupture is expected for a mechanically loaded interface. Therefore the adhesion of a residual Al on the native oxide layer is predicted. This is consistent with experimental observations. The data presented here may also be relevant for other oxygen containing surfaces in a contact with Al or Al based alloys for example during forming operations.

9:00am **SE+AS+NS+TR-MoM3 Molecular Dynamics Simulations of TiN/TiN(001) Growth, Daniel Edström**, *D.G. Sangiovanni, V. Chirita, L. Hultman*, Linköping University, Sweden, *J.E. Greene, I. Petrov*, University of Illinois at Urbana Champaign

The Modified Embedded Atom Method (MEAM) interatomic potential within the classical Molecular Dynamics (MD) framework enables realistic,

\* Coburn & Winters Student Award Finalist

large-scale simulations of important model materials such as TiN. As a step toward understanding atomistic processes controlling the growth of TiN on a fundamental level, we perform large-scale simulations of TiN/TiN(001) deposition using a TiN MEAM parameterization which reproduces experimentally-observed surface diffusion trends, correctly accounts for Ehrlich barriers at island step edges [1], [2], and has been shown to give results in excellent qualitative and good quantitative agreement with Ab Initio MD based on Density Functional Theory (DFT) [3], [4]. 85% of a monolayer of TiN is deposited on 100x100 atom TiN(001) substrates at a rate of 1 Ti atom per 50 ps, resulting in simulation times of 212.5 ns. The TiN substrate is maintained at a typical epitaxial growth temperature, 1200 K during deposition using N:Ti flux ratios of 1:1, 2:1, and 4:1 and incident energies of 2 and 10 eV to probe the effects of N<sub>2</sub> partial pressure and substrate bias on TiN(001) growth modes. We observe nucleation of Ti<sub>x</sub>N<sub>y</sub> molecules; N<sub>2</sub> desorption; the formation, growth and coalescence of mixed <100>, <110>, and <111> faceted islands; as well as intra- and interlayer mass transport mechanisms. For equal flux ratios at 2 eV incidence energy, islands begin to form atop existing islands at coverages ≥ 0.25 ML, leading to 3D multilayer growth. Increasing the N:Ti flux ratio shifts the growth mode to layer-by-layer growth and changes the stoichiometry from under- to over-stoichiometric. We discuss the implications of these results on thin film growth and process tailoring. Our classical MD predictions are supported and complemented by DFT-MD simulations.

[1] D. G. Sangiovanni, D. Edström, L. Hultman, V. Chirita, I. Petrov, and J. E. Greene, "Dynamics of Ti, N, and TiN<sub>x</sub> (x=1–3) ad-molecule transport on TiN(001) surfaces," *Phys. Rev. B*, vol. 86, no. 15, p. 155443, 2012.

[2] D. Edström, D. G. Sangiovanni, L. Hultman, V. Chirita, I. Petrov, and J. E. Greene, "Ti and N adatom descent pathways to the terrace from atop two-dimensional TiN/TiN(001) islands," *Thin Solid Films*, vol. 558, pp. 37–46, 2014.

[3] D. G. Sangiovanni, D. Edström, L. Hultman, I. Petrov, J. E. Greene, and V. Chirita, "Ab initio and classical molecular dynamics simulations of N<sub>2</sub> desorption from TiN(001) surfaces," *Surf. Sci.*, vol. 624, pp. 25–31, 2014.

[4] D. G. Sangiovanni, D. Edström, L. Hultman, I. Petrov, J. E. Greene, and V. Chirita, "Ti adatom diffusion on TiN(001): Ab initio and classical molecular dynamics simulations," *Surf. Sci.*, vol. 627, pp. 34–41, 2014.

9:20am **SE+AS+NS+TR-MoM4 Stress Design of Multi-layered Coatings, Wolfgang Seidl**, Christian Doppler Laboratory for Application Oriented Coating Development at the Institute of Materials Science and Technology, Vienna University of Technology, 1040 Vienna, Austria, *M. Arndt*, Oerliko Balzers, Oerlikon Surface Solutions AG, 9496 Balzers, Liechtenstein, *P. Polcik*, Plansee Composite Materials GmbH, 86983 Lechbruck am See, Germany, *P.H. Mayrhofer*, Vienna University of Technology, Austria

Residual stresses within physical vapour deposited coatings are a major concern, as they are often the origin of failure and delamination. Furthermore, stresses, which typically scale with the thickness, limit the thickness of the coating. With increasing stresses, the interface region is increasingly stressed and weakened, promoting delamination and buckling effects. CrN coatings are known to allow for moderate compressive or even tensile stresses, enabling the preparation of coating thicknesses above 20 μm. Although CrN coatings exhibit excellent tribological and wear resistance properties, their thermal stability with respect to Cr-N dissociation is limited to 900 °C, which limits their application field. However, several applications require higher thermal stability in combination with relatively thick ceramic coatings. Therefore, we study in detail the requirements to develop nitride-based coatings with thicknesses exceeding 20 μm.

The residual stresses of arc evaporated TiN, CrN, TiAlN, CrAlN, and TiAlTaN coatings, prepared with an industrial sized coating plant (Balzers Oerlikon INNOVA), are investigated as a function of their thicknesses by measuring the curvature of one-side coated Si(100) cantilevers. Based on these studies we developed multilayer arrangements of TiN/CrN, TiAlN/CrN, TiAlN/CrAlN, and TiAlTaN/CrAlN thick coatings. Their stresses are designed through variations in bilayer period and arrangements of the cathodes at the sidewalls of the industrial chamber.

The individual coatings and multilayers are additionally investigated with respect to growth morphology (by cross sectional scanning electron microscopy), hardness and indentation moduli (by nanoindentation), structure and crystallographic phases (by X-ray diffraction).

9:40am **SE+AS+NS+TR-MoM5 Atomistic Guided Development of Hard Coatings and Thin Films for Severe Applications, Paul Mayrhofer**, Vienna University of Technology, Austria **INVITED**

This work summarizes recent developments on applying thin film structure and architecture concepts to hard coatings for optimized performance in various application fields.

The hardness of materials rapidly decreases at elevated temperatures as generally the density of structural defects, such as point defects, dislocations, and grain boundaries, decreases. Additional strengthening can be provided by age-hardening mechanisms, which originate from decomposition-processes of supersaturated phases to form new obstacles retarding plastic deformation. Furthermore important is the resistance against oxidation and corrosive attack.

By using ab initio calculations and sophisticated experimental methods we will have a detailed insight into various mechanisms responsible for excellent mechanical strength, thermal stability and oxidation resistance properties of Ti–Al–N based hard coatings. For these materials we will also compare the effect of various architecture and alloying concepts with e.g., Y, Zr, Hf, Nb, and Ta.

Another important class of hard coatings is based on the material systems CrN and Cr–Al–N. After a short overview on ab initio and experimental studies in comparison to their sister system Ti–Al–N, we will have a small excursion on the influence of architecture – using the model system CrN/AlN multilayers or their superlattices – on the mechanical properties and especially fracture toughness. Furthermore, based on recent ab initio investigations suggesting that the inherent fracture toughness of CrN can be increased by alloying with Mo or W, we will explore in detail the challenges in studying Cr–Mo–N or Cr–W–N materials by ab initio and experiments.

The various thin film structure and architecture concepts allow the utilization of multifunctional properties facilitating the development of next generation's hard coatings.

10:40am **SE+AS+NS+TR-MoM8 Crystallographic Stabilization of δ-WC Thin Films by Alloying with B, using Reactive Magnetron Sputtering of W in Trimethylboron (CH<sub>3</sub>)<sub>3</sub>B. Hans Högborg, L. Tengdelius, M. Samuelsson, G. Greczynski, F. Eriksson, L. Hultman**, Linköping University, Sweden

The hardness, oxidation resistance, and high temperature stability of hexagonal δ-WC (B<sub>h</sub>) in cemented carbide is a key component in metal cutting. Such a property envelop suggest many potential thin film applications. However, the literature shows that thin film growth of δ-WC by for instance magnetron sputtering is complicated typically resulting in the deposition of films containing the phase γ-WC (B<sub>l</sub>) with a carbon content lower than nominal, i.e. WC<sub>1-x</sub>. As the properties of this phase is less favorable compare to those of δ-WC, growth of WC<sub>1-x</sub> must be avoided in an optimized thin film material. In this study, we attempt to promote the formation of δ-WC films by alloying with B. Our hypothesis is that the preferred growth of WC<sub>1-x</sub> films depends on the preference of C to occupy octahedral sites found in the B<sub>l</sub> structure and where the larger B atom may act to stabilize the B<sub>h</sub> structure by better filling out the larger trigonal prism interstitials in this structure. We use reactive magnetron sputtering of W, using trimethylboron (CH<sub>3</sub>)<sub>3</sub>B (TMB) as C and B precursor. The 5 min depositions were carried on Si(100) substrates in a Kr plasma held at a constant pressure of 0.53 Pa. The gaseous TMB was introduced close to the substrates. The influence of TMB flow, ranging from 1-10 mln, was studied for a growth temperature of 500 °C. Also, the influence of growth temperature, from room temperature to 900 °C, was investigated for a constant TMB flow of 10 mln. X-ray photoelectron spectroscopy shows that the content of B and C scales with the flow into the plasma with no B and ~3 at.% C at 1 mln and 6.5 at.% B and 17.8 at.% C at 10mln. In contrast, temperatures up to 600 °C show no impact on the B and C content in the films, while higher temperatures give a solid state reaction with the substrate. X-ray diffraction shows broad peaks indicative of small grain sizes and with peaks at 2θ angles matching those of the phases WC<sub>1-x</sub> or W. In the in the temperature range 300 to 600 °C, 100-textured WC<sub>1-x</sub> films are deposited and with a shift to a weak 111 orientation at lower temperatures. At 500 °C, TMB flows of 5 to 10 mln results in the growth of 100-textured WC<sub>1-x</sub> films, while lower flows yield W films. Films are deposited with thicknesses up to ~1000 nm, corresponding to a deposition rate of 3.3 nm/s. The microstructure is generally fine-grained, but with broken columns at 500 and 600 °C and a TMB flow of 1 mln. The mechanical properties of the films will be reported.

11:00am **SE+AS+NS+TR-MoM9 Epitaxial and Polycrystalline WN<sub>x</sub> and MoN<sub>x</sub> Films Deposited by Reactive DC Magnetron Sputtering**, Brian Ozsdolay, K. Balasubramanian, Rensselaer Polytechnic Institute, C.P. Mulligan, U.S. Army Armament Research Development & Engineering Center, Benét Laboratories, M.J. Guerette, L. Huang, D. Gall, Rensselaer Polytechnic Institute

WN<sub>x</sub> layers, 1.45- $\mu$ m-thick, were deposited by reactive magnetron sputtering on MgO(001), MgO(111), and Al<sub>2</sub>O<sub>3</sub>(0001) in 20 mTorr N<sub>2</sub> at T<sub>s</sub> = 500-800 °C. X-ray diffraction  $\omega$ -2 $\theta$  scans,  $\omega$ -rocking curves,  $\phi$  scans, and reciprocal space maps show that all layers deposited from 500-700 °C exhibit the cubic rock-salt structure, with a relaxed lattice constant that decreases from 4.299 to 4.171 Å as the N-to-W ratio decreases from x = 1.20 for T<sub>s</sub> = 500 °C to x = 0.83 for T<sub>s</sub> = 700 °C, as measured by energy dispersive and photoelectron spectroscopies. T<sub>s</sub> = 500-600 °C yields a polycrystalline 111-textured microstructure on all substrates. In contrast, deposition at 700 °C results in epitaxial growth of WN(111) and WN(001) on MgO(111) and MgO(001), respectively, while deposition on Al<sub>2</sub>O<sub>3</sub>(0001) yields a 111-preferred orientation, misoriented cubic WN grains as well as N-deficient BCC W. T<sub>s</sub> = 800 °C causes nitrogen loss and WN<sub>x</sub> layers with primarily BCC W grains and x = 0.04-0.06. The measured elastic modulus ranges from 110-260 GPa for T<sub>s</sub> = 500-700 °C and decreases with increasing N-content, and increases to 350 GPa for T<sub>s</sub> = 800 °C. For samples deposited at T<sub>s</sub> = 700 °C, nanoindentation on WN on MgO(001), MgO(111), and Al<sub>2</sub>O<sub>3</sub>(0001) provides hardness values of 9.8 ± 2.0, 12.5 ± 1.0, and 10.3 ± 0.4 GPa, and elastic moduli of 240±40, 257±13, and 242±10 GPa, respectively. The corresponding shear moduli measured by Brillouin light scattering are 127±2 GPa, 121±2 GPa and 115±2 GPa. MoN<sub>x</sub> layers, 1- $\mu$ m-thick, deposited on MgO(001) also exhibit a cubic rock salt structure with x decreasing from 1.18 for T<sub>s</sub> = 500 and 600 °C to x = 0.76 for T<sub>s</sub> = 800 °C but remaining approximately constant for T<sub>s</sub> = 800-1000 °C. Layers with T<sub>s</sub> > 700 °C contain both epitaxial MoN<sub>x</sub>(001) and 111-oriented grains. The out-of-plane lattice constant decreases from 4.22 to 4.18 Å for 111 oriented grains and from 4.17 to 4.06 Å for epitaxial 001-oriented grains, as T<sub>s</sub> is increased from 700 °C to 1000 °C.

11:20am **SE+AS+NS+TR-MoM10 Phase Stability and In Situ Growth Stresses in Thin Cu/Nb Multilayered Films**, Qianying Guo, L. Wan, R.L. Martens, G.B. Thompson, University of Alabama

As the length scale of individual layers are reduced in a Cu/Nb multilayer, fcc to bcc and bcc to fcc transformations were noted for Cu and Nb respectively. These transitions have been modeled using a thermodynamic phase diagram where interfacial and volumetric energy considerations determine stability and the bilayer thickness of the multilayer is a state variable for predicting those transformations. Using HRTEM, the evolution of the interface from incoherent-to-semicoherent-to-coherent is determined and related to the structural component of the interfacial energy reduction that drives the crystalline transformations. When equal thicknesses of each layer were < 1 nm, the layers underwent an additional transformation from a crystalline to amorphous structure. This has been rationalized by the positive enthalpy of mixing between these two species as they intermixed during the sputter deposition process. The chemical intermixing and local clustering at and near the interface has been quantified by atom probe tomography. These phase transformations have been related to real-time, intrinsic growth stress measurements. All of the multilayers were in a compressive stress state, but a notable reduction in the compressive stress value occurred with each transformation. The collective characterization of the film, via TEM, atom probe, and stress evolution, have provided insights into the structural stability of crystalline phases at the nanoscale.

11:40am **SE+AS+NS+TR-MoM11 Droplets in Cathodic Arc Evaporated (Al,Cr)<sub>2</sub>O<sub>3</sub>-based Coatings and the Nucleation of Dedicated Crystalline Structures**, Christian M. Koller, CDL AOS, TU Wien, Austria, R. Hahn, TU Wien, Austria, J. Ramm, Oerlikon Balzers, Oerlikon Surface Solutions AG, Liechtenstein, S. Kolozsvári, Plansee Composite Materials GmbH, Germany, P.H. Mayrhofer, CDL AOS, TU Wien, Austria  
Corundum-type Al<sub>2</sub>O<sub>3</sub> coatings demonstrate excellent thermo-mechanical properties, giving rise to widespread applications as protective films on, e.g., cutting inserts or components. These coatings are typically synthesised by chemical vapour deposition (CVD) at temperatures of 900 °C or higher, which excludes temperature sensitive substrates. Physical vapour deposition (PVD) proved to be a suitable method for low temperature synthesis of nitrides with excellent properties. However, the growth of single-phased corundum-type  $\alpha$ -Al<sub>2</sub>O<sub>3</sub> by PVD is still a difficult task under standard production conditions. In general, a mixed phase composition of metastable cubic phases is observed, which influence the thermo-mechanical performance of the coating. The utilisation of targets produced by powder metallurgical methods allows for the combination of aluminium with other elements, suitable to promote dedicated crystal structures as demonstrated by AlCr and more recently AlCrFe, where dense crystalline coatings with an increased amount of hexagonal phase fractions were realised. Although

the alloying with Cr and Fe is a promising concept with good prospects, the mechanism to form the hexagonal structure in these materials is yet not understood. Therefore, the aspect of layer-nucleation is investigated in more detail. A significant part of hexagonal crystallites in (Al,Cr,Fe)<sub>2</sub>O<sub>3</sub> coatings is triggered by nucleation onto small particles incorporated in the coating. They originate from the cathode surface and are generated during the cathodic arc process. Cathode surface modifications, macroparticle incorporation and the associated coating microstructures are elucidated by detailed X-ray diffraction and electron microscopy studies. Implications on the coatings' properties and possible technological concepts are discussed.

# Monday Afternoon, October 19, 2015

## Energy Frontiers Focus Topic

Room: 211B - Session EN+AS+EM+NS+SE+SS+TF-MoA

## Solar Cells II

Moderator: Adrie Mackus, Stanford University

2:20pm EN+AS+EM+NS+SE+SS+TF-MoA1 **Influence of Annealing Temperature in the Bulk Defect Formation in Perovskite Thin Films.** *Weina Peng, B.X. Anand, L.-H. Liu, S.C. Sampat, B.E. Bearden, A.V. Malko, Y.J. Chabal*, University of Texas at Dallas

Perovskites are emerging as front-runners for solar cell applications because of their superior optoelectronic properties. Over the past few years the grain size of perovskites has been continuously improved from several hundred of nanometers to a few millimeters which resulted in better solar conversion efficiencies. In addition to surface and grain boundary related defects, perovskites are prone to the formation of bulk defects as well. However the role of bulk defects in the determination of photovoltaic performance of perovskites is rarely explored. To this end we investigate the impact of annealing temperature on the defect density in polycrystalline  $\text{CH}_3\text{NH}_3\text{PbI}_3$  thin films of  $\sim 1$  micron average grain size prepared using vapor assisted solution process (VASP). The photoluminescence (PL) intensity and lifetime show systematic reduction when the annealing temperature is increased from 150°C to 200°C. A rough estimate of the defect state density obtained using fluence dependent PL measurements reveal a 5 fold increase in defect density for a 25°C increase in annealing temperature although the average grains size stays unchanged. Furthermore, surface passivation of perovskite films using  $\text{Al}_2\text{O}_3$  via atomic layer deposition leads to an improvement in PL intensity and lifetime. But the PL quantum efficiency, as well as the lifetime, of the surface passivated 200°C annealed sample remains significantly lower than that of the un-passivated 150°C annealed sample indicating that the majority of the defects states we observe in the high temperature annealed samples originate from bulk defects. Thus the present study shows that minimizing the number of bulk defects, in addition to surface defects, is very important in the realization of highly efficient perovskite solar cells.

3:00pm EN+AS+EM+NS+SE+SS+TF-MoA3 **Tandem Solar Cells Using Perovskites, Silicon and CIGS.** *M.D. McGehee, Tomas Leijtens*, Stanford University **INVITED**

The efficiency of perovskite solar cells has soared from a few percent to over 20% in the last 3 years. They are very attractive for multijunction solar cell applications because the bandgap of perovskite semiconductors can be easily tuned in the range of 1.55 to 2.2 eV and the open circuit voltage of the cells is large. We have made highly efficient semitransparent perovskite solar cells using silver nanowire meshes as the top electrode. These cells can be used in combination with either silicon or copper indium gallium diselenide solar cells to make four-terminal and two-terminal tandems. We will also present detailed characterization of perovskite semiconductors made with different processing conditions to show what needs to be done to minimize recombination and make the solar cells stable.

3:40pm EN+AS+EM+NS+SE+SS+TF-MoA5 **Lifetime, Mobility, and Diffusion of Photoexcited Carriers in Ligand-Exchanged Lead Selenide Nanocrystal Films Measured by Time-Resolved Terahertz Spectroscopy.** *G.W. Guglietta*, Drexel University, *B.T. Diroll, E.A. Gaulding, J.L. Fordham*, University of Pennsylvania, *S. Li*, Drexel University, *C.B. Murray*, University of Pennsylvania, *Jason Baxter*, Drexel University

Colloidal semiconductor nanocrystals have been used as building blocks for electronic and optoelectronic devices ranging from field effect transistors to solar cells. Properties of the nanocrystal films depend sensitively on the choice of capping ligand to replace the insulating synthesis ligands. Thus far, ligands leading to the best performance in transistors result in poor solar cell performance, and vice versa. To gain insight into the nature of this dichotomy, we used time-resolved terahertz spectroscopy measurements to study the mobility and lifetime of PbSe nanocrystal films prepared with five common ligand-exchange reagents. Non-contact terahertz spectroscopy measurements of conductivity were corroborated by contacted van der Pauw measurements of the same samples. The films treated with different displacing ligands show more than an order of magnitude difference in the peak conductivities and a bifurcation of time-dynamics. Inorganic chalcogenide ligand-exchanges with sodium sulfide ( $\text{Na}_2\text{S}$ ) or ammonium thiocyanate ( $\text{NH}_4\text{SCN}$ ) show high THz mobilities above  $25 \text{ cm}^2\text{V}^{-1}\text{s}^{-1}$ , which is desirable for transistors, but nearly complete decay of transient

photocurrent within 1.4 ns. The high mobility with  $\text{NH}_4\text{SCN}$  and  $\text{Na}_2\text{S}$  exchanges is more than offset by their short lifetimes and results in diffusion lengths of only  $\sim 200$  nm. In contrast, ligand exchanges with 1,2-ethylenediamine (EDA), 1,2-ethanedithiol (EDT), and tetrabutylammonium iodide (TBAI) show  $\sim 5\times$  lower mobilities but much longer carrier lifetimes, with  $\sim 30\%$  of photoexcited carriers remaining for  $>10$  ns. The long lifetimes with EDA, EDT, and TBAI yield diffusion lengths of at least 500 nm, which is approaching the film thickness desired for strong light absorption in solar cells. This bifurcated behavior may explain the divergent performance of field-effect transistors and photovoltaics constructed from nanocrystal building blocks with different ligand exchanges.

4:00pm EN+AS+EM+NS+SE+SS+TF-MoA6 **iCVD Synthesis and Integration of Poly(vinylpyrrolidone) and Poly(4-vinylpyridine) as Polymer Electrolytes in Dye Sensitized Solar Cells.** *Yuriy Y. Smolin, S. Janakiraman, A.J. Sauter, M. Soroush, K.K.S. Lau*, Drexel University

Initiated chemical vapor deposition (iCVD) is used to synthesize and integrate poly(4-vinylpyridine) (P4VP) and polyvinylpyrrolidone (PVP) as polymer electrolytes within the mesoporous  $\text{TiO}_2$  photoanode of dye sensitized solar cells (DSSCs). DSSCs with conventional liquid electrolytes are prone to leakage and evaporation, which hinders DSSC durability and field implementation. In addition, liquid electrolytes lead to significant electron recombination within the cells that limit DSSC performance. In contrast, polymer electrolytes do not suffer from the practical disadvantages and could potentially enhance the cell's I-V behavior.

However, in order to enable good contact between the  $\text{TiO}_2$  electrode and the polymer electrolyte, a major obstacle is the difficulty in achieving good pore filling of the polymer into the mesoporous  $\text{TiO}_2$  layer. Mesoscale pore diameter, high aspect ratio, and tortuous pore structure of the photoanode along with liquid surface tension, poor wettability, and solute steric hindrance make pore filling extremely limited when using liquid techniques. This leads to poor electrical contact and lower efficiency. To overcome the challenges of pore filling, we directly synthesized polymer electrolytes inside the pore volume of the photoanode using the solvent-free technique of iCVD. iCVD relies on the vapor delivery of monomer and initiator, which facilitates infiltration into the porous  $\text{TiO}_2$  substrate, and by controlling the relative rates of diffusion and surface polymerization through iCVD process parameters, uniform and conformal growth of polymer is achieved. The pore filling of the polymer electrolyte into 5–10  $\mu\text{m}$  photoanodes using iCVD is typically 90–100% which is significantly better than that achievable with liquid techniques like spin coating.<sup>1</sup>

In this work, we will show that iCVD P4VP and PVP polymer electrolytes can be effectively integrated within  $\text{TiO}_2$  mesoporous photoanodes to produce enhanced DSSCs. By varying the polymer electrolyte chemistry including the use of a crosslinking agent during iCVD to stabilize the resulting polymer structure, DSSC I-V characteristics, such as open-circuit voltage, short-circuit current density and fill factor, are tuned.<sup>2</sup> To gain a better understanding on the effect of the polymer electrolyte, experimental techniques such as linear sweep voltammetry, intensity modulated spectroscopy, and impedance spectroscopy are used. Mathematical modeling of DSSC behavior is also performed to relate these experimental observations with the dynamics of the operation of the cell.

1. S. Nejadi and K. K. S. Lau, *Nano Lett.*, 2010, 11, 419-423.

2. Y. Y. Smolin et al., *J. Power Sources*, 2015, 274, 156-164.

4:20pm EN+AS+EM+NS+SE+SS+TF-MoA7 **Interfacial Effects on Device Performance in Organic Solar Cells.** *Huanxin Ju, J.F. Zhu*, University of Science and Technology of China, *D.S. Ginger*, University of Washington

The better understanding of the underlying mechanisms is essential for the further development of highly efficient organic photovoltaics (OPVs) devices. In this paper, the transient photovoltage (TPV) and charge extraction (CE) measurements in combination with the synchrotron radiation photoemission spectroscopy (SRPES) were used to gain insights into the correlation between the microscopic interfacial properties and macroscopic device performance. The OPV devices based on PCDTBT:  $\text{PC}_{70}\text{BM}$  with Ca interlayer were studied as a reference system to investigate the interfacial effects on device performance. The charge carrier decay dynamics demonstrated that the device with the Ca interlayer exhibited a lower recombination constant ( $k_{\text{rec}}$ ) than that only with the Al cathode at a given charge carrier density ( $n$ ). In addition, the interfacial energy band structures indicated that the strong dipole moment produced by the Ca interlayer can facilitate electron extraction as well as drive hole away at the cathode/polymer interface, resulting in retarding interfacial recombination losses. Finally, we examined the device performance with the Ca interlayer to find that the efficiency is improved by 28% as compared to that without



the Ca interlayer, which shows good correlation with the observed interfacial properties.

4:40pm **EN+AS+EM+NS+SE+SS+TF-MoA8 Tungsten-Titanium Mixed Oxide Thin Films for Improved Structural and Optical Properties for Solar Driven Applications**, *Mirella Vargas*, The University of Texas at El Paso, *N.R. Murphy*, Air Force Research Laboratory, *R.V. Chintalapalle*, The University of Texas at El Paso

Tungsten oxide ( $\text{WO}_3$ ) is a well-established n-type semiconductor possessing unique optical and electronic properties.  $\text{WO}_3$  has become the most interesting inorganic material for electrochromic applications due to the reversible spectral absorption properties associated with  $\text{WO}_3$ .  $\text{WO}_3$  thin films and nanostructures exhibit an optical band gap that permits efficient use of the solar spectrum including absorption in the blue part of the visible region and the ultraviolet region, as well as a high transmission region that extends from the near-infrared (IR) to the visible spectrum. Coupled with good electronic transport properties, photosensitivity, and chemical integrity,  $\text{WO}_3$ -based materials are attractive for applications related to sustainable energy production including energy efficient windows and architecture, photoelectrochemical (PEC) water-splitting, photocatalysis and solar cells. Anion or cation doping into  $\text{WO}_3$  has been extensively studied as this offers the opportunity to tailor the transport properties that may influence the efficiency of solar driven devices. Titanium doping into  $\text{WO}_3$  has proven to enhance the electrochromic response and the cyclic lifetime by a factor of five in PEC devices. In the present case a systematic investigation of progressively increasing the Ti content in the W-Ti target for reactive sputtering has been employed to tune the structure, chemistry, and properties of the films. Tungsten-titanium (W-Ti) mixed oxide thin films were fabricated using reactive sputtering of W-Ti alloy targets with Ti content ranging from 0 to 30 wt.%. X-ray photoelectron spectroscopy confirms the existence of W and Ti in their highest oxidation states of +6 and +4, respectively. Quantification of binding energy shifts for W and Ti core-level transitions confirms the formation of  $\text{WO}_3$ - $\text{TiO}_2$  composite oxide films. Optical analyses made from spectrophotometry measurements indicate a decrease in band gap with a discrete amount of Ti incorporation. The band gap decreases with increasing Ti from 3.0 eV to 2.5 eV. Such films are expected to have the possibility for tuning the electrical conductivity while retaining the optical transparency to make them efficient for photoelectrochemical cells and photovoltaics.

5:00pm **EN+AS+EM+NS+SE+SS+TF-MoA9 Potential Resolution to the "Doping Puzzle" in Pyrite  $\text{FeS}_2$** , *X. Zhang, M. Li, L. O'Brien, J. Walter, M. Manno, F. Mork, J. Kakalios, Eray Aydil, C. Leighton*, University of Minnesota

In principle, pyrite  $\text{FeS}_2$  is one of the most suitable photovoltaic materials for sustainable low-cost, large-scale solar cell manufacturing because it has high absorbance in the visible and comprises earth-abundant inexpensive elements. However, current efficiencies of solar cells based on pyrite  $\text{FeS}_2$  have not exceeded 2.8%. Early research on this material concluded that unintentionally doped  $\text{FeS}_2$  thin films are p-type and subsequent solar cell work evolved based on this presumption. In fact, it is now widely accepted that  $\text{FeS}_2$  thin films almost always exhibit p-type conduction even though single crystals are typically found to be n-type. This discrepancy between single crystals and thin films is perplexing and to date this puzzle remains unexplained. In this talk we reexamine the conclusion that undoped  $\text{FeS}_2$  films are predominantly p-type and provide an explanation for this "doping puzzle" in pyrite. Using a combination of Hall effect, thermopower, and temperature-dependent resistivity measurements on a large set of well characterized single crystals and thin films, we show that the widely accepted predominant p-type behavior in pyrite films may, in fact, be an artifact of hopping conduction and should be revisited. Specifically, both Hall effect and thermopower measurements establish that all of our high-mobility ( $>1 \text{ cm}^2\text{V}^{-1}\text{s}^{-1}$ ) films and single crystals are n-type. Temperature-dependent resistivity measurements on these high mobility films and crystals establish diffusive electronic transport. We find that films with lower mobility ( $4 \times 10^{-2} - 1 \text{ cm}^2\text{V}^{-1}\text{s}^{-1}$ ) also show n-type Hall effect but exhibit a p-type Seebeck coefficient, leading to a discrepancy in the measured carrier type. Temperature-dependent resistivity measurements on these intermediate mobility films show a transition from diffusive to hopping transport. Finally, both Hall and Seebeck coefficients are strongly suppressed and invert in the lowest mobility thin films ( $<4 \times 10^{-3} \text{ cm}^2\text{V}^{-1}\text{s}^{-1}$ ) indicating apparent p-type conduction. Temperature-dependent resistivity measurements establish unambiguous hopping behavior in these lowest mobility films. Based on this evolution of Hall and Seebeck coefficients with carrier mobility, and the well-known suppression of the Hall and Seebeck effects in conductors with hopping electronic transport, we conclude that the apparent crossover from n-type to p-type with decreasing mobility is, in fact, an artifact of hopping conduction.

Work supported by the NSF under DMR-1309642, in addition to the University of Minnesota NSF MRSEC under DMR-1420013.

5:20pm **EN+AS+EM+NS+SE+SS+TF-MoA10 Interparticle Contact Radius and Electron Transport in Thin Films Comprised of Nanocrystals**, *Elijah Thimsen, D. Lanigan*, Washington University, St. Louis

Thin films comprised of nanocrystals are being explored for a variety of applications that involve electron transport. For traditional applications such as photovoltaic solar cells, the goal is often to utilize solution processing to make an inexpensive thin film that essentially behaves as a bulk material with diffusive transport. For other applications, such as neuromorphic computing, variable range hopping (VRH) transport is more desirable because it enables a given nanocrystal to have orders of magnitude more nearest neighbors than it physically touches. It is of paramount importance that the structure-property relationships that control electron transport mechanism be elucidated. Previous work has demonstrated that interparticle separation distance affects charge carrier mobility. However, for films comprised of nanocrystals that are physically touching, what is the effect of contact radius? In this work, we present a systematic experimental study of the effect of interparticle contact radius on the electron transport mechanism in thin films comprised of heavily-doped ZnO nanocrystals embedded in  $\text{Al}_2\text{O}_3$ . As the contact radius increased, the electron transport mechanism crossed over from VRH to diffusive conduction. For large contact radius between nanocrystals, the room-temperature electron mobility in the film approached the local mobility within a nanocrystal, approximately  $10 \text{ cm}^2 \text{V}^{-1} \text{s}^{-1}$ . The conclusion is that for nanocrystals that are physically touching, the interparticle contact radius determines the transport mechanism. With the ability to control the electron transport mechanism in films comprised of ZnO nanocrystals, we performed an exploratory study of the Hall effect in these materials. Hall effect measurements are of great utility and are routine for determining charge carrier mobility and type, but the interpretation of data for materials that exhibit VRH has been difficult in the past. For well-connected ZnO nanocrystals that exhibit diffusive conduction, the Hall coefficient was independent of temperature, as expected for the high doping level. Alternatively, for films with small contact radius between nanocrystals, which exhibited a VRH transport mechanism, we observed an anomalous behavior of the Hall coefficient at low temperature (100 to 200 K). Surprisingly, for films that exhibited VRH, the magnitude of the Hall coefficient increased exponentially with decreasing temperature, in stark contrast to the conventional wisdom that the Hall effect is suppressed for VRH.

## Advanced Surface Engineering

Room: 212A - Session SE+EM+EN-MoA

## Thin Film Technologies for Energy Storage, Conversion and Harvesting

Moderator: Michael Stueber, Karlsruhe Institute of Technology, Andrey Voevodin, Air Force Research Laboratory

2:20pm **SE+EM+EN-MoA1 Properties of Zinc Oxide Thin Films Grown on Silicon Wafers by Pulsed Laser Deposition**, *Yilu Li, J.W. Wrobel, M.K. Michael*, University of Missouri-Kansas City

Pulsed ultraviolet light from a XeF excimer laser was used to grow thin films of zinc oxide on (111) p-type silicon wafers within a versatile high vacuum laser deposition system. Pressure, target temperature and distance from the target to the substrate can be adjusted in the system. Scanning electron microscopy, energy dispersive X-ray spectroscopy, X-ray diffraction spectroscopy and ellipsometry had been used to analyze the structures and properties of ZnO thin film products.

3:00pm **SE+EM+EN-MoA3 Synthesis of Crystallized and Nanostructured  $\text{TiO}_2$  Thin Films by Reactive Magnetron Sputtering for Application as Photoanode in Dye Sensitive Solar Cells**, *J. Dervaux, P.-A. Cormier, S. Konstantinidis*, Université de Mons, Belgium, *P. Moskovkin, S. Lucas*, University of Namur, Belgium, *Rony Snyders*, Université de Mons, Belgium

Nowadays, the efficient use of renewable energies, and more specifically of solar energy, represents a major economic and environmental issue. Among the potential solutions, the Dye Sensitive Solar Cells (DSSC) present many advantages. In order to improve the efficiency of DSSC,  $\text{TiO}_2$  nanoparticles, which are usually used as photo-anode, could be replaced by nanostructured  $\text{TiO}_2$  thin films. Indeed, a photo-anode of ordered porous nano-columnar  $\text{TiO}_2$  would provide large surface area for dye absorption, fast electron transfer path, enhanced light trapping, and tight interfaces to conducting electrodes and contributes to a high fill factor and an overall higher cell efficiency. In view of this application, the anatase phase of  $\text{TiO}_2$  is usually



the preferred polymorph as electron acceptors in DSSCs even if a synergistic effect exists between anatase and rutile with an optimal rutile content of around 13 wt%.

In this work, nanostructured and crystallized TiO<sub>2</sub> thin films are synthesized by reactive magnetron sputtering combined with Glancing Angle Deposition (GLAD). The substrate temperature, the substrate bias voltage and the rotation speed were varied in order to determine the best experimental conditions leading to (nano-)porous films with anatase TiO<sub>2</sub> columns. The chemical composition, the crystalline structure and the microstructure of the films were analyzed by XPS, XRD, SEM and TEM, respectively while the surface area is evaluated by the BET method.

It is demonstrated that many type of microstructures (tilted columns, straight pillars, chevrons,...) are obtained by combining the GLAD parameters and the sputtering conditions. On the other hand, depending on these growth conditions, the phase constitution can be tuned from amorphous to pure rutile or anatase phases including mixtures of both polymorphs. The surface area of the synthesized layer strongly depends on the experimental conditions and on the associated microstructure. The highest obtained value is of  $\sim 140$  m<sup>2</sup>/g for a tilted columnar amorphous/anatase sample which is significantly better than the values reported for TiO<sub>2</sub> nanoparticles systems ( $\sim 60$  m<sup>2</sup>/g). On the other hand, a clear correlation between the surface area and the dye absorption is demonstrated revealing a good impregnation of the layer. It is also demonstrated that this impregnation behaviour is depending on the size of the dye molecule revealing different populations of pores as a function of their size. This is supported by TEM and modelling data using NASCAM, a 2D-3D Kinetic Monte Carlo code for the simulation of deposition, diffusion, nucleation and growth of films on a surface.

**3:20pm SE+EM+EN-MoA4 Silver-Carbon-Nanotube Metal Matrix Composites for Metal Contacts on Space Photovoltaic Cells, Omar K. Abudayyeh, C. Nelson, S.M. Han, University of New Mexico, N. Gapp, D.M. Wilt, Air Force Research Laboratory**

The advanced solar cells used in space vehicles today are rapidly moving towards thin-film-based inverted metamorphic multijunction (IMM) solar cells mounted on flexible substrates. However, the IMM cells are more prone to cracking than state-of-the-art triple junction cells. The cell cracking can lead to metal contact failure on IMM cells, compromising the power generation. To mitigate the power loss and increase the lifetime of IMM cells, silver metal films imbedded with carbon nanotubes (CNTs), otherwise known as metal matrix composites, have been developed and investigated for the reinforced mechanical strength against stress-induced cracking. We have primarily focused on (1) surface functionalization of CNTs to make their surface more hydrophilic and wetting to metals, (2) optimization of a cyanide-free electrochemical deposition of silver, (3) electrochemical deposition, drop casting and nanospreader technique to control the composite microstructure, and (4) mechanical and electrical characterization of the composite films. We observe that carboxylation of CNTs produces a stable, homogeneous suspension of negatively charged CNTs at pH > 6. Lustrous-mirror-finish silver films are also successfully deposited, using a commercial cyanide-free silver-plating solution with precise control of current density. Currently, one of the microstructures being explored is a silver-carbon-nanotube layer-by-layer structure, where the surface coverage of CNTs is an important parameter that directly affects the CNT packing fraction and metal intercalation through the CNT network. We quantify the CNT surface coverage as a function of different deposition variables by digitally analyzing scanning electron microscopy images. In this presentation, we will further discuss how this surface coverage correlates to the mechanical and electrical properties of the MMC films. We characterize the mechanical properties, using nanoindentation and strain failure tests. The initial nanoindentation analysis reveals that the composite film has a lower elastic modulus (10 GPa) than pure silver (73 GPa) or CNT (1000 GPa). The lower elastic modulus is attributed to the electroplating process of silver, in which hydrogen is incorporated and trapped within the composite. Our finite element analysis also corroborates this speculation, where the elastic modulus near 10 GPa is predicted with approximately 4% void fraction. While the composite elastic modulus is lower than that of pure silver, the strain failure tests show that carbon nanotubes can bridge 20 to 50-mm-wide microcracks, maintaining electrical conductivity of the composite.

**3:40pm SE+EM+EN-MoA5 Laser Liftoff of Single Crystal GaAs Thin Films and Energy Conversion Devices, Bruce Clemens, G. Hayes, V. Parameshwaran, A. Jan, J.B. Reeves, Stanford University INVITED**

GaAs and related III-V sphalerite materials offer a wide array of tunable characteristics that lend themselves to many advanced device technologies. However, the cost of GaAs substrates limits their use, specially for photovoltaics. Separating epitaxially-grown layers from a growth substrate can reduce costs, however the current approach, which uses an acid to laterally etch an epitaxial sacrificial layer, is slow and can damage other

device layers. Here, we demonstrate laser lift-off as a new approach that is orders of magnitude faster, and that enables more freedom in the selection of other device layers. We grow a structure with a spatially-tuned optical absorption coefficient by growing a small-band-gap, pseudomorphic layer between the GaAs substrate and a GaAs film and device structure. By using InGaAsN with a band gap of 0.9 eV for this layer, we achieve high absorption of 1064 nm (1.17 eV) light from a Nd:YAG nanosecond laser pulse, while GaAs is essentially transparent for this wavelength. Illumination through the back of the GaAs substrate with laser fluences of about 0.7 J/cm<sup>2</sup> achieves transfer of the GaAs layer to a flexible polymer substrate. Transmission electron microscopy and x-ray diffraction show that the initial InGaAsN layer is coherently strained to match the GaAs substrate, and that the GaAs film is strain-free and free of dislocations, both before and after lift-off. Thermal modeling shows only modest heating outside of the InGaAsN layer, so that the film or device above the InGaAsN layer experiences minimum thermal exposure. Examination of the lift-off interfaces shows evidence of melting and re-solidification. We demonstrate a process using additional InGaP etch layers that allow for quick and easy clean-up of this melted region, resulting in restoration of the original GaAs wafer surface to a condition suitable for re-use. Thus our process can transform the GaAs substrate from a consumable to a manufacturing tool. Device performance and material properties of lifted-off devices will be reported.

**4:20pm SE+EM+EN-MoA7 Optical and Structural Properties of Metal-dielectric Composite Films, Lirong Sun, N.R. Murphy, J.G. Jones, J.T. Grant, Air Force Research Laboratory**

In this work, the metal - metal oxide composite films were prepared in multilayer stacks. A medium layer of silver or a mixture of silver and oxide (SiO<sub>2</sub>, Al<sub>2</sub>O<sub>3</sub>, ZnO and ITO) was embedded between the host (SiO<sub>2</sub>, Al<sub>2</sub>O<sub>3</sub>, ZnO and ITO) materials. The mixture of silver and oxide was deposited by co-sputtering the silver target and one oxide target in pure argon simultaneously using DC and pulse DC magnetron sputtering techniques. The optical constant of composite films was tailored by varying deposition time of the medium layer, deposition conditions and host material. The absorbing spectral peaks were influenced by silver content, silver particle sizes and oxide matrix. The *in situ* spectroscopic ellipsometry data was performed in real time during film growth to derive film thickness and optical constants. The dispersion results were further correlated with absorption spectra, film density, grain sizes and surface morphology by UV-Vis-NIR spectra, X-ray diffraction, X-ray reflectivity and scanning electron microscope measurements.

**5:00pm SE+EM+EN-MoA9 Atomic Layer Deposition of Alumina and Titania Passivation Layers in Microchannel Reactors for Coke Suppression, Hao Feng, Xi'an Modern Chemistry Research Institute, China**

Alumina and titania thin films are deposited inside the channels of stainless steel tubes by atomic layer deposition to deactivate the metal surface for the purpose of coke suppression. The ALD equipment is modified to incorporate the high-aspect-ratio metal tubes into the flow path. Experiment parameters are adjusted to ensure complete and uniform coverage of the internal surface areas of the metal tubes. The thicknesses of the passivation layers are precisely controlled by adjusting the number of ALD cycles. In coking experiments the passivated metal tubes are used as reactors for thermal cracking of a hydrocarbon fuel composed of C<sub>12</sub>-C<sub>16</sub> paraffins. The lifetime of the experiment system passivated by ALD alumina films can be up to 5 times longer compared to the system using bare metal tubes as the reactor. By analyzing the tested metal tube samples it is discovered that the ALD alumina film remains intact after the coking experiment so that the metal catalyzed filament coke formation can be completely inhibited by the alumina passivation layer. The anti-coking performances of ALD titania passivation layers are also noticeable but not as stable. The formation of filament cokes can also be suppressed by titania passivation layers. However, the ALD titania films tend to crack during the coking experiments. This could lead to failures of the passivation layers and acceleration of coke formation.

# Tuesday Morning, October 20, 2015

## Energy Frontiers Focus Topic

Room: 211B - Session EN+AS+EM+SE+SS-TuM

### Photocatalysis

**Moderator:** Jason Baxter, Drexel University, Manjula Nandasiri, Pacific Northwest National Laboratory

8:00am EN+AS+EM+SE+SS-TuM1 **Ultra-dense Hydrogen and Low Energy Nuclear Reactions**, Sveinn Ólafsson, Science Institute, Physics department University of Iceland, L. Holmlid, University of Gothenburg, Sweden

For over the last 25 years the science of cold fusion/LENR has been researched around the world with slow pace of progress. Modest quantity of excess heat and signatures of nuclear transmutation and helium production have been confirmed in experiments and theoretical work has resulted in a flora of possible theoretical scenarios. [1-2]

Here we present energy production in several stages of surface processes that result first in the formation of Rydberg matter of Hydrogen [3] that can later condense in a new ultra-dense Hydrogen phase with 2.3 pm short bond distances. This phase is nuclear active showing break-even fusion reaction [7] under 100mW laser pulsing and slow spontaneous fusion occurring without laser pulsing[4,5,6]. The experimental work in around 30 publications is briefly reviewed and latest experimental results presented and discussed.

In that work high-energy particles are detected from the spontaneous processes using scintillation and other similar detectors. Both spontaneous line-spectra and a spontaneous broad energy distribution similar to a beta-decay distribution are observed indicating detection of particles such as muons. The broad distribution is concluded to be due to nuclear particles, giving straight-line Kurie-like plots. They are observed even at a distance of 3 m in air and have a total rate of  $10^7$ - $10^{10}$  s<sup>-1</sup>. In the talk the link of these observation to Low energy nuclear reactions (LENR) or so called cold fusion will be discussed experimentally and theoretically.

1. The science of low energy nuclear reaction.

Storms E. World Scientific Publishing Company; 2007.

2. The explanation of low energy nuclear reaction.

Storms E. Ienergy Press; 2014.

3. Review paper: Experimental Studies and Observations of Clusters of Rydberg Matter and Its Extreme Forms Leif Holmlid. J Clust Sci (2012) 23:5-34

4. Spontaneous ejection of high-energy particles from ultra-dense deuterium D(0)

Leif Holmlid and Sveinn Ólafsson

Volume 40, Issue 33, 7 September 2015, Pages 10559-10567

5. Charged particle energy spectra from laser-induced processes: nuclear fusion in ultra-dense deuterium D(0) Leif Holmlid and Sveinn Ólafsson submitted 2015.

6. Muon detection studied by pulse-height energy analysis: Novel converter arrangements

Leif Holmlid and Sveinn Ólafsson. Rev. Sci. Instrum. 86, 083306 (2015);

7. Heat generation above break-even from laser-induced fusion in ultra-dense deuterium

Leif Holmlid. AIP Advances 5, 087129 (2015);

8:20am EN+AS+EM+SE+SS-TuM2 **Optical and Surface Properties of Semiconductor Nanowires for Solar Fuels**, Eleonora Frau, J. Vukajlovic, A. Dalmau-Mallorquí, A. Fonctuberta i Morral, E. Alarcon Llado, Ecole Polytechnique Fédérale de Lausanne (EPFL), Switzerland

Semiconductor nanowires (NWs) are filamentary crystals with new properties from their bulk counterparts. Their large versatility makes them excellent candidates as building blocks for contributing to solving the energy problem in the near future. In this work, we will assess two main properties of semiconductor NWs that have an impact to solar energy conversion.

First, it is known that light is strongly absorbed by NW arrays since light resonances give rise to effective absorption cross-sections that are much larger than the geometrical ones. Optical resonances depend on NW geometry and dielectric environment, and can result into absorption effective diameters up to 25 times larger than the geometrical for certain wavelengths. We have used finite-difference time-domain (FDTD)

electromagnetic simulations to understand and design NW-based sunlight scavengers. For instance, a GaAs NW array that is only covering 3% of the surface can generate more photocurrent than a planar film, considering a 30% reflectivity (see figure1). Also that thanks to optical resonances, an indirect-bandgap material such as Si is capable of absorbing most of the light within a 2um long NW array that only covers 7% of the device surface.

On the other hand, it is also known that surface states and traps detriment device performances. However, in case where solar energy is directly converted into fuel (such as hydrogen) in a photoelectrochemical (PEC) cell, the large surface-to-volume ratio of NW forests is an important asset. Since the electrochemical reactions happen at the semiconductor surface, NWs enable the use of low-cost catalysts (e.g. MoSx) even though they exhibit lower performances than noble metals (e.g. Pt). In order to assess the effects of nanostructuring photo-electrodes for solar fuel generation, we have studied photo-cathodes based on Silicon nanopillar structures. The photo-cathodes were fabricated by using a top-down approach and their diameters range from ~200 to 900nm and lengths ~2um. We observe that reducing the size of the nanostructure, increases the overpotential, and thus the overall efficiency (see figure 2). By coating the surface with thin TiO<sub>2</sub> layers, the performance is improved in terms of overpotential and fill factor. We explain these findings by using an electrico-kinetic model of the semiconductor-water junction. We find that the TiO<sub>2</sub> layers actually act as a hole blocking layer, preventing recombination.

8:40am EN+AS+EM+SE+SS-TuM3 **Engineering Surfaces and Interfaces for Photoelectrochemical (PEC) Water-Splitting**, Thomas Jaramillo, J.D. Benck, Stanford University, J. Kibsgaard, SLAC National Accelerator Laboratory, T.R. Hellstern, C.J. Hahn, P. Chakhranont, R. Britto, K.D. Fong, Stanford University

INVITED

The talk will focus on engineering surfaces and interfaces for solar photoelectrochemical (PEC) water-splitting for the direct, renewable production of H<sub>2</sub>. In particular, this talk begin by describing research efforts to develop H<sub>2</sub> evolution catalysts that are active, stable, and comprised of only earth-abundant elements, including transition metal sulphides, phosphides, and phosphosulfides.<sup>1-3</sup> Next, we will describe recent efforts to integrate these catalysts onto semiconductor surfaces to provide corrosion protection as well as enhanced interfacial catalysis for PEC water-splitting.<sup>4</sup> This talk will focus on the need for high turnover frequency (TOF) catalysts, which ultimately enable the greatest flexibility in designing optimum interfaces for high performance devices.

[1] J. Kibsgaard, T.F. Jaramillo, F. Besenbacher, "Building an appropriate active site motif into a hydrogen evolution catalyst with thiomolybdate [Mo<sub>3</sub>S<sub>13</sub>]<sup>2-</sup> clusters," *Nature Chemistry*, **6** (2014) 248.

[2] J.D. Benck, T.R. Hellstern, J. Kibsgaard, P. Chakhranont, T.F. Jaramillo, "Catalyzing the Hydrogen Evolution Reaction (HER) with Molybdenum Sulfide Nanomaterials," *ACS Catalysis*, **4** (2014) 3957.

[3] J. Kibsgaard and T.F. Jaramillo, "Molybdenum Phosphosulfide: An Active, Acid-Stable Earth-Abundant Catalyst for the Hydrogen Evolution Reaction," *Angewandte Chemie*, **53** (2014) 14433.

[4] J.D. Benck, S.C. Lee, K.D. Fong, J. Kibsgaard, R. Sinclair, T.F. Jaramillo, "Designing active and stable silicon photocathodes for solar hydrogen production using molybdenum sulfide nanomaterials," *Advanced Energy Materials*, **4** (2014) 1400739.

9:20am EN+AS+EM+SE+SS-TuM5 **Bulk and Surface Effects of Incorporating Titanium Into Hematite Thin Films to Improve Photoelectrochemical Water Splitting**, Anthony Abel, A.M. Patel, Drexel University, I.G. Torregrosa, Utrecht University, Netherlands, B. Opananont, J.B. Baxter, Drexel University

Hematite ( $\alpha$ -Fe<sub>2</sub>O<sub>3</sub>) has emerged as a promising photoanode material for photoelectrochemical (PEC) water splitting due to its chemical stability, earth-abundance, low cost, and suitable band gap for both water splitting and visible light absorption. However, poor charge separation due to low hole mobility and high recombination rate, and sluggish oxygen evolution reaction kinetics have limited its potential as an economical water-splitting catalyst. Here, we investigate titanium incorporation into hematite photoanodes and provide insight into the role of Ti<sup>4+</sup> in improving PEC performance. Planar hematite thin films (~45 nm thick) were deposited by successive ionic layer adsorption and reaction (SILAR) of FeOOH on an FTO/glass substrate and subsequent annealing to induce phase transition to  $\alpha$ -Fe<sub>2</sub>O<sub>3</sub>, and titanium was incorporated up to 10% Ti/(Ti+Fe) by either modification of the SILAR solution (SM: $\alpha$ -Fe<sub>2</sub>O<sub>3</sub>) or solid-state diffusion (SSD: $\alpha$ -Fe<sub>2</sub>O<sub>3</sub>) during the annealing process. PEC measurements revealed substantial improvements in both charge separation efficiency and hole injection into the electrolyte, increasing photocurrent from nearly zero to

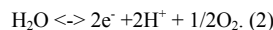
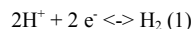
~0.6 mAc<sup>m</sup>-<sup>2</sup> under 1-sun irradiation at 1.23 V<sub>RHE</sub>. Mott-Schottky analysis indicated a 100 mV cathodic shift in the flat band potential upon doping with Ti<sup>4+</sup> regardless of fabrication method, but a 100-fold increase in carrier density only in SM:α-Fe<sub>2</sub>O<sub>3</sub> films, resulting in a high 20 % separation efficiency at 1.23 V<sub>RHE</sub> with optimized 5 % Ti/(Ti+Fe) in the modified SILAR solution. Electrochemical impedance spectroscopy showed a 4x increase in the surface state capacitance peak near the water oxidation onset potential, possibly due to reduced Fermi level pinning as a result of more efficient hole injection into the electrolyte. More importantly, doping with titanium resulted in a 100-fold decrease in the charge transfer resistance from surface states to the electrolyte, revealing the strong influence of Ti<sup>4+</sup> on interfacial kinetics. Further surface modification with an ultrathin FeOOH surface passivation layer raised the plateau photocurrent to ~0.8 mAc<sup>m</sup>-<sup>2</sup> at 1.23 V<sub>RHE</sub>, representing a 3x improvement over previous reports of SILAR-deposited hematite films and comparable with record performance for planar hematite deposited using high vacuum synthesis techniques.

9:40am **EN+AS+EM+SE+SS-TuM6 Iron Oxide Nanoparticle Growth on Highly Oriented Pyrolytic Graphite (HOPG) and Photocatalytic Properties of Pt on Iron Oxide**, *Jayde Kwon, J.C. Hemminger*, University of California, Irvine

Highly oriented pyrolytic graphite (HOPG) is an ideal substrate to study the fundamental growth mechanism of iron oxide independent from substrate effects. Platinum on iron oxide is a model heterogeneous catalyst with importance to biotechnology and solar cell applications. Selective growth of iron oxide nanoparticle (NP) either on step edges of HOPG or oxygen plasma treated HOPG by physical vapor deposition (PVD) will be presented. The successful selective iron oxide NP growth was validated by scanning electron microscopy (SEM), transmission electron microscopy (TEM), and X-ray photoelectron spectroscopy (XPS). The development of the NP array system is highly significant in that it can provide an ideal template for theoretical calculations for fundamental metal growth studies. Pt nanoparticles were subsequently deposited on the iron oxide nanoparticles using a selective photodeposition technique. The application of these nano-systems (Pt nanoparticles on iron oxide nanoparticles) towards photocatalysis of methylene blue will be presented. Although iron oxide is a promising semiconductor photocatalyst, it suffers from a short hole diffusion length, low electrical conductivity and a high rate of electron hole recombination. However, this bimetallic system using platinum deposited on iron oxide overcomes these barriers. A novel method was developed using small quantities of Pt on iron oxide to significantly enhance methylene blue decomposition. This system is also being explored as a catalytic model for water-gas shift reactions.

11:00am **EN+AS+EM+SE+SS-TuM10 Interface Design for Efficient and Stable Photoelectrochemical Water Splitting**, *Joel Ager*, Lawrence Berkeley National Laboratory **INVITED**

Solar photoelectrochemical (PEC) water splitting is potential future carbon-neutral energy source which could dramatically change the landscape of global energy generation and storage. The half reactions for water splitting are as follows:



The free energy change for the overall reaction,  $\text{H}_2\text{O} \leftrightarrow \text{H}_2 + 1/2\text{O}_2$  corresponds to 1.23 eV per electron transferred; however, typically >1.5 V is required to overcome kinetic limitations, particularly for the O<sub>2</sub> evolution reaction. The most commonly used approach for integrated solar water splitting employs photocathodes (H<sub>2</sub> or hydrocarbon producing) and photoanodes (O<sub>2</sub> producing) linked in a tandem geometry [1].

The interface challenges required to demonstrate a practical system which is both efficient and stable under operation are substantial and severe. In addition to constructing interfaces, either solid-solid or solid liquid, which achieve the desired photovoltaic charge separation, the surfaces of these photoelectrodes can be a failure point under sustained operation due to corrosion. We have found that the use of nanoscale conformal oxide layers can greatly reduce corrosion rates. Moreover, it is possible to achieve both high performance and lifetime by the use of protection layers which are also tuned for selective carrier contact.

Examples of such a strategy will be shown for photocathodes [2-5] and for photoanodes [5]. Recent work on p-type transparent oxides (p-TCOs) used as selective hole contacts for photoanodes will be emphasized. For example, it will be shown that using NiCo<sub>2</sub>O<sub>4</sub> as the p-TCO and n-type Si as a prototypical light absorber, a rectifying heterojunction capable of light driven water oxidation can be created. By placing the charge separating junction in the Si using a np<sup>+</sup> structure and by incorporating a highly active Ni-Fe oxygen evolution catalyst, efficient light-driven water oxidation can be achieved. The generality of the p-TCO protection approach is

demonstrated by multi-hour, stable, water oxidation with n-InP/p-NiCo<sub>2</sub>O<sub>4</sub> heterojunction photoanodes.

**Acknowledgements.** This material is based upon work performed by the Joint Center for Artificial Photosynthesis, a DOE Energy Innovation Hub, supported through the Office of Science of the U.S. Department of Energy under Award Number DE-SC0004993.

#### References.

1. J. W. Ager *et al.*, *Energy Environ. Sci.* (2015). DOI:10.1039/C5EE00457H
2. M. H. Lee *et al.*, *Ang. Chemie Int. Edition* **51** 10760 (2012).
2. Y. Lin *et al.*, *Nano Letters* **13** 5615 11 (2013)
3. Y. Lin *et al.*, *J. Phys. Chem. C* **119**, 2308 (2015).
4. J. Yang *et al.*, *J. Amer. Chem. Soc.* **136** 6191 (2014).

11:40am **EN+AS+EM+SE+SS-TuM12 Buried, Hetero, and p-i-electrolyte III-V Photoelectrochemical Junctions with Significantly Enhanced Photocurrent Onset Potentials**, *James Young, H. Doscher, J. Turner, T. Deutsch*, National Renewable Energy Laboratory

To approach the maximum achievable solar-to-hydrogen (STH) conversion efficiencies with photoelectrochemical (PEC) devices, it is necessary to employ the lowest possible band gap (E<sub>g</sub>) absorbers that can still provide sufficient voltage to drive water splitting at high rates (1.7-1.8 V for 25% STH). The record 12.4% STH was achieved by a GaInP<sub>2</sub>/GaAs PEC/photovoltaic (PV) tandem device while an all solid state GaInP<sub>2</sub>/GaAs PV/PV tandem produces an open-circuit voltage that approaches 2.4 V. Since GaAs (E<sub>g</sub> = 1.4 eV) is the current-limiting junction in these devices, it can be substituted by InGaAs with E<sub>g</sub> = 1.0 eV to reach 25% STH. The current-for-voltage tradeoff of using lower-E<sub>g</sub> absorbers moves toward the constraint of insufficient voltage for spontaneous water splitting. To address this approaching constraint, we investigate several alternative device structures at the III-V/electrolyte interface that show photocurrent onset potential enhancements of a few hundred mV. We will present band diagram calculations and electrochemical measurements to discuss the voltage performance of these structures.

12:00pm **EN+AS+EM+SE+SS-TuM13 X-ray Absorption Studies on the Li-S Battery Cathode Side**, *Yifan Ye*, University of Science and Technology of China, *A. Kawase*, Lawrence Berkeley National Laboratory, *H.X. Ju*, University of Science and Technology of China, *E. Cairns*, Lawrence Berkeley National Laboratory, *J.-H. Guo*, Lawrence Berkeley Lab, University of California, Berkeley, *J.F. Zhu*, University of Science and Technology of China

As increasing global energy consumption in the coming days, sustainable, clean energy technologies are highly desirable. The high theoretical specific capacity of 1675 mA·h/g for elemental S has prompted intense effort to study the Lithium-Sulfur batteries. With the application of cetyltrimethyl ammonium bromide (CTAB), modified sulfur-graphene oxide (S-GO) nano-composite based Li/S batteries exhibited a very high initial discharge capacity of 1440 mA·h/g of sulfur at 0.2C with excellent rate capability of up to 6C for discharge and 3C for charge while still maintaining high specific capacity. And the batteries demonstrated cycling performance up to 1500 cycles with extremely low decay rate of 0.039% per cycle. With the introduction of CTAB, the performance of the GO-S based Li-S battery has been improved significantly, thus it is important to figure out the role of CTAB played in the system. During the synthesis process of the cathode materials, S and Na<sub>2</sub>S were used as the precursors, the ratio of S/Na<sub>2</sub>S is crucial to the components of the precursors. Moreover, the sequence of mixing GO/CTAB solution with precursor solution is a key point to effective cathode synthesis procedure. Understanding these information helps to optimize the methodology for the controllable synthesis of desired cathode material that can be used to fabricate an efficiency and well-performed Li/S battery. S K-edge X-ray absorption spectroscopy (XAS) is applied to study the chemical species evolution during the GO-S-CTAB cathode material synthesis. The influences on the cathode materials related to the battery performance are monitored by S K-edge XAS. The research revealed the interaction between CTAB and GO, S, Na<sub>2</sub>S and Na<sub>2</sub>S<sub>x</sub>. It indicated that CTAB can physical adsorbed on Na<sub>2</sub>S<sub>x</sub> molecules by bonding with the terminal S atoms of Na<sub>2</sub>S<sub>x</sub> chains, and this kind of bonding can convert to chemical C-S bonding with heating treatment. Thus the interaction of CTAB with GO, formed C-S between CTAB and S and interaction of GO and S provided a tight tri-layer structure which can immobilize the S particles on GO sheet and finally enhanced the battery performance. The information from this work proved the importance of Na<sub>2</sub>S:S ratio, CTAB/GO adding procedure in the fabrication process, and we can easily apply XAS to optimize these recipe. And moreover, this work proved strong evidence that XAS tools can be used to do the initial characterization on the battery performance before real cycling procedure.

## Atmospheric Pressure Plasmas, CVD and Other Deposition Methods

**Moderator:** Hana Barankova, Uppsala University, Sweden, Michael Stueber, Karlsruhe Institute of Technology

8:00am **SE+PS+SM-TuM1 Synthesis of Hybrid Nanoparticles - Fluorinated (Super)Hydrophobic Coatings by Atmospheric Plasma : Possibilities and Challenges.** *J. Mertens, J. Hubert, N. Vandecasteele, François Reniers*, Université Libre de Bruxelles, Belgium

In order to obtain superhydrophobic coatings, one has to combine a low surface energy surface with a specific roughness. We propose a simple method to obtain such coatings by depositing by atmospheric plasma fluorinated coatings starting from C<sub>6</sub>F<sub>12</sub> or C<sub>6</sub>F<sub>14</sub> in argon or helium onto surfaces previously decorated with SiO<sub>2</sub> or TiO<sub>2</sub> nanoparticles. The loading (concentration) and size of nanoparticles were varied, as well as the plasma parameters (nature of the process gas and precursor, plasma power, deposition time). Depending on the experimental parameters, coatings exhibiting water contact angles from 110° to more than 160° could be obtained. The mechanisms for the polymer synthesis have been studied by a combination of atmospheric mass spectrometry and X-ray photoelectron spectroscopy, and the influence of the process gas on the final chemical structure of the coating is evidenced and explained. A higher fragmentation pattern is shown for Argon, due to the higher electron density and the higher energy available in the filamentary discharge. This is responsible for a change in the CF<sub>2</sub> and CF<sub>3</sub> moieties in the final coating. Similarly, the nature of the oxide nanoparticles has a strong influence on the chemistry of the coating: whereas SiO<sub>2</sub> particles do not modify the CF<sub>x</sub> moieties, the TiO<sub>2</sub> nanoparticles contribute to a significant degradation of the chemistry of the coating. This method can easily be implemented on any industrial process line, provided a good adhesion of the final coating on the substrate is obtained.

8:20am **SE+PS+SM-TuM2 Deposition of Antifouling PMOXA-like Coatings using Atmospheric Pressure Helium Plasma Jet.** *Sameer Al-Bataineh, A. Cavallaro, M. Ramiasa, K. Vasilev*, University of South Australia

Antifouling interfaces are important in a wide range of applications such as food packaging, water purification, marine biofouling and biomedical devices.<sup>1,2</sup> In recent years, poly(2-oxazoline)s have attracted much attention due to their numerous biological applications as antifouling polymers.<sup>3,4</sup> Poly(2-methyl-2-oxazoline)(PMOXA) has antifouling properties comparable to the gold standard PEG, and has better stability in a range of aqueous solution and biological media.<sup>5</sup> Atmospheric pressure plasma (APP) is an emerging technology with a wide range of applications including material processing.<sup>6</sup> The advantage of using APP for surface modification is that it eliminates the use of expensive vacuum equipment and enables continuous surface modification processes. This study aims to develop PMOXA-like coatings using atmospheric pressure helium plasma jet.

The plasma jet system used in this study consisted of a glass capillary tube with an internal diameter of 1mm that was surrounded by two external hollow electrodes separated by 4mm. The carrier helium gas was sent through a glass container at a flow rate of 1L.min<sup>-1</sup> and carried the oxazoline monomer (2-methyl-2-oxazoline, MOXA) vapour into the glass tube. The plasma jet was operated at an applied voltage of 5.5 kV<sub>pk-pk</sub> and a frequency of 10 kHz. Deposition of the plasma coatings was carried out under static deposition conditions with 3mm separation distance between the end of the capillary tube and the substrate. To enhance stability of the coatings, substrates were heated during plasma deposition process.

Surface elemental composition and molecular structure of oxazoline plasma polymer coatings were thoroughly characterised using XPS and ToF-SIMS. Stability of the plasma coatings were examined by incubation in PBS buffer solution at room temperature overnight. The antifouling properties of the plasma coatings are now under investigation towards resisting protein adsorption and bacterial cell adhesion. In addition, the surface chemistry and functionality of the coatings produced in this study will be briefly compared to those prepared with an RF low pressure plasma.<sup>7</sup>

This study offers a convenient alternative single step strategy for preparation of oxazoline-based antifouling coatings.

1. Lowe S, et al., *Polym. Chem.*, 2015, 6, 198.
2. Zou L, et al., *J. Membr. Sci.*, 2011, 369, 420.
3. Luxenhofer R, et al., *Macromol. Rapid Commun.*, 2012, 33, 1613.
4. Sedlacek O, et al., *Macromol. Rapid Commun.*, 2012, 33, 1648.

5. Konradi R, et al., *Langmuir*, 2008, 24, 613.
6. Merche D, et al., *Thin Solid Films*, 2012, 520, 4219.
7. Ramiasa MN, et al., *Chem. Commun.*, 2015, 51, 4279.

8:40am **SE+PS+SM-TuM3 Antibacterial Silicon Oxide Thin Films Doped with Zinc and Copper Grown by Atmospheric Pressure Plasma Chemical Vapor Deposition.** *E. Jäger*, Montanuniversität Leoben, *J. Schmidt, A. Pfuch, S. Spange, O. Beier*, INNOVENT e.V., *O. Jantschner, R. Daniel*, Montanuniversität Leoben, *Christian Mitterer*, Montanuniversität Leoben, Austria

Zn- and Cu-doped SiO<sub>x</sub> films were applied by atmospheric pressure plasma chemical vapor deposition to study their antibacterial efficiency against Gram-negative *Escherichia coli* and their cytotoxic effect on the growth of mouse cells. ZnO<sub>x</sub> and CuO<sub>x</sub> particles were found to be homogeneously embedded within the SiO<sub>x</sub> films. For both doping elements, bacteria are killed already within the first three hours after exposure to the film surface. In contrast, mouse cells grow well on the surfaces of both film types, with a slight inhibition effect present only after the first day of exposure, due to the more pronounced release of zinc and copper. The obtained results indicate that the films show a high potential for use as effective antibacterial surfaces for medical applications

9:00am **SE+PS+SM-TuM4 Carbon Bridge Incorporation in Organic-Inorganic Hybrid Coatings using Atmospheric Plasma Deposition in Ambient Air.** *Linying Cui*, Stanford University, *G. Dubois*, IBM Almaden Research Center, *R.H. Dauskardt*, Stanford University

Atmospheric plasma deposition in ambient air has a huge potential for large-scale coating synthesis at reduced cost for energy, display, and aerospace applications. However, the abundant oxygen in air poses significant oxidation challenge for incorporating specific oxygen sensitive components in the coating. In this work, the oxygen sensitive carbon bridge structure was successfully incorporated into the inorganic silicate network in the oxygen-helium atmospheric plasma in ambient air. The mechanism of incorporating the specific carbon structure in an oxidative species rich environment was elucidated by a kinetics model which takes into account the probability of oxidation, adsorption, and desorption of different precursor species during gas transport and on the substrate surface. The key tuning knobs were identified as the precursor chemistry and the precursor delivery rate. The resulting carbon bridged organo-silicate coatings exhibited significantly improved plasticity, more than doubled adhesion, and up to four times increase of moisture resistance in terms of the driving energy threshold for debonding in humid air, compared to plasma silica coatings and commercial sol-gel polysiloxane coatings. In order to further improve the interfacial bonding of the coating to oxygen sensitive substrate in an oxidative atmospheric plasma environment, other deposition parameters were also investigated in order to fully activate but not over-oxidize the substrate. The resulting carbon bridged, highly adhesive coating showed remarkably enhanced hydrothermal stability, a key requirement for application in exterior coatings and functional membranes. As an example for application, the carbon-bridged coating was deposited between hard scratch-resistant coatings and oxygen-sensitive polymer substrate to enhance the adhesion of hard coatings for airplane window protection.

9:20am **SE+PS+SM-TuM5 Atmospheric Plasma in Liquids.** *Ladislav Bardsos, H. Barankova*, Uppsala University, Sweden **INVITED**

Experiments using spark discharge above the water level were reported already in 1784 by Henry Cavendish after his study of air. His results inspired in 1894 Lord Rayleigh and William Ramsay and led to an important discovery of argon present in air. Studies of water electrolysis and interactions of a glow discharge with water solutions were described in 1887 by J. Gubkin and followed in 1952 by R.A. Davies and A. Hickling. The first type of plasma discharge submerged directly into water was an arc. The arc discharges are used for the underwater welding already since 1930. A number of applications of submerged arcs have already been tested and reported. Rapid developments of non-thermal (cold) atmospheric plasma sources during last century led to new studies of plasma in liquids. Studies of the plasma-assisted electrolysis and different phenomena observed on surfaces of electrodes during electrolysis in water electrolytes enhanced an interest in different types of submerged discharges. New processes were developed like the plasma electrolytic oxidation (PEO), formation of nanoparticles and nanotubes, novel plasma-chemical reactions, plasma cleaning, disinfection and "activation" of water or water solutions. This presentation summarizes several interesting systems and results on the submerged plasma in liquids. Examples of the experimental systems and the results of tests of cold plasma discharges in water using different power generators and an efficient low power production of hydrogen from the mixtures of water with ethanol will be presented and discussed in more details.

11:00am **SE+PS+SM-TuM10 Study of Polymer Confinement Effects in Nanocomposite Thin Films Synthesized by Initiated Chemical Deposition, Chia-Yun(Sharon) Hsieh, K.K.S. Lau,** Drexel University

Initiated chemical vapor deposition (iCVD) is a liquid-free polymer synthesis technique that simultaneously deposits the polymers as thin films on supporting substrates. It produces well-defined polymers that are spectroscopically identical to corresponding polymers synthesized in the liquid phase. A wide range of polymers have been produced by iCVD, including hydrophilic polyglycidol (PGL), hydrophobic polytetrafluoroethylene (PTFE), semicrystalline polyethylene oxide (PEO), and amorphous poly (methyl methacrylate) (PMMA). In addition, iCVD is an effective approach for integrating polymers within porous 3D inorganic nanostructures to produce polymer nanocomposite thin films. By utilizing inorganic nanostructural templates such as mesoporous TiO<sub>2</sub> nanoparticle networks, good dispersion of the nanoparticles can be ensured by adopting well-established dispersion procedures. Conformal and uniform polymer growth within the pore space can be achieved by operating under reaction-limited iCVD conditions that allow efficient delivery of reactive precursors by gas and surface diffusion. Quantitative measurements using thermogravimetric analysis has shown that 90–100% of the available pore space can be filled in porous layers of up to 12 μm in thickness with 10–20 nm diameter interconnected pores. As a result, we are able to achieve polymer nanocomposite thin films with high inorganic content (>80 wt%) that are well-dispersed. This ability provides an ideal platform for studying polymer confinement effects that lead to significantly altered polymer properties compared to its bulk 2D planar film counterpart with no inorganic filler. For example, iCVD PGL-TiO<sub>2</sub> nanocomposite thin films has shown a significant increase of 50–60°C in the polymer glass transition temperature (a transition between the glassy, brittle state to the rubbery, pliable state) compared with bulk PGL. This has been attributed to the strong hydrogen bonding interactions between the polar oxygen groups on PGL with the hydroxyl groups on the TiO<sub>2</sub> surface. Here, we will detail the iCVD approach in making different polymer nanocomposite thin films and discuss the resulting nanoscale confinement effects on polymer properties as a result of different polymer-substrate interactions. This knowledge has critical implications in applying polymers in the design of nanostructured devices as bulk polymer properties might not be followed in these systems.

11:20am **SE+PS+SM-TuM11 Persistent Superhydrophilicity of Polycarbonate Surfaces via Nanoimprint Lithography and Atomic Layer Deposition, Xue Li,** Institute of Materials Research and Engineering (IMRE), Singapore, *K.S.L. Chong, M.S.M. Saifullah, R.B. Yang, C.S. Lee, Y.C. Loke,* Institute of Materials Research and Engineering (IMRE), *A.Y. He,* Loke

Superhydrophilic surfaces are often exploited for their anti-fog ability and typically rely on coatings which modify the surface energies of the materials to create such effects. Such traditional coatings are often applied wet and are not long lasting. A persistent superhydrophilic coating with both anti-fog and anti-UV properties have been fabricated on polycarbonate (PC) surfaces *via* a combination of nanoimprint lithography and atomic layer deposition (ALD) process. Nanoimprint lithography was used to pattern anti-reflection (AR) structures on to a PC surface. These samples were then coated with a thin layer titanium dioxide (TiO<sub>2</sub>) layer *via* a low temperature ALD process (<80 °C). The PC sample with AR patterns demonstrated enhanced visible light transmittance upto 94% and reduced transmittance in the UV wavelengths (<400 nm). The TiO<sub>2</sub> layer is superhydrophilic and the resultant samples showed a persistent superior anti-fog effect. More importantly, the superhydrophilicity can be recycled *via* rinsing in an oxidant solution, and had demonstrated stability upto 4 months.

11:40am **SE+PS+SM-TuM12 Enhanced CO<sub>2</sub> Permeation Characteristics Performance On A Crack-Free Nanostructured Ceramic Membrane, Ngozi Nwogu, E. Gobina,** Robert Gordon University, UK

Carbon capture from point source emissions have been acknowledged as one of numerous strategies required for alleviating unrestricted release of greenhouse gases (GHGs) into the atmosphere. To keep greenhouse gases at controllable levels, large drops in CO<sub>2</sub> emissions through capturing and separation will be necessary. Reduction and manipulation of materials at nanometre scale are key experiments in nano-science and nanotechnology. In this work, an experimental study is made on the preparation, the morphological characterization and the gas permeation of ordered ceramic multilayer membranes with silica top layer. We developed and manufactured a crack-free thin film membrane on a fresh tubular alumina ceramic membrane with pore diameter of 6000nm. By using a hybrid material of appropriate proportion, the nano-fabrication conditions are then controlled with extremely high carbon dioxide permeance due to the membrane immersion in a silica solution. Results obtained from the experiments show that the nanostructured silica membranes have potential

applications in the treatment of large gas streams under low pressure conditions like carbon dioxide separation from flue gases.

Keywords: Carbon capture, CO<sub>2</sub> Permeation, nanostructured ceramic membrane & flue gases

# Tuesday Afternoon, October 20, 2015

## Energy Frontiers Focus Topic

Room: 211B - Session EN+EM+NS+SE+SS+TF-TuA

## Batteries and Supercapacitors

**Moderator:** Elijah Thimsen, Washington University, St. Louis, Andrew C. Kummel, University of California at San Diego

2:20pm EN+EM+NS+SE+SS+TF-TuA1 **Behavior of Layered Cathode Materials: A Route to Higher Energy Density for Li-Ion Batteries**, *Marca Doeff, F. Lin*, Lawrence Berkeley National Laboratory, *I. Markus*, Lawrence Berkeley Lab, University of California, Berkeley **INVITED**

The most promising cathode materials for Li-ion batteries geared towards vehicular applications are the so-called NMCs ( $\text{LiNi}_x\text{Mn}_y\text{Co}_z\text{O}_2$ ), based on cost and performance considerations. NMCs exhibit a slightly sloping voltage profile in lithium half-cells, with typical utilizations significantly lower than the theoretical capacity of about 280 mAh/g. An attractive strategy for increasing the energy densities of devices meant for traction applications would be to cycle NMCs to a higher potential than is currently used (usually about 4.3V vs.  $\text{Li}^+/\text{Li}$ ) so that more lithium can be extracted and cycled. For this approach to be viable, the cathodes must exhibit excellent structural stability and good reversibility over a wide composition range. Our recent work has been directed towards understanding the high-potential behavior of NMCs, using an array of synchrotron x-ray techniques as well as transmission electron microscopy. These techniques show that surface reconstruction to rock salt and spinel phases occur during high voltage cycling, and result in impedance rises and apparent capacity losses. The degree to which this occurs is a function of how the material is made and its electrochemical history. Partial substitution of Ti for Co in NMCs not only increases the capacities obtained during cycling to 4.7V in lithium half-cells compared to baseline materials, but appears to improve the cycling behavior as well. First principles calculations show that the aliovalent substitution lowers the voltage profile slightly. This allows a greater amount of lithium to be extracted and cycled below 4.7V, resulting in higher practical capacities. The Ti-substitution also delays the formation of rock salt during charging, resulting in better capacity retention. These observations suggest that optimizing the synthesis and judicious substitution can mitigate deleterious structural changes of the NMCs due to high potential operation in Li-ion cells. These strategies should be combined with those designed to prevent side reactions with electrolytic solutions during high potential operation, such as new electrolytic solutions with improved oxidative stability, or atomic layer deposition coatings on electrode surfaces, to further ensure stable cycling.

3:00pm EN+EM+NS+SE+SS+TF-TuA3 **Next-Generation Electrolytes for Lithium-Ion Batteries**, *Sarah Guillot*, University of Wisconsin - Madison, *M. Usrey, A. Pena-Hueso*, Silatronix, Inc., *R.J. Hamers*, University of Wisconsin-Madison and Silatronix, Inc.

Current-generation electrolytes for lithium-ion batteries are limited in electrochemical stability and thermal stability. Over the last several years, researchers at University of Wisconsin and at Silatronix, inc. have developed several new generations of electrolytes based upon incorporation of organosilane groups into the molecular structure. A recently developed class of compounds shows unprecedented enhancements in performance, including the ability to cycle full cells over 400 times at 70 degrees C, and the ability to reduce or eliminate "gassing" at cathode surfaces. In this talk we will discuss the molecular structure of these organosilane-based compounds, quantitative measurements of the decomposition pathways, and the resulting mechanistic insights into the molecular properties that gives rise to their outstanding performance characteristics.

3:20pm EN+EM+NS+SE+SS+TF-TuA4 **Physico-Chemical Properties of Polyamidoamine Dendrimer-Based Binders for Carbon Cathodes in Lithium-Sulfur Batteries**, *Manjula Nandasiri, P. Bhattacharya, A. Schwarz, D. Lu*, Pacific Northwest National Laboratory, *D.A. Tomalia*, NanoSynthons LLC, *W.A. Henderson, J. Xiao*, Pacific Northwest National Laboratory

Lithium-sulfur (Li-S) batteries are one of the most promising energy storage systems, offering up to five-fold increase in energy density as compared with state-of-the-art lithium-ion batteries to meet the growing demand for environmentally benign energy storage devices with high energy density, low cost, and long life time. For practical applications, high sulfur (active material) loading ( $> 2 \text{ mg/cm}^2$ ) within the carbon cathode in Li-S batteries is essential. Most reports on engineered cathode materials for Li-S batteries are based upon low sulfur loadings (typically  $\sim 1 \text{ mg/cm}^2$ ), which are

impractical and often give misleading results. It is unknown how these novel engineered cathodes behave under high sulfur loading conditions. The binder is perhaps the most critical material in achieving a high sulfur loading in carbon cathodes. We have recently used dendrimers with various surface chemistries as functional binders in Li-S cells with SuperP-carbon/S as the cathode material. Even without engineering the cathode, very favorable cycling stability and electrolyte wetting were obtained with these binders. It was attributed to the high density of surface functional groups on the dendrimers, high curvature of the binder and its porosity, and the interactions between the large number of basic nitrogen and oxygen atoms on the dendrimers and lithium polysulfides.

Here, we will discuss the fundamental properties of dendrimers as aqueous binders for Li-S battery cathodes and compare their performance with other aqueous, commonly used linear polymeric binders such as styrene butadiene rubber (SBR) and sodium carboxyl methyl cellulose (CMC). Specifically, generation 4 polyamidoamine (PAMAM) dendrimers with hydroxyl (OH), 3-carbomethoxypropylidone (CMP), and sodium carboxylate (COONa) surface functional groups served as good, electrochemically stable binders at high S loadings ( $\sim 3\text{-}5 \text{ mg/cm}^2$ ) with high initial capacities ( $> 1000 \text{ mAh/g}$ ). In comparison to CMC-SBR binder-based electrodes which failed at high C-rates (0.2C) after 40 cycles, dendrimer-based binders showed a capacity retention of  $>85\%$  for more than 100 cycles. It was also observed that acidic groups and all- $\text{NH}_2$  surface groups are poor binders, whereas binders with  $\text{COO}^-$  and neutral surface groups (OH,  $\text{CH}_3$ ) show better performance. X-ray photoelectron spectroscopy was used to identify different surface functional groups in these dendrimers and understand their interactions with SuperP-carbon/S cathode. In addition, a detailed physico-chemical characterization using IR spectroscopy and XANES/EXAFS will be presented to substantiate the superior dendrimer-carbon/S interactions.

4:20pm EN+EM+NS+SE+SS+TF-TuA7 **The Road beyond Lithium Batteries is Paved — In Three Dimensions — With Rechargeable, Dendrite-Free Zinc**, *Debra Rolison, J.F. Parker, C.N. Chervin, I.R. Pala, M.D. Wattendorf, J.W. Long*, U.S. Naval Research Laboratory **INVITED**

Lithium-ion batteries dominate the energy-storage landscape, but do so with the ever-present threat of thermal runaway and conflagration courtesy of flammable electrolytes and oxygen-releasing electrode materials. Fortunately, Zn-based batteries offer a compelling alternative grounded in the innate safety and cost advantages of aqueous electrolytes augmented by the high earth-abundance of Zn and the high energy density of Zn-based batteries (comparable to Li-ion). Traditional Zn-based batteries provide suboptimal utilization of the zinc (typically  $<60\%$  of theoretical capacity) and poor rechargeability—thanks to the complex dissolution/precipitation processes that accompany  $\text{Zn}/\text{Zn}^{2+}$  cycling of conventional powder-bed Zn electrode structures in alkaline electrolyte. We address these limitations by redesigning the zinc anode as a porous, 3D-wired "sponge" architecture. Zinc sponge electrodes achieve  $>90\%$  Zn utilization when discharged in primary Zn-air cells, retaining both the 3D framework of the Zn sponge and an impedance characteristic of the metal thanks to an inner metallic core of 3D zinc. When cycled in Ag-Zn and Ni-Zn cells, the Zn sponges retain monolithicity and reveal uniform deposition of charge/discharge products at the external and internal surfaces, even to deep depth-of-discharge of the zinc. These results show that all Zn-based chemistries can now be reformulated for next-generation rechargeable, Li-free batteries

5:00pm EN+EM+NS+SE+SS+TF-TuA9 **Porous Silicon Electrochemical Capacitor Devices for Integrated On-Chip Energy Storage**, *Donald Gardner, C.W. Holzwarth III, Y. Liu, S. Clendinning, W. Jin, B.K. Moon, Z. Chen, E.C. Hannah, T.V. Aldridge*, Intel Corp, *C.P. Wang, C. Chen*, Florida International University, *J.L. Gustafson*, Intel Corp

Integrated on-chip energy storage is increasingly important in the fields of internet of things (IoT), energy harvesting, and sensing. Silicon is already the materials of choice for the integrated circuits found in every IoT device; however, the efforts to integrate electrochemical (EC) capacitors on a silicon die have been limited. Unlike batteries, EC capacitors are electrostatic devices and do not rely on chemical reactions enabling cycle lifetimes of  $>1\text{M}$ . This is especially important for off-power-grid IoT devices where difficulty associated with regularly replacing the batteries of billions of devices is prohibitive. This work demonstrates electrochemical capacitors fabricated using porous Si nanostructures with extremely high surface-to-volume ratios and an electrolyte. Devices were fabricated with tapered channels sized from 100 nm at the top to 20 nm and with aspect ratios greater than 100:1. Surface coatings were necessary for long-term stability because unpassivated silicon structures react with the electrolytes. To obtain uniform coatings using stop-flow atomic layer deposition (ALD), efficient surface reactions are needed between high volatility, low molecular

weight, small molecular diameter precursors without chemical vapor deposition side reactions.  $\text{TiCl}_4$  and  $\text{NH}_3$  precursors were found to coat porous Si with TiN uniformly. Measurements of coated P-Si capacitors reveal that an areal capacitance of up to  $6 \text{ mF/cm}^2$  can be achieved using  $2 \mu\text{m}$  deep pores, and scales linearly with depth with  $28 \text{ mF/cm}^2$  measured for  $12 \mu\text{m}$  deep pores. Three-terminal CV measurements with EMI- $\text{BF}_4$  ionic electrolyte were used to examine the stability of different pore sizes and TiN coating thicknesses. Pores with an average  $50 \text{ nm}$  width and 100:1 aspect ratio were stable to  $\pm 1.2 \text{ V}$  when cycled at  $10 \text{ mV/s}$  and stable to  $\pm 1.0 \text{ V}$  when cycled at  $1 \text{ mV/s}$ . Different ionic liquids were studied to determine the ionic liquid best suited to TiN coated porous Si including TEA- $\text{BF}_4/\text{AN}$ , EMI- $\text{BF}_4$ , EMI-Tf, and a 3M EMI- $\text{BF}_4$ /propylene carbonate (PC) mixture. Using impedance spectroscopy, the time constant for a  $2 \mu\text{m}$  deep porous Si EC capacitor with a high conductivity TiN coating was found to be  $17.6 \text{ ms}$  which is fast enough that this can be used for applications involving AC filtering for AC-DC conversion. Measurements of volumetric energy density versus power density of porous Si devices versus other devices show several orders of magnitude higher energy density than electrolytic capacitors with a similar voltage range. These results are also between one to two orders of magnitude higher than other studies utilizing porous silicon and are comparable to commercial carbon-based EC capacitors.

5:20pm **EN+EM+NS+SE+SS+TF-TuA10 Investigations of Magnesium Stripping and Deposition using Operando Ambient Pressure X-ray Photoelectron Spectroscopy**, Yi Yu, Lawrence Berkeley National Laboratory, Q. Liu, Shanghai Tech University, China, B. Eichhorn, University of Maryland, College Park, E.J. Crumlin, Lawrence Berkeley National Laboratory

Since the first demonstration of rechargeable magnesium battery, magnesium metal has been considered as an attractive battery anode due to its high volumetric energy density, high negative reduction potential, natural abundance in the earth crust, and relatively good safety features due to its dendrite-free formation. Although it is well accepted that the dissolution and plating of metal plays an important role in the electrochemical properties related to the discharge and charge of the battery, the nature of metal-electrolyte chemical and electrochemical interaction is still not fully established. In an effort to elucidate the interfacial electrochemical mechanisms, we present the studies of magnesium deposition and stripping using *operando* ambient pressure X-ray photoelectron spectroscopy (AP-XPS). Synchrotron X-rays at the Advanced Light Source, Lawrence Berkeley National Laboratory and our 'tender' X-ray AP-XPS endstation allow for probing the liquid-solid interface at pressures up to 20 Torr. Cyclic voltammetry is employed to examine the reversibility of electrochemical magnesium deposition. This talk will provide details on how *operando* AP-XPS coupled with electrochemistry allows for studying electrochemical processes of magnesium deposition and stripping at the liquid-solid interface and yields chemical information relevant to real-world applications.

5:40pm **EN+EM+NS+SE+SS+TF-TuA11 Atomic Layer Deposition of Solid Electrolytes for Beyond Lithium-Ion Batteries**, Alexander Kozen, G.W. Rubloff, University of Maryland, College Park **INVITED**

Solid Li-based inorganic electrolytes offer profound advantages for energy storage in 3-D solid state batteries: (1) enhanced safety, since they are not flammable like organic liquid electrolytes; and (2) high power and energy density since use of the 3D geometry can maximize the volume of active material per unit area, while keeping the active layer thickness sufficiently small to allow for fast Li diffusion. The quality of thin solid electrolytes is currently a major obstacle to developing these solid state batteries, restricting electrolyte thickness to  $>100 \text{ nm}$  to control electronic leakage, consequently slowing ion transport across the electrolyte and impeding 3-D nanostructure designs that offer high power and energy.

Furthermore, the ion-conducting, electron-insulating properties of solid electrolytes are promising for their use as protection layers on metal anodes (e.g., Li, Na, Mg) and on cathodes in proposed "beyond-Li-ion" battery configurations such as Li-NMC, Li- $\text{O}_2$ , and Li-S to prevent electrolyte breakdown.

Atomic layer deposition (ALD) is well suited to the challenge of solid electrolytes, providing ultrathin, high quality films with exceptional 3-D conformality on the nanoscale. We have developed a quaternary ALD processes for the solid electrolyte LiPON, exploiting *in-operando* spectroscopic ellipsometry and *in-situ* XPS surface analysis for process development. ALD LiPON has tunable morphology, and a nitrogen-dependent tunable ionic conductivity as high as  $3.5 \times 10^{-7} \text{ s/cm}$ .

We explore the potential of ALD solid electrolytes for the fabrication of solid, 3D microbatteries, as well as the use of thin ALD solid electrolyte coatings on metal anodes to improve interfacial stability against organic electrolytes and thus prevent SEI formation. We demonstrate and quantify

protection of lithium metal anodes with low ionic conductivity ALD  $\text{Al}_2\text{O}_3$  coatings to prevent degradation reactions, and probe the surface chemistry and morphology of these anodes. Finally, we demonstrate that protection of Li metal anodes using ALD protection layers can improve the capacity of Li-S batteries by 60% by preventing anode corrosion by dissolved sulfur species in the electrolyte.

This work has implications beyond the passivation of lithium metal besides its focus and greatest impact on the Li-S battery system, as ALD protection layers could also be applied to other promising metal anode battery systems such as Mg and Na, and other beyond Li-ion technologies such as Li-NMC or Li-Air where similar reactivity issues prevent adoption.

## Advanced Surface Engineering

Room: 212A - Session SE+PS-TuA

## Pulsed Plasmas in Surface Engineering

Moderator: Jolanta Klemberg-Sapieha, Ecole

Polytechnique de Montreal, Canada, Michael Stueber,

Karlsruhe Institute of Technology

2:20pm **SE+PS-TuA1 Strategy for Tuning the Average Charge State of Metal Ions Incident at the Growing Film during HIPIMS Deposition**, Grzegorz Greczynski, Linköping University, Sweden, I. Petrov, University of Illinois at Urbana Champaign, J.E. Greene, University of Illinois at Urbana-Champaign, L. Hultman, Linköping University, Sweden

Energy- and time-dependent mass spectroscopy is used to determine the relative number density of singly- and multiply-charged metal ions incident at the substrate during high-power pulsed magnetron sputtering (HIPIMS) as a function of the average noble-gas ionization potential. We selected Ti as the sputtering target since the microstructure, phase composition, properties, and stress-state of Ti-based ceramic thin films grown by HIPIMS are known to be strongly dependent on the charge state of  $\text{Ti}^{n+}$  ( $n = 1, 2, \dots$ ) ions incident at the film growth surface. [1,2] Mass spectroscopy results show that the flux of  $\text{Ti}^{n+}$  with  $n > 2$  is insignificant; thus, the  $\text{Ti}_{2+}/\text{Ti}_+$  integrated flux ratio  $J_{\text{Ti}^{2+}}/J_{\text{Ti}^+}$  is measured at the substrate position as a function of the choice of noble gas -- Ne, Ar, Kr, Xe, as well as Ne/Ar, Kr/Ar, and Xe/Ar mixtures -- supporting the plasma. We demonstrate that by changing noble-gas mixtures,  $J_{\text{Ti}^{2+}}$  varies by more than two orders of magnitude with only a small change in  $J_{\text{Ti}^+}$ . This allows the ratio  $J_{\text{Ti}^{2+}}/J_{\text{Ti}^+}$  to be continuously tuned from less than 0.01 with Xe, which has a low first-ionization potential  $IP^1$ , to 0.62 with Ne which has a high  $IP^1$ . The value for Xe,  $IP^1_{\text{Xe}} = 12.16 \text{ eV}$ , is larger than the first ionization potential of Ti,  $IP^1_{\text{Ti}} = 6.85 \text{ eV}$ , but less than the second Ti ionization potential,  $IP^2_{\text{Ti}} = 13.62 \text{ eV}$ . For Ne, however,  $IP^1_{\text{Ne}} = 21.63 \text{ eV}$  is greater than both  $IP^1_{\text{Ti}}$  and  $IP^2_{\text{Ti}}$ . Therefore, the high-energy tail of the plasma-electron energy distribution can be systematically adjusted, allowing  $J_{\text{Ti}^{2+}}/J_{\text{Ti}^+}$  to be controllably varied over a very wide range, from 0.01 with Xe to 0.62 with Ne. [3]

[1] G. Greczynski, J. Lu, M. Johansson, J. Jensen, I. Petrov, J.E. Greene, and L. Hultman, *Surf. Coat. Technol.* 206 (2012) 4202

[2] G. Greczynski, J. Lu, M. Johansson, J. Jensen, I. Petrov, J.E. Greene, and L. Hultman, *Vacuum* 86 (2012) 1036

[3] G. Greczynski, I. Petrov, J.E. Greene, and L. Hultman, *Vacuum* 116 (2015) 36

2:40pm **SE+PS-TuA2 Study of High Power Pulsed Magnetron Sputtering Under Differing Magnetic Field Configurations**, Priya Raman, I.A. Shchelkanov, J.T. McLain, University of Illinois at Urbana Champaign, S. Armstrong, Kurt J. Lesker Company, D.N. Ruzic, University of Illinois at Urbana Champaign

There is an increasing demand for high quality, wear-resistant, low-friction and corrosion resistant coatings in the microelectronics, automotive, tooling and other industries. High power magnetron sputtering is a type of magnetron sputtering technique where short high power pulses are applied to the magnetron target at very low duty cycles leading to higher degree of ionization of the target material. These ionized sputtered material assist in film growth leading to more adhesive, dense, and smoother films compared to conventional DC Magnetron Sputtering (dcMS) techniques. Unfortunately HPPMS suffers from lower deposition rates due to "return effect" of the ionized sputter materials [1]. Further reach of the HPPMS technology largely depends on whether it can produce deposition rates comparable or higher than dcMS. Recent studies of HPPMS discharges have shown that the magnetic field in the region above the sputter target defines the plasma properties and potential distribution in that region. The "ε" magnet pack [2] had already demonstrated increased deposition rates by



carefully changing the magnetic field pattern above the target surface. Cylindrically symmetric "TriPIMS" magnet was developed based on magnetic field design solutions from "ε" magnet pack to keep the high deposition rates but improve deposition uniformity. In order to fully understand the behaviour of high current pulsed discharge in this new magnetic field configuration, TriPIMS magnet pack, was tested with Huettinger HiPIMS, Z-pulsed MPP, Starfire Impulse and DC power supplies. Plasma parameters (ne, Te, ionization fraction), deposition rate, deposited film density, uniformity, and stress were measured. Reason for higher deposition rate is discussed.

[1] Papa F et al 2011 Thin Solid Films 520.5 1559-1563.

[2] Raman, Priya, et al. "High power pulsed magnetron sputtering: A method to increase deposition rate." *Journal of Vacuum Science & Technology A* 33.3 (2015): 031304.

3:00pm **SE+PS-TuA3 Reactive High-power Impulse Magnetron Sputtering and Pulsed Magnetron Co-sputtering of Multifunctional Films, Jaroslav Vlcek, J.R. Rezek, P.M. Mares, University of West Bohemia, Czech Republic** **INVITED**

In the presentation, we report on discharge and deposition characteristics (including the ion flux characteristics at the substrate), and on film structure and properties for two different pulsed reactive magnetron sputtering techniques.

High-power impulse magnetron sputtering (HiPIMS) with a pulsed reactive gas flow control was used for high-rate reactive depositions of densified, highly optically transparent, stoichiometric ZrO<sub>2</sub> and HfO<sub>2</sub> films, and of Ta-O-N films with tunable composition and properties. The depositions were performed using a strongly unbalanced magnetron with a planar directly water-cooled Zr, Hf or Ta target in Ar-O<sub>2</sub> or Ar-O<sub>2</sub>-N<sub>2</sub> gas mixtures at an average target power density of up to 2.4 kWcm<sup>-2</sup> in a pulse. The repetition frequency of pulses was 500 Hz at 50 – 200 μs voltage pulse lengths and the total pressure close to 2 Pa. An effective reactive gas flow control made it possible to produce high-quality ZrO<sub>2</sub>, HfO<sub>2</sub> and Ta-O-N films with high deposition rates (up to 120 nm/min, 345 nm/min and 190 nm/min, respectively, for the target-to-substrate distance of 100 mm) and to adjust the composition of the Ta-O-N films from Ta<sub>2</sub>O<sub>5</sub> to a mixture of Ta<sub>3</sub>N<sub>5</sub> and TaN. We prepared almost stoichiometric TaON films possessing appropriate band-edge levels for water splitting and a narrow optical band gap of 2.5 eV that permits a visible light absorption up to 500 nm. Selected results obtained using a parametric model for the controlled reactive HiPIMS of the ZrO<sub>2</sub> films are presented.

Pulsed dc magnetron co-sputtering of a single segmented target (B<sub>4</sub>C-M, where M = Ti, Zr and Hf, or B<sub>4</sub>C-Hf-Si) in Ar gas or Ar-N<sub>2</sub> gas mixtures was used for deposition of different multifunctional films. The repetition frequency of pulses was 10 kHz at a fixed 85 μs voltage pulse length and the total pressure of 0.5 – 1.7 Pa. Energy-resolved mass spectroscopy was used to correlate the energy of Ar<sup>+</sup> ions bombarding the growing films with high positive voltage overshoots after the negative voltage pulses and with the energy of Ar atoms backscattered from the sputtered targets. We present the results obtained for nanocolumnar ZrB<sub>2</sub>-type Zr-B-C films and nanocomposite Zr-B-C-N films exhibiting a high hardness (37 GPa) and high electrical conductivity, and for nanostructured HfB<sub>2</sub>-type Hf-B-Si-C films with a high hardness (34 – 37 GPa), high electrical conductivity and significantly improved oxidation resistance in air up to 800 °C.

4:20pm **SE+PS-TuA7 Target Poisoning in Mixed Ar, N<sub>2</sub> and CH<sub>4</sub> Atmosphere, in Processes Using Different Target Materials for HIPIMS/DC and DC Cathode Modes. Anna Oniszczuk, A.P. Ehiasarian, Sheffield Hallam University, United Kingdom of Great Britain and Northern Ireland, C.F. Carlström, M. Ahlgren, Sandvik Coromant, Sweden**

Reactive sputtering in mixed Ar+N<sub>2</sub>+CH<sub>4</sub> atmosphere is a widely used industrial process however the poisoning of different target materials under different sputtering discharges in this complex environment is insufficiently described.

In mixed Ar+CH<sub>4</sub>+N<sub>2</sub> atmosphere, at low flow processes were influenced by methane whereas at high flow they were dominated by nitrogen indicating the formation of carbide and then carbonitride compounds. This was observed for both TiAl and V targets in DC as well as in HIPIMS mode.

Vanadium targets operating in DC mode were poisoned at 55% of reactive gas flow. Poisoning resulted in a 2-fold increase in total pressure, a 50 % increase in discharge voltage/current ratio, a 5 fold drop in V(I) optical emission intensity and a 10 fold drop in V<sup>+</sup> and Ar<sup>+</sup> fluxes obtained from energy-resolved mass spectroscopy.

TiAl targets in DC mode poisoned at lower reactive gas flows and exhibited narrower hysteresis than V due to the higher reactivity of the target material. The voltage/current ratio of TiAl targets went through a minimum with a flow, while for V target it increased with flow.

For HIPIMS both targets poisoned earlier and the hysteresis was narrower than in DC mode. As confirmed by trends in the partial pressure, the voltage/current ratio and ion fluxes of metals and reactive gasses. These effects are due to higher reactivity of the plasma as evidenced by higher fluxes of N<sup>+</sup> and N<sub>2</sub><sup>+</sup> and radicals containing H, C and N. The voltage/current ratio reduced by 50% as the target is poisoned in contrast to operation in DC mode where it increased. This could be attributed to efficient ionization and drop in plasma impedance.

Pathways for poisoning and resulting ion fluxes are discussed.

4:40pm **SE+PS-TuA8 Structure and Properties of Cr<sub>2</sub>O<sub>3</sub> Coatings Deposited using DCMS, PDCMS, and DOMS, Jianliang Lin, Southwest Research Institute, W.D. Sproul, Reactive Sputtering, Inc.**

The properties of oxide coatings are strongly tied to the crystallinity of oxide phases. In general, a well-crystallized oxide phase is desired because it is usually related to improved mechanical and chemical properties. This paper presents a comparative study of the chromium oxide (Cr<sub>2</sub>O<sub>3</sub>) coatings deposited by deep oscillation magnetron sputtering (DOMS), mid-frequency pulsed dc magnetron sputtering (PDCMS) and continuous dc magnetron sputtering (DCMS). Without applying external substrate heating, the processing techniques strongly affected the crystallinity of the Cr<sub>2</sub>O<sub>3</sub> coatings. The DCMS-Cr<sub>2</sub>O<sub>3</sub> coating exhibited an amorphous like structure. The coating deposited by PDCMS contained a mixture of amorphous and crystalline phases. In contrast, the DOMS-Cr<sub>2</sub>O<sub>3</sub> coating showed a strong crystallinity with a (110) preferential orientation. The improved crystallinity of the DOMS-Cr<sub>2</sub>O<sub>3</sub> coating is due to the higher ion bombardment and higher substrate saturation temperature, which is related to the high energy electron bombardment associated with deep oscillation pulses. Improved mechanical properties and wear resistance were achieved in the DOMS-Cr<sub>2</sub>O<sub>3</sub> coatings as compared to the coatings deposited using DCMS and PDCMS. This study also showed that the bias voltage strongly affected the structure of the DOMS-Cr<sub>2</sub>O<sub>3</sub> coatings by changing the substrate current characteristics.

5:00pm **SE+PS-TuA9 Strategy to Tailor the Composition of Silicon Oxynitride Thin Films Deposited by Reactive High Power Impulse Magnetron Sputtering using Nitrous Oxide as a Single-source Precursor, Tuomas Hänninen, S. Schmidt, J. Jensen, L. Hultman, H. Högberg, Linköping University, Sweden**

Silicon oxynitride (SiON) is a material with tunable optical and electrical properties. It is used as thin films in antireflection coatings, surface passivation layers, and optical waveguides. Commonly two reactive gases, O<sub>2</sub> and N<sub>2</sub>, have been employed for the reactive magnetron sputter deposition of SiON. The two-gas approach is, however, limited by the non-linear target effects as a function of reactive gas flow rates, which makes an accurate control of the deposition process challenging.

In this study we present SiON thin films deposited by reactive high power impulse magnetron sputtering from a pure Si target in Ar/N<sub>2</sub>O plasmas. The influence of the average target power while maintaining a fixed pulse frequency (1000–4000 W at 1000 Hz and 1200–3000 W at 600 Hz) and the frequency at a fixed energy per pulse (300–1000 Hz at 4 J) on the resulting film properties were investigated.

The ~ 300 nm thick films show a dense and featureless morphology when viewed in cross-sectional scanning electron microscopy. X-ray diffraction reveals that the films are X-ray amorphous and exhibit compressive residual stresses in the range of 500–1500 Mpa. The chemical bonding structure and the elemental composition of the films were studied with X-ray photoelectron spectroscopy. The spectra acquired from the as-deposited samples show mixed Si—O, Si—N, and Si—Si bonding. The ratio between these type of bonds correlates with the atomic concentrations of Si, O, and N in the films. A decreased average power at a fixed pulse frequency induces an increase in O content (from 13 at.% to 51 at.% at 1000 Hz and from 17 at.% to 43 at.% at 600 Hz) while the N concentration remains virtually unaffected. An exception are films with the highest O content, showing a decrease in N content from ~ 26 at.% to 9 at.% at 1000 Hz and to 16 at.% at 600 Hz. A similar behavior is observed when the pulse frequency is lowered at a constant pulse energy, the film O content increases from 13 at.% to 43 at.%, followed by a decrease in N concentration from ~ 26 at.% to 17 at.%. Film densities as measured by X-ray reflectivity are found to range between 2.6–2.9 g/cm<sup>3</sup>. The refractive indices and extinction coefficients at 633 nm, measured by variable-angle spectroscopic ellipsometry, show that the films with highest total O plus N content have the lowest refractive index (1.6–1.8) and extinction coefficient (~ 0) values. The refractive index values are comparable to those of SiO<sub>2</sub> (~ 1.45) and Si<sub>3</sub>N<sub>4</sub> (~ 2.0), confirming that the optical properties of the studied films can be tailored to range between SiO<sub>2</sub> and Si<sub>3</sub>N<sub>4</sub>.

5:20pm **SE+PS-TuA10 Phase Changes Observed on AlCr Composite Cathodes due to the Exposure to Cathodic Arc Plasmas in N<sub>2</sub> and O<sub>2</sub> Atmospheres**, Robert Franz, F. Mendez Martin, G. Hawranek, Montanuniversität Leoben, Austria, P. Polcik, PLANSEE Composite Materials GmbH, Germany

Hard and wear-resistant coatings based on the system aluminium and chromium represent the state of the art in the protection of tools used in metal cutting operations. Using cathodic arc deposition techniques in nitrogen and/or oxygen atmospheres, nitrides, oxides or oxynitrides can be synthesised. The growth conditions encountered in processes employing cathodic arc plasmas are typically characterised by a high degree of ionisation and high deposition rates. For the supply of the non-gaseous elements during the deposition, it is common to use multi-element cathodes containing the desired Al/Cr ratio. These cathodes are usually composite cathodes and are widely used in industrial-scale deposition systems since they facilitate an easier process control and reproducibility. However, the plasma conditions in the cathodic arc plasma using such multi-element cathodes and their erosion behaviour in reactive atmospheres are only scarcely studied.

In the present investigation, AlCr composite cathodes with compositions of 75/25, 50/50 and 25/75 at.-% were exposed to cathodic arc plasmas in N<sub>2</sub> and O<sub>2</sub> atmospheres. Due to periodic melting and solidification of the cathodes' near-surface region in the cathode spots, an intermixing of the elements Al and Cr and the formation of intermetallic phases occurred which was analysed by recording elemental distribution maps in the cross-sections using scanning electron microscopy. By comparing regions of strong erosion with areas less affected by the cathodic arc plasma, poisoning effects due to reactions of the metals in the cathodes and the background gas could be identified and were analysed in detail. The conductivity of the formed nitrides and oxides on the surface of the AlCr composite cathodes was decisive for the characteristics of the cathodes' erosion behaviour. All results regarding the cathode erosion and the phase changes are compared to similar studies on TiAl [1] and Al<sub>0.7</sub>Cr<sub>0.3</sub> [2, 3] cathodes and are put in context with recently reported arc plasma properties obtained with the same AlCr cathodes and gas atmospheres [4, 5].

#### References:

- [1] D. Rafaja, C. Polzer, G. Schreiber, P. Polcik, M. Kathrein, Surf. Coat. Technol. 205 (2011) 5116–5123.
- [2] J. Ramm, A. Neels, B. Widrig, M. Döbeli, L.D.A. Vieira, A. Dommann, H. Rudigier, Surf. Coat. Technol. 205 (2010) 1356–1361.
- [3] M. Pohler, R. Franz, J. Ramm, P. Polcik, C. Mitterer, Surf. Coat. Technol. 206 (2011) 1454–1460.
- [4] R. Franz, P. Polcik, A. Anders; *IEEE Trans. Plasma Sci.* 41 (2013) 1929–1937
- [5] R. Franz, P. Polcik, A. Anders; *Surf. Coat. Technol.* 272 (2015) 309–321

5:40pm **SE+PS-TuA11 Optimization of Linear Scanning Magnetron Array Performance**, Vladimir Kudriavtsev, A. Ripsan, D.W. Brown, C. Smith, T. Bluck, Intevac, Inc.

In this presentation we discuss Linear Scanning Magnetic Array (LSMA) technology for magnetron sputtering in conjunction with in-line substrate processing. In this approach, the magnet array (pole) scans over planar target spreading the erosion pattern in a controlled fashion. Thus, high quality, dense films with good uniformity can be produced at significant advantages over static magnetrons, such as significantly higher target utilization, longer uptime, and prevention/removal of target defects related to re-deposition.

We review the influence of magnet motion acceleration/deceleration, the influence of endpoint motion offset (stagger), and the influence of magnet - to - substrate velocity ratio, on target utilization and lead-to-trail edge film uniformity. Trade-offs between uniformity and target utilization were established and characterized.

The optimization method we use employs a combination of theoretical simulations and experimental measurements. Theoretical analysis utilizes ANSYS static magnetic field simulations, erosion profile calculations including motion integration effects, and ray tracing method for sputtering film thickness calculations (MATLAB). The structure and uniformity of LSMA-deposited thin films was characterized experimentally by XRF and SEM, and the target erosion measured by weight and erosion profiles of spent targets.

We have demonstrated that, with a judicious design approach, an optimal range of operating parameters can be defined and target utilizations above 70% can be reached, while maintaining deposition uniformity below 2% with excellent film properties. This makes the LSMA plasma source (using planar targets) more economically competitive than static and rotatable magnetrons.

6:00pm **SE+PS-TuA12 Correlation of Microstructure of Deposited Thin Films with Discharge Characteristics by Modulated Pulsed Power Magnetron Sputtering (MPPMS)**, M.K. Lei, Dalian University of Technology, China

Pure Cu thin films and TiAlSiN nanocomposite thin films are deposited in a closed field unbalanced magnetron sputtering system using the modulated pulsed power magnetron sputtering (MPPMS), in order to understand the correlation of the microstructure and texture of deposited thin films with the discharge characteristics by MPPMS. The discharge processes at different pressures on the metallic targets are numerically modeled with considering the loss of electrons by cross-B diffusion. With increasing the pressure from 0.1 to 0.7 Pa, both the ion bombardment energy and substrate temperature which are estimated by the modeled plasma parameters decrease, corresponding to the observed transition of the deposited Cu thin films from a void free structure with a wide distribution of grain size into an underdense structure with a fine fiber texture in the extended structure zone diagram. The TiAlSiN thin films are deposited at the ratio of the nitrogen flow rate to the total gas flow rate ( $f_{N_2}$ ) ranging from 0 to 40%. An optimized nanocomposite structure of *nc*-TiAlN/*a*-Si<sub>3</sub>N<sub>4</sub> is formed with the 5–10 nm TiAlN nanocrystallites embedded in the 2–3 nm amorphous Si<sub>3</sub>N<sub>4</sub> matrix. Further increasing  $f_{N_2}$  up to 40%, the grain size of nanocrystallites increase to 10–20 nm with the gradually precipitation of AlN phase, albeit the composition keeps constant. With increasing the partial pressure, the increased ion bombardment energy and substrate temperature are believed to be responsible for the complete phase separation of the *nc*-TiAlN/*a*-Si<sub>3</sub>N<sub>4</sub> nanocomposite thin films.

# Tuesday Evening Poster Sessions

## Advanced Surface Engineering

Room: Hall 3 - Session SE-TuP

### Advanced Surface Engineering Poster Session

**SE-TuP1 Surface and Tribological Properties of CF<sub>x</sub>-doped TaN Thin Films With and Without CF<sub>x</sub> Top Layer**, *W.C. Say, ShangLun Liu*, National Taipei University of Technology, Taiwan, Republic of China, *J.H. Hsieh*, Ming Chi University of Technology, Taiwan, Republic of China

TaN thin film coatings are known to have good mechanical properties, impact toughness, as well as good biocompatibility. However, the friction coefficient of these films is sometimes too high, or the hemocompatibility is poor. The purpose of this study is to reduce the friction coefficient and lower the surface energy of TaN coating by introducing CF<sub>x</sub> into/onto the nitride coatings. CF<sub>x</sub>-doped TaN films, with and without CF<sub>x</sub> top layer, were deposited on silicon and tool steel substrates by magnetron sputtering. During the deposition process, C<sub>2</sub>F<sub>6</sub> gas with various flow rates was added. During the deposition of 30 nm CF<sub>x</sub> top layer on some samples, the power to Ta target was shut off. After deposition, these films were then characterized using XRD, XPS, FTIR, FESEM, as well as a tribometer. The tribo-tests were carried out with and without argon flow. Surface energies of the films were also analyzed with contact angle measurement system. According to structural analysis, TaN phase would transform to Ta(FCN) with the increase of the fluoride gas flow rate, which would cause the decrease of friction coefficient and surface energy. According to the results obtained from tribotesting, it is found the increase of CF<sub>x</sub> would reduce the effects of moisture and oxygen on friction coefficient. The prepared films may have good hemocompatibility and wear-resistance.

**SE-TuP2 Biocompatibility of Porous TaO<sub>x</sub>N<sub>y</sub> Films with Various O/N Ratio**, *J.H. Hsieh, YiChih Lin, S.J. Liao*, Ming Chi University of Technology, Taiwan, Republic of China, *C. Li*, National Yang Ming University, Taiwan, Republic of China, *Y.H. Lai*, Ming Chi University of Technology, Taiwan, Republic of China

The oxynitride of a transition metal is able to form a new grade of functional thin film. Controlling oxygen-to-nitrogen ratio allows one to tune the film properties. The tunable properties include optical and mechanical properties, and biocompatibility, etc. In this study, TaO<sub>x</sub>N<sub>y</sub>-Cu films were first prepared using reactive co-sputtering, with the variation of O/N flow ratios. After deposition, the films were annealed, and Cu was etched away to form porous oxynitride structures with various O/N ratio. The films were characterized using nano-indentation, XRD, and SEM. The results showed that the porosity of these films could be varied depending on Cu contents and O/N ratios. The samples were then tested for their biocompatibility and viability using 3-T-3 fibroblast cells. According to the results obtained from biocompatibility and MTT assay testing, it was found that the O/N ratio should be near the transition of semiconductor to conductor. Furthermore, the pore size played a major role in terms of biocompatibility and cell viability. An optimal pore size was found around 200 μm.

**SE-TuP3 Nanopatterned ZnO on PDMS via Decoupled Ion Beam Modification and Metal Co-Deposition**, *Zachariah Koyn, B. Holybee, A. Shetty, K. Nash, J. Pachicano*, University of Illinois at Urbana-Champaign, *S. Srivastava*, Illinois Applied Research Institute, *J.P. Allain*, University of Illinois at Urbana-Champaign

Ion beams have been shown to create nano-scale surface patterning on polycrystalline thin metal films, including ripples and dots [1,2]. Additionally, oxygen ion beams have been shown to induce fluence-dependent surface oxidation on metal surfaces [3]. This work seeks to unravel the directed irradiation synthesis of metal oxide thin-films, specifically ZnO, with irradiation-driven mechanisms on dissimilar, polymer-based substrates. This examines the dual effects of oxygen irradiation as a method of both oxidizing and patterning metal thin-films at ambient temperatures. This represents a scalable process in growing and functionalizing metal-oxide thin-films on polymers, which are sensitive to the high temperatures required in thermal oxidation processes. Recent work utilized a single ion beam to simultaneously irradiate and sputter deposit metal impurities on Si, creating nanostructures [4]. The work here decouples these processes by using two ion beams to independently control the metal deposition and surface modification fluxes. The ratio of these is the primary tool used to explore the creation and control over size and shape of nanostructures. Beam energies of 100-2000 eV are used at ambient temperatures to protect the substrate, with an inert beam used for metal deposition and both inert and reactive (O<sub>2</sub><sup>-</sup>) normal incidence beams used for surface modification. Both Si and PDMS substrates are explored with fluences of ~5E16–2E17 ions/cm<sup>2</sup>. Surface patterning and chemistry are

analyzed with AFM and XPS, respectively. The ability to functionalize flexible, transparent substrates with metal-oxide nanostructures offers exciting applications in areas such as flexible and wearable electronics, gas sensors, biosensors, and photonics [5].

[1] D. Ghose, *J. Phys. Condens. Matter* **21**, 224001 (2009).

[2] P. Gailly, C. Petermann, P. Tihon, and K. Fleury-Frenette, *Appl. Surf. Sci.* **258**, 7717 (2012).

[3] N. V. Alov, *Nucl. Instruments Methods Phys. Res. Sect. B Beam Interact. with Mater. Atoms* **256**, 337 (2007).

[4] K. Zhang, M. Brötzmann, and H. Hofsäss, *AIP Adv.* **2**, 0 (2012).

[5] I.-S. Hwang, Y.-S. Kim, S.-J. Kim, B.-K. Ju, and J.-H. Lee, *Sensors Actuators B Chem.* **136**, 224 (2009).

**SE-TuP4 Investigation of Tungsten-YttriumBased Structural Materials for Nuclear Reactor Applications**, *Gustavo Martinez, J. Chessa*, University of Texas at El Paso, *M. Lerche*, Mccllellan Nuclear Research Center, *R.V. Chintalapalle*, University of Texas at El Paso

Material failure is one of the most considerable setbacks needed to be addressed by the materials research community to develop the next generation of nuclear energy systems that demand materials to serve under extreme conditions. We report on the enhanced irradiation tolerance and phase stability of nanocrystalline Tungsten-Yttrium (W-Y) coatings produced by radio-frequency sputter deposition. The W-Y coatings were produced under variable sputtering pressure and Y-content. The coatings were characterized by studying their structure and mechanical properties. The W-Y coatings were then subjected to heavy ion-irradiation at high fluence levels. The addition of Y atoms into the W matrix has shown to improve the irradiation bombardment of heavy Au+3 and yielding improved young's modulus and hardness when compared to pure W alone. It is believed that the addition of Y creates grain boundaries that are capturing interstitial ions and recombining to eliminate vacancies. The results will be presented and discussed.

**SE-TuP6 The Influence of Mo Content and Bias Potential on the Structure, Mechanical Properties, and Tribological Behaviour of Cathodic Arc Evaporated Ti-Al-N Hard Coatings**, *Stefan A. Glatz*, TU Wien, Austria, *C.M. Koller*, *H. Riedl*, CDL AOS, TU Wien, Austria, *R. Rachbauer*, Oerlikon Balzers, Oerlikon Surface Solutions AG, Liechtenstein, *S. Kolozsvári*, Plansee Composite Materials GmbH, Germany, *P.H. Mayrhofer*, CDL AOS, TU Wien, Austria

Today's industrial processes, i.e. forming and shaping of various materials, require efficiency and precision. Therefore, wear and friction are core topics in the continuous improvement process. Coating either one of the counter-bodies or both of them with, for example, Ti-Al-N can be a feasible solution for fitting these certain requirements of the tribological conditions within industrial processes. Powder metallurgical manufacturing is ideal to produce materials with a broad composition and/or to alloy further elements to a standard target composition—i.e. to alter the properties of Ti<sub>1-x</sub>Al<sub>x</sub>N thin films. This study focuses on the influence of bias potential and alloying element content on phase formation, mechanical properties, and tribological behaviour of cathodic arc evaporated (Ti<sub>0.5</sub>Al<sub>0.5</sub>)<sub>1-x</sub>Mo<sub>x</sub>N hard protective coatings. The tribological behaviour of the coatings obtained by using this physical vapour deposition (PVD) technique were evaluated by means of pin-on-disc tests and by non-contact optical profilometry—where the development of the wear tracks and counter-bodies is investigated. Scanning electron microscopy in combination with energy dispersive x-ray spectroscopy and x-ray diffraction experiments are performed to establish the chemical and structure evolution of our (Ti<sub>0.5</sub>Al<sub>0.5</sub>)<sub>1-x</sub>Mo<sub>x</sub>N thin films deposited with various bias potentials. It can be shown that the tribological behaviour of Ti-Al-N coatings can significantly be enhanced by the development of (Ti<sub>0.5</sub>Al<sub>0.5</sub>)<sub>1-x</sub>Mo<sub>x</sub>N thin films.

**SE-TuP7 High-temperature Tribological Investigations of CrAlN and CrAlSiN in Ambient and Inert Atmospheres**, *Marisa Rebelo de Figueiredo*, *A. Xia*, Montanuniversität Leoben, Austria, *S. Kolozsvári*, Plansee Composite Materials GmbH, Germany, *R. Franz*, Montanuniversität Leoben, Austria

CrAlN-based hard coatings are nowadays widely used in industrial cutting applications to protect the base material of the tools against wear and oxidation. Due to alloying of the binary CrN with Al, enhanced mechanical properties of CrAlN could be achieved as a result of solid solution hardening, if the face-centered cubic structure of CrN is retained, i.e. Al atoms substitute Cr in the crystal lattice. An improved oxidation resistance is based on the formation of thin oxide layers on the coating's surface hindering further oxidation. With the addition of Si, a nanocomposite of

crystalline CrAl(Si)N grains and an amorphous SiN<sub>x</sub> grain boundary phase can be formed resulting in a further enhancement of the mechanical properties. The oxidation resistance could also be further improved due to the formation of an additional SiO<sub>x</sub> phase on the coating surface. The tribological properties of these coatings at high temperature have already been studied in detail [1, 2]. However, these experiments were performed in ambient atmosphere impeding a clear identification of the main wear mechanism like abrasive or oxidative wear. Even though CrAlN and CrAlSiN are oxidation resistant at the test temperatures up to 700 °C, oxidation in the tribological contact zone might still play an important role if the protective oxide layer on the surface is removed and freshly exposed coating material can rapidly oxidize.

Therefore, CrAlN and CrAlSiN coatings were analyzed in ball-on-disk tests in ambient and inert Ar (+ N<sub>2</sub>) atmosphere at temperatures ranging from room temperature up to 700 °C. The coatings were synthesized by DC magnetron sputter deposition in an industrial-scale system using composite Cr<sub>50</sub>Al<sub>50</sub> and Cr<sub>45</sub>Al<sub>45</sub>Si<sub>10</sub> targets. The tribological tests against alumina counterparts revealed a coefficient of friction independent of the used atmosphere. The wear coefficient as determined by 3D optical profilometry, however, showed a non-uniform behavior. At medium temperature of about 400 °C higher wear in inert than oxidative atmosphere was noticed, whereas the opposite trend was observed at high temperatures of up to 700 °C. A subsequent analysis of the wear scars and the wear debris by scanning electron microscopy and Raman spectroscopy revealed further details about the wear mechanisms.

[1] A.E. Reiter, C. Mitterer, M. Rebelo de Figueiredo, R. Franz, Tribol. Lett. 37 (2010) 605–611.

[2] T. Polcar, A. Cavaleiro, Surf. Coatings Technol. 206 (2011) 1244–1251.

# Wednesday Morning, October 21, 2015

## Plasma Science and Technology

Room: 210B - Session PS+2D+SE-WeM

## Plasma Diagnostics, Sensors and Control II

Moderator: Colin Wolden, Colorado School of Mines

8:20am **PS+2D+SE-WeM2 Diagnostics for Ionized Physical Vapor Deposition Chambers**, *YuiLun Wu, P. Piotrowicz*, University of Illinois at Urbana-Champaign, *I.A. Shehelkanov*, National Nuclear Research University (MEPhI), *D.N. Ruzic*, University of Illinois at Urbana-Champaign

As the critical dimension of the semiconductor device continues to shrink and aspect ratio continues to rise, more diagnostics are needed to accurately predict the deposition profile of features on the wafer. Traditionally, the incident ion fluxes are considered to be perfectly normal to the wafer plane due to the electric field of the plasma sheath. However from simulation results [1] the ion flux from a magnetron discharge has a narrow angular distribution and this distribution is becoming more significant as the aspect ratio increases. In order to confirm and adjust this predicted distribution a sensor to measure angular distribution of ions in an industrial scale chamber is designed and developed. The sensor is a combined gridded energy analyzer (GEA) and a quartz crystal microbalance (QCM) [2], with a high aspect ratio collimator in place of the normal electron repeller grid for angular measurement distribution measurements. The collimator is made of 3D-printed plastic elements with 600 $\mu$ m nominal openings which provides 1 degree angular resolution. This combined QCM and GEA setup is capable to determine fluxes of metal ions, metal atoms and argon ions at 30kW DC magnetron nominal target power. The setup is able to tilt around 10 degrees about the wafer plane in 1 degree intervals and measure the angular distribution of the ion and neutral fluxes generated by the discharge. A time resolved triple Langmuir probe was also employed to measure the plasma parameters such as electron temperature and density and scanning in a three dimensional map.

References:

1. Stout, P. J., et al. "Comparing ionized physical vapor deposition and high power magnetron copper seed deposition." *Journal of Vacuum Science & Technology B* 20.6 (2002): 2421-2432.
2. Meng, Liang, et al. "Downstream plasma transport and metal ionization in a high-powered pulsed-plasma magnetron." *Journal of Applied Physics* 115.22 (2014): 223301.

8:40am **PS+2D+SE-WeM3 Probing the Plasma Chemistry that Underpins Diamond Chemical Vapour Deposition**, *Michael Ashfold*, University of Bristol, United Kingdom and Northern Ireland and *M.W. Kelly, B.S. Truscott*, University of Bristol, UK, United Kingdom of Great Britain and Northern Ireland, *Y.A. Mankelevich*, Moscow State University, Russia, Russian Federation

**INVITED**

Most diamond chemical vapour deposition (CVD) employs microwave (MW) activated C/H (typically CH<sub>4</sub>/H<sub>2</sub>) gas mixtures. Many previous studies have sought to explore (and optimise) radical formation in such activated gas mixture, and the ways in which these radicals add to, and are accommodated on and in, the growing diamond surface.

Our activities in this area employ an interrelated three-pronged approach, *i.e.*

i) electronic spectroscopy methods (cavity ring down absorption and optical emission spectroscopies) to determine the spatial distributions of selected species (*e.g.* H atoms, CH and C<sub>2</sub> radicals) as functions of process variables like the process gas mixing ratio, flow rate and total pressure, and MW power,

ii) complementary 2-dimensional (2-D) modelling of the plasma chemistry and composition with the aim not just of rationalising the spatial resolved column density data obtained in (i), but also enabling prediction of the concentrations of other key gas phase species (*e.g.* CH<sub>3</sub> radicals, which are generally regarded as the dominant growth species) that are not amenable to spectroscopic detection, as functions of process condition, and

iii) quantum mechanical (QM) and QM-molecular mechanics (MM) calculations of the energetics of the elementary steps involved in radical addition to, migration on, and eventual accommodation on, a growing diamond surface.

This invited presentation will summarise the current understanding of diamond CVD from traditional C/H gas mixtures and results of recent studies designed to explore and explain the significant growth rate

enhancements that can be achieved by adding trace amounts of nitrogen to such gas mixtures.

9:20am **PS+2D+SE-WeM5 Ionization Zones and the Deposition of Thin Films in the Transition Region from Non-Reactive to Reactive Magnetron Sputtering including dc, HiPIMS, and Burst-HiPIMS Modes**, *Yuchen Yang, X. Zhou, A. Anders*, Lawrence Berkeley Lab, University of California, Berkeley

Research has been done for copper and chromium targets in conventional non-reactive HiPIMS, revealing the disappearance of localized ionization zones when operating at high power due to high metal neutral supply from the target. However, relatively little research has been done for reactive HiPIMS. In this work we investigate the existence of ionization zones in various forms of reactive magnetron sputtering: direct current (dc) and HiPIMS for conventional pulse patterns and in burst mode. Copper and chromium targets are selected with nitrogen as reactive gas because (i) in the non-reactive regime Cu and Cr can be operated with or without ionization zones, and (ii) these target materials form application-relevant compound films, *e.g.* of interest in wear and corrosion-resistant applications, medical implants, metallization layers, etc.

Work at LBNL is supported by the U.S. Department of Energy under Contract No. DE-AC02-05CH11231.

11:00am **PS+2D+SE-WeM10 Modelling of the Reactive High Power Impulse Magnetron Sputtering (HiPIMS) process**, *JonTomas Gudmundsson*, University of Iceland, *D. Lundin*, Université Paris-Sud, France, *N. Brenning*, KTH Royal Institute of Technology, Sweden, *T. Minea*, Université Paris-Sud, France

Reactive high power impulse magnetron sputtering (HiPIMS) [1] provides both a high ionization fraction of the sputtered material and a high dissociation fraction of the molecular gas. We demonstrate this through an ionization

region model (IRM) [2] of the reactive Ar/O<sub>2</sub> HiPIMS discharge with a titanium target that was developed to study the temporal behavior of the discharge plasma parameters. We explore the influence of oxygen dilution on the discharge properties such as electron density, the ionization fraction of the sputtered vapour, the oxygen dissociation fraction and the onset and role of self sputtering. We discuss the important processes and challenges for more detailed modeling of the reactive HiPIMS discharge. Furthermore, we discuss experimental observations during reactive high power impulse magnetron sputtering (HiPIMS) of Ti target in Ar/N<sub>2</sub> and Ar/O<sub>2</sub> atmosphere. The discharge current waveform is highly dependent on the reactive gas flow rate, pulse repetition frequency and discharge voltage. The discharge current increases with decreasing repetition frequency. This we attribute to an increase in the effective secondary electron emission yield during the self-sputtering phase of the pulse, as nitride [3] or oxide [4] forms on the target.

[1] J. T. Gudmundsson, N. Brenning, D. Lundin and U. Helmersson, *J. Vac. Sci. Technol. A*, 30 030801 (2012)

[2] M. A. Raadu, I. Axnäs, J. T. Gudmundsson, C. Huo and N Brenning, *Plasma Sources Science and Technology*, 20 065007 (2011) 065007

[3] F. Magnus, O. B. Sveinsson, S. Olafsson and J. T. Gudmundsson, *J. Appl. Phys.*, 110 083306 (2011)

[4] F. Magnus, T. K. Tryggvason, S. Olafsson and J. T. Gudmundsson, *J. Vac. Sci. Technol.*, 30 (2012) 050601

11:20am **PS+2D+SE-WeM11 Pulsed Magnetron Sputtering Plasma Optimization for Large Area Growth of Two-dimensional MoS<sub>2</sub>**, *Andrey Voevodin*, Air Force Research Laboratory, *C. Muratore*, University of Dayton, *A.R. Waite, J. Bultman, A. Safriet, J. Hu*, Air Force Research Laboratory

Pulsed magnetron sputtering process provides an alternative scalable and reduced temperature growth pathway for the direct synthesis of two-dimensional (2D) materials for electronic device applications [1]. To avoid defect generation by excessive ion bombardment, while maintaining sufficient adatom mobility on the condensation surface at low substrate temperatures, the ion flux and kinetic energy must be modulated. In this study a variable intensity magnetic field was used to control chemistry, energy, and spatial density distribution characteristics of plasma produced by pulsed magnetron sputtering of MoS<sub>2</sub> in 15 mTorr argon. An electromagnetic coil positioned above the substrate generated a 5-15 G magnetic field near substrate surface, causing redirection of magnetron particle flux for tuning of electron and ion densities at the substrate surface. Both plasma emission and mass-spectroscopy analysis showed an abundance of excited and ionized Ar as well as Mo and S species with no

evidence for MoS radicals. Wavelength specific plasma imaging and mass/energy spectroscopy studies demonstrated that the applied magnetic field mostly affects excited and ionized Ar generated in background gas collisions with electrons trapped by the magnetic field lines, while the trajectories of Mo and S species generated from the target surfaces are influenced to a much lesser degree. The imposed magnetic field intensity was adjusted to selectively filter Ar species from reaching the substrate and to find a balance between reducing unnecessary Ar bombardment and preventing shifting energy distributions of all arriving ions above 8 eV, where point defect generation is expected for hexagonal MoS<sub>2</sub>. Plasma studies were used to select optimum growth conditions for 2D MoS<sub>2</sub> synthesis on SiO<sub>2</sub> surfaces at 700 °C. Film thickness uniformity was verified by producing 2-3 monolayer layer thick hexagonal polycrystalline MoS<sub>2</sub> films over 25-50 mm scale area sizes as confirmed by in-situ Raman spectroscopy and TEM microscopy.

[1]. C. Muratore, J.J. Hu, B. Wang, M.A. Haque, J.E. Bultman, M. L. Jespersen, P.J. Shamberger, M. E. McConney, R.D. Naguy, A.A. Voevodin, "Continuous ultra-thin MoS<sub>2</sub> films grown by low-temperature physical vapor deposition", *Applied Physics Letters* 104 (2014) 261604 1-5

11:40am **PS+2D+SE-WeM12 Molybdenum Nitride Formation by N<sub>2</sub> Plasma Exposure on Molybdenum Disulfide: In-situ Surface Study.** *Angelica Azcatl, X. Qin, Q. Wang, N. Lu, M.J. Kim, C.L. Hinkle, R.M. Wallace*, The University of Texas at Dallas

Two-dimensional molybdenum disulfide (MoS<sub>2</sub>) is currently considered as a potential channel material for CMOS applications. Electron mobilities on the order of 470 cm<sup>2</sup>/Vs [1] have been reported for few-layer MoS<sub>2</sub> based FETs. Such promising results have fueled the efforts on synthesis of large area and high quality mono and few-layer MoS<sub>2</sub>. Yet, the development of MoS<sub>2</sub> processing techniques of interest for device fabrication (i.e. doping, etching, functionalization) is still in an early stage.

Recently, it has been reported that when MoS<sub>2</sub> is exposed to SF<sub>6</sub>, CF<sub>4</sub> or CHF<sub>3</sub> plasma treatments, fluorine can be introduced in the MoS<sub>2</sub> structure as an acceptor dopant, resulting in p-type doping. In parallel, due to the weak van der Waals interlayer forces, layer etching occurred as a side effect after these fluorine-based plasma exposures. [2]

Following the exploration of the effect of plasma exposures on MoS<sub>2</sub>, in this study nitrogen plasma exposures on MoS<sub>2</sub> were performed, while the surface chemistry was monitored by in-situ by X-ray Photoelectron Spectroscopy. Theoretical studies have shown that substitution of sulfur with nitrogen in MoS<sub>2</sub> leads to p-type doping. [3,4] Here, the chemical analysis obtained by XPS indicates that nitrogen will covalently interact with molybdenum to generate molybdenum nitride. It was found that the nitrogen content in MoS<sub>2</sub> can be controlled with exposure time. The thermal stability of MoN<sub>x</sub> formed due to sulfur replacement with nitrogen will be discussed. Finally, Raman Spectroscopy studies and Scanning Transmission Electrons Microscopy imaging on the MoN<sub>x</sub>/MoS<sub>2</sub> structure will be presented to discuss the impact of the Mo-N bonding environment on the MoS<sub>2</sub> structure. This study will give an important insight for the understanding of the interaction of MoS<sub>2</sub> with a non-metal dopant atom, nitrogen, which has implications on the electrical properties of MoS<sub>2</sub>.

This work is supported in part the Center for Low Energy Systems Technology (LEAST), one of six centers supported by the STARnet phase of the Focus Center Research Program (FCRP), a Semiconductor Research Corporation program sponsored by MARCO and DARPA, and by the SWAN Center, a SRC center sponsored by the Nanoelectronics Research Initiative and NIST.

#### References

[1] W. Bao, et al. *Applied Physics Letters* 102, 042104 (2013).

[2] M. Chen, et al., *Appl. Phys. Lett.* 103, 142110 (2013).

[3] H.-P. Komsa, et al., *Phys. Rev. B* 88, 035301 (2013).

[4] Q. Yue, et al., *Phys. Lett. A* 377, 1362 (2013).

12:00pm **PS+2D+SE-WeM13 Low Temperature Synthesis of AlYB<sub>14</sub> by High Power Pulsed Magnetron Sputtering.** *Oliver Hunold, Y.T. Chen, D. Music*, RWTH Aachen University, Germany, *P.O.A. Persson*, Linköping University, Sweden, *J.M. Schneider*, RWTH Aachen University, Germany

The influence of ion bombardment on the structure evolution of AlYB<sub>14</sub> was studied by using high power pulsed magnetron sputtering (HPPMS). The structure was analyzed by X-ray and electron diffraction. The diffraction data are consistent with the formation of crystalline AlYB<sub>14</sub> domains in an amorphous matrix. As the growth temperature was 675 °C synthesis was conducted at 725 °C below the bulk synthesis temperature. It is reasonable to assume that this decrease in the growth temperature is facilitated by bombardment of ions formed in the HPPMS discharge resulting in enhanced surface diffusion and hence higher adatom mobility. This work may be relevant for synthesizing other boron rich solids with low symmetry

crystal structures at temperatures well below their bulk synthesis temperature.

# Thursday Morning, October 22, 2015

## 2D Materials Focus Topic

Room: 212C - Session

2D+EM+MG+NS+SE+SM+SS+TF-ThM

## Emergent 2D Materials

Moderator: Paul Sheehan, Naval Research Laboratory

8:00am **2D+EM+MG+NS+SE+SM+SS+TF-ThM1 CVD Growth and Characterization of 2D MoS<sub>2</sub>, MoSe<sub>2</sub>, MoTe<sub>2</sub>, WS<sub>2</sub>, WSe<sub>2</sub>, and MoS<sub>2</sub>(1-x)Se<sub>2x</sub> Alloys**, David Barroso, T. Empante, A. Nguyen, V. Klee, I. Lu, E. Preciado, C. Lee, C. Huang, W. Coley, S. Naghibi, G. von Son, A. Brooks, J. Kim, L. Bartels, University of California, Riverside

Transition Metal Dichalcogenides (TMDs) have been of increasing interest over the past years due to their exciting semiconducting properties. In the bulk, TMDs possess a native indirect bandgap and transition to a direct bandgap as they approach the monolayer limit. The bandgaps range from 1.15 eV to 1.95 eV depending on composition. Using organic liquids and/or inorganic powders as precursors, CVD growth techniques have been realized for MX<sub>2</sub> TMDs (M = Mo, W; X = S, Se, Te) and their alloys at tunable compositions. We achieved consistent synthesis of these TMDs materials. The films can either be made homogeneous in bandgap or exhibiting a linear bandgap gradient. Characterization of the films include Raman and photoluminescence spectroscopy, as well as AFM. Device fabrication allows for transport measurements. Depending on the composition, the materials show n- or p-doping in a consistent fashion.

8:20am **2D+EM+MG+NS+SE+SM+SS+TF-ThM2 Investigation of Manganese Dioxide Nanosheets by STM and AFM**, Loranne Vernisse, S. Afsari, S.L. Shumlas, A.C. Thenuwara, D.R. Strongin, E. Borguet, Temple University

Interest in ultrathin two-dimensional nanosheets has grown exponentially thanks to their unique and diverse electronic properties. As they possess atomic or molecular thickness and infinite planar dimension, they are expected to have different properties than the bulk of the material from which they originate. This offers opportunities for the development of devices in various areas, ranging from catalysis to electronics. Using the exfoliation approach, it is possible to investigate 2D nanosheets of different materials in search of new phenomena and applications. Bearing this mind, we focused on manganese dioxide (MnO<sub>2</sub>), and more specifically  $\delta$ -MnO<sub>2</sub> (Birnessite). This mineral has the advantage to present a low surface enthalpy [1], which results in weak water binding. Moreover, the presence of defects, e.g., oxygen vacancies has a dopant effect on water oxidation. These properties make MnO<sub>2</sub> a perfect candidate as a catalytic surface for water splitting and pave the way to the design of clean and renewable energy system. Furthermore, MnO<sub>2</sub> can be easily exfoliated into ultrathin nanosheets owing to the layered structure of the manganese oxide precursors.

Our goal is to investigate the catalytic activity of ultrathin MnO<sub>2</sub> nanosheets using scanning probe microscopy techniques, especially atomic force microscopy (tapping mode) and scanning tunneling microscopy (ambient and electrochemical conditions). In this perspective, we have first improved the deposition processes and find the imaging conditions to observe MnO<sub>2</sub> nanosheets with an average thickness of one or two layers. We have also showed that MnO<sub>2</sub> single layer nanosheets exhibit an expected hexagonal atomic pattern and present some defects. We will now resolve and identify the different defects and investigate the evolution of the conductivity as a function of the defect concentration and the number of layers.

This work was supported as part of the Center for the Computational Design of Functional Layered Materials, an Energy Frontier Research Center funded by the U.S. Department of Energy, Office of Science, Basic Energy Sciences under Award #DE-SC0012575.

[1] M. M. Najafpour, E. Amini, M. Khatamian, R. Carpentier, S. I. Allakhverdiev, Journal of Photochemistry and Photobiology B: Biology (2014), 133, 124.

8:40am **2D+EM+MG+NS+SE+SM+SS+TF-ThM3 Two-Dimensional Early Transition Metal Carbides and Carbonitrides "MXenes": Synthesis, Properties and Applications**, Michael Naguib, Oak Ridge National Laboratory

INVITED

Ternary layered carbides and nitrides with formula of M<sub>n+1</sub>AX<sub>n</sub> (M stands for early transition metal, A for group A element, X is carbon or nitrogen, and n=1, 2, or 3), so called MAX phases, are known for their unique combinations properties of ceramics and metals. It was found recently that etching atomically thin layers of aluminum from the MAX phases results in

forming weakly bonded stacks of two-dimensional (2D) layers of early transition, coined as MXenes. The etching was carried out in fluoride contained aqueous systems. Thus MXenes surfaces are terminated with a mixture of groups including OH, O, and F. Sonicating MXenes in water results in delaminating few layers of MXenes from each other. However, to achieve a large-scale delamination, intercalation of a large compound between the layers prior to delamination is needed. MXenes were found to be a very interesting family of 2D materials since they are electrically conductors and hydrophilic. They also showed an excellent performance as electrodes for electrochemical super capacitors and Li-ion batteries. Here the recent progress in MXenes research from the synthesis to properties and applications will be covered, and in more details, large-scale delamination of MXenes will be discussed. Also, light will be shed on the performance of MXenes as electrode materials for electrochemical energy storage systems.

9:20am **2D+EM+MG+NS+SE+SM+SS+TF-ThM5 Molecular Beam Epitaxy of Large area HfSe<sub>2</sub>(ZrSe<sub>2</sub>)/MoSe<sub>2</sub> van der Waals Heterostructures on AlN(0001)/Si substrates**, Athanasios Dimoulas, P. Tsipas, E. Xenogiannopoulou, D. Tsoutsou, K.E. Aretouli, J. Marquez-Velasco, S.A. Giamini, N. Kelaidis, NCSR DEMOKRITOS, Greece

Two dimensional (2D) semiconductor van der Waals heterostructures (HS) made of group IVB (Zr, Hf) and group VIB (Mo, W) metal dichalcogenides are predicted [1] to have type II or type III band alignments mainly because of a large difference in their workfunctions and band gaps, which makes them candidates for novel 2D staggered, or broken gap tunneling field effect transistors (TFET). We use molecular beam epitaxy (MBE) to grow high quality large area HfSe<sub>2</sub> [2,3], ZrSe<sub>2</sub> [4] and MoSe<sub>2</sub> [5] films directly on AlN(0001)/Si(111) substrates. We confirm by RHEED and HRTEM that atomically thin layers (1-6 ML) are grown in single crystal form with a well-defined in-plane orientation on AlN. The films are continuous with smooth surface morphology (0.6 nm RMS roughness) and abrupt interfaces with no detectable reaction as verified by in-situ XPS and HRTEM. Micro Raman mapping for all layers confirms their structural integrity down to one monolayer and reveals very good uniformity on a cm-scale wafer and excellent stability of MoSe<sub>2</sub> over a period of at least two weeks in air. Strong room temperature PL signal of 1 ML MoSe<sub>2</sub> indicate high quality direct gap semiconductor in agreement with valence band structure details imaged by our in-situ ARPES [3, 5]. In a second step, MoSe<sub>2</sub>/HfSe<sub>2</sub> [3] and MoSe<sub>2</sub>/ZrSe<sub>2</sub> [4] HS were grown. Despite the large lattice mismatch, all layers are grown epitaxially as evidenced by RHEED with no detectable defects at the interfaces as confirmed by HRTEM suggesting good quality vdW epitaxy [6]. Using UPS the workfunctions (WF) were estimated to be 5.2, 5.5 and 5.4 eV for MoSe<sub>2</sub>, HfSe<sub>2</sub> and ZrSe<sub>2</sub> respectively [3,4]. The last two differ substantially from theoretical values (~ 6 eV). Based on our STM and DFT calculations [3], we conclude that this difference is due to an ordered Se adlayer which lowers the HfSe<sub>2</sub> and ZrSe<sub>2</sub> WF bridging the WF gap between them and MoSe<sub>2</sub>. As a result, small valence band offsets of 0.13 and 0.58 eV were found for the HfSe<sub>2</sub>/MoSe<sub>2</sub> and ZrSe<sub>2</sub>/MoSe<sub>2</sub> HS, respectively leading to type II band alignments. The availability of low cost wide-gap-AlN/Si wafers in 300 mm wafer sizes defines a manufacturable route for single crystal 2D semiconductor technology.

We acknowledge financial support from ERC Advanced Grant SMARTGATE-291260. We thank IMEC for providing the AlN/Si substrates.

[1] C. Gong et al., *APL*, **103**, 053513 (2013)

[2] R. Yue et al., *ACS Nano*, **9**, 474 (2014)

[3] K. E. Aretouli et al., *APL*, **106**, 143105 (2015)

[4] P. Tsipas et al., *Microelectron. Eng.* (2015), <http://dx.doi.org/10.1016/j.mee.2015.04.113>

[5] E. Xenogiannopoulou et al, *Nanoscale* **7**, 7896 (2015)

[6] F.S. Ohuchi et al., *JAP*, **68**, 2168 (1990)

9:40am **2D+EM+MG+NS+SE+SM+SS+TF-ThM6 Surface Investigation of WSe<sub>2</sub> Atomically Thin Film and Bulk Crystal Surfaces**, Rafik Addou, H. Zhu, University of Texas at Dallas, Y.-C. Lin, S.M. Eichfeld, J.A. Robinson, Penn State University, R.M. Wallace, University of Texas at Dallas

Heterogeneous fabrication of semiconducting two-dimensional layered materials presents a promising opportunity to develop highly tunable electronic and optoelectronic materials. (1-2) An example of crystalline monolayer of WSe<sub>2</sub> grown by chemical vapor deposition on epitaxial graphene (EG) grown from silicon carbide had been investigated at nanoscale level. The WSe<sub>2</sub> surface was characterized using atomic force microscopy (AFM) scanning tunneling microscopy/spectroscopy (STM/STS) and X-ray photoelectron spectroscopy (XPS). (3,4) AFM and



large STM images show high-quality WSe<sub>2</sub> monolayers. The sharpness of the W 4f and Se 3d core levels confirms the absence of any measurable reaction at the interface and oxide formation. The photoemission measurements of WSe<sub>2</sub>-Graphene interface suggest p-type doping due to charge transfer (EG withdraws electrons from WSe<sub>2</sub>) at the interface and formation of Schottky-type contact,(5) suggesting possible applications of such heterostructures as diodes and photodetectors. High-resolution STM images reveal atomic-size imperfections induced by Se vacancies and impurities. Additionally, the investigation of bulk WSe<sub>2</sub>(0001) surface shows spatial variation attributed to the presence of two components in W 4f<sub>7/2</sub> core level attributed to the presence of both n- and p-type behavior. STM images exhibit also various types of defect induced by vacancies and dopants. The STS spectra reveal two main characteristics i) expected p-type conductivity where the Fermi level located at the valence band edge, and ii) zero conductivity at negative bias explained by defect-induced band bending as reported on geological MoS<sub>2</sub> crystal surfaces.(4) In conclusion, the spatial variation (topography and electronic structure) is more noticeable in bulk WSe<sub>2</sub> grown by chemical vapor transport than in CVD thin films.

This work was supported in part by the Southwest Academy on Nanoelectronics sponsored by the Nanoelectronic Research Initiative and NIST and the Center for Low Energy Systems Technology, one of six centers supported by the STARnet phase of the Focus Center Research Program, a Semiconductor Research Corporation program sponsored by MARCO and DARPA.

- (1) Yu-Chuan Lin et al., Nano Lett., **14** (2014) 6936-6941.
- (2) Yu-Chuan Lin et al., Nature Comm. arXiv:1503.05592v1.
- (3) Robert M. Wallace, ECS Trans. **64** (2014) 109-116.
- (4) Rafik Addou, Luigi Colombo, and Robert M. Wallace, ACS Appl. Mater. Interfaces (Accepted, 2015).
- (5) Horacio Coy Diaz, Rafik Addou, and Matthias Batzill, Nanosclae **6** (2014) 1071-1078.

11:00am **2D+EM+MG+NS+SE+SM+SS+TF-ThM10 A Kinetic Study on the Adsorption of Polar (Water) and Non-Polar (Benzene) Molecules on CVD Graphene, Nilushni Sivapragasam, U. Burghaus, North Dakota State University**

The adsorption kinetics of water and benzene at ultrahigh vacuum conditions were studied. Two different chemical vapor deposited graphene samples (graphene/SiO<sub>2</sub> and graphene/Cu) were utilized. Different surface analytical techniques (Auger electron spectroscopy, X-ray photoelectron spectroscopy, and Raman spectroscopy) were used to characterize the surface. Subsequently, a kinetics study - to understand the adsorption of water and benzene- using thermal desorption spectroscopy (TDS) was conducted. The TDS results revealed the hydrophobicity of water on graphene. However, the adsorption kinetics of water on graphene did not mimic the bare substrate, i.e., graphene is non-transparent for water adsorption. In contrast, graphene was transparent for benzene adsorption. Furthermore, the adsorption kinetics of both, water and benzene were substrate dependent.

11:20am **2D+EM+MG+NS+SE+SM+SS+TF-ThM11 Epitaxial Ultrathin MoSe<sub>2</sub> Layers Grown by Molecular Beam Epitaxy, Ming-Wei Chen, M.B. Whitwick, O. Lopez-Sanchez, D. Dumcenco, A. Kis, Ecole Polytechnique Fédérale de Lausanne (EPFL), Switzerland**

Two-dimensional transition metal dichalcogenides (TMDs) have attracted widespread attention recently, and the focus is specifically on ultrathin layers due to the strong spin-orbit coupling and direct band-gap transition of single-layers. The unique properties of various TMDs also enable the possibilities for future optoelectronic applications. However, the synthesis of TMDs with uniform large-area and high-quality still remains challenging. While chemical vapour deposition has been demonstrated as a promising technique, the complexity of chemical precursors and the lacking of *in-situ* observation technique strongly hinder the progress.

Here, We propose to use ultra-high vacuum molecular beam epitaxy (MBE) to grow MoSe<sub>2</sub> ultrathin layers, down to single-layer in a controllable way. Epitaxial MoSe<sub>2</sub> layers were successfully grown on different crystalline substrates via van der Waals epitaxy mechanism, benefited from the weak interlayer interaction and the lacking of dangling bonds. Reflection high energy electron diffraction (RHEED) was used to *in-situ* monitor the initial growth stage and revealed a clear transition of the streaks, demonstrating the formation of MoSe<sub>2</sub> layer. Sharp streaks were obtained in the growth end, with the streak spacing corresponding to MoSe<sub>2</sub> lattice constant, and no significant strain effect was observed. In order to demonstrate the validity of van der Waals epitaxy, different crystalline substrates with lattice mismatch up to 30 % have been tested. The epitaxial layers showed a smooth and uniform surface in atomic force microscopy, and the quality was further confirmed in Raman spectrum and transmission electron

microscopy. Furthermore, photoluminescence of the single-layer MoSe<sub>2</sub> showing a sharp peak of ~1.58 eV at room temperature demonstrates the direct band-gap feature and indicates the potentials of photovoltaic applications. In the end, the growth of two-dimensional van der Waals heterostructures has also been addressed and the results pave way for heterostructure studies.

In summary, molecular beam epitaxy has been proved to be a reliable route to grow large-area and high-crystalline transition metal chalcogenides, and is promising to facilitate the integration of other two-dimensional materials in the future.

11:40am **2D+EM+MG+NS+SE+SM+SS+TF-ThM12 A Two-Dimensional Oxide Quasicrystal, Stefan Förster, Institute of Physics, Martin-Luther-Universität Halle-Wittenberg, Germany, J.I. Flege, Institute of Physics, University of Bremen, Germany, K. Meinel, R. Hammer, M. Trautmann, Institute of Physics, Martin-Luther-Universität Halle-Wittenberg, Germany, J. Falta, Institute of Solid State Physics, University of Bremen, Germany, T. Greber, Physik-Institut, University of Zürich, Switzerland, W. Widdra, Institute of Physics, Martin-Luther-Universität Halle-Wittenberg, Germany**

**INVITED**

With the recent discovery of the first oxide quasicrystal (QC) aperiodicity is entering the field of two-dimensional materials [1]. Aperiodicity means that the system exhibits long-range order as expressed by sharp diffraction spots but since the ordering follows an aperiodic function the system is lacking translational symmetry. We report here on the complex growth process of the oxide QC involving a high-temperature wetting process and periodic approximant structures.

The QC is derived from BaTiO<sub>3</sub> thin films on a hexagonal Pt(111) substrate and exhibits a sharp twelve-fold diffraction pattern [1]. Based on scanning tunneling microscopy the aperiodic atomic structure had been resolved [1]. It is formed by surface atoms arranged in forms of squares, triangles, and rhombi with a next-neighbour distance of 0.69 nm. In addition to this dodecagonal atomic arrangement, building blocks of squares, triangles, and rhombi are also found on  $(2+\sqrt{3})$  and  $(2+\sqrt{3})^2$  larger scales indicating the characteristic self-similarity of an ordered QC [1]. The high-resolution STM measurements allow furthermore to identify atomic flips in the structure indicating lattice excitations in the quasicrystal called phasons. Using low-energy electron microscopy (LEEM) the preparation and the growth of the QC films on top of the hexagonal Pt(111) is monitored in all details from room temperature up to about 1200 K. LEEM shows that upon high-temperature annealing large 3DBaTiO<sub>3</sub> islands are formed with bare Pt(111)-(1x1) in between. At temperatures above 1020 K a wetting layer spreads on the free Pt area. This wetting process can be reversed by annealing in an oxygen atmosphere. In-situ LEEM measurements show that under these conditions the QC decays into small BaTiO<sub>3</sub> islands. The observed interface-driven formation of a 2D QC from a perovskite oxide in contact with a hexagonal substrate is expected to be a general phenomenon.

1. S. Förster, K. Meinel, R. Hammer, M. Trautmann, and W. Widdra, *Nature* **502**, (2013) 215.

# Thursday Afternoon, October 22, 2015

## Plasma Science and Technology

Room: 210B - Session PS+AP+SE-ThA

### Advanced Ion Implantation and Plasma Doping

Moderator: Aseem K. Srivastava, Applied Materials, Inc.

2:20pm **PS+AP+SE-ThA1 Evolutionary Trends in Ion Implantation**,  
**Anthony Renau**, Applied Materials, Varian Semiconductor Equipment  
**INVITED**

Since the 1960s and 1970s ion implantation has been used for the p- and n-type doping of semiconductors. The ability of ion implantation to abruptly alter the stoichiometry of the substrate has made it a very attractive technology for making transistors with the required drive characteristics, by accurately manipulating dopant concentrations in the contact and channel regions. It is used to control carrier density, channel length, contact resistance, isolation and other key device attributes.

There have been significant enhancements to enable ion implant to continue to meet semiconductor doping needs. These include the development of ribbon ion beams, substrate temperature control, accurate beam angle control and novel methods for precisely varying the dose over the substrate. These improvements have also enabled the technology to be used for a rapidly growing number of non-doping applications.

Today, the majority of implants are done not for doping, but are instead used for some form of materials modification or engineering. These include, for example, strain control, pre- or post-treatments to improve some other process step, and lattice engineering for isolation or diffusion control.

In this paper we will discuss some of the improvements to the technology and the applications that have benefited from these. We will also describe how directed ribbon beam technology, similar to that used for implanters, can also be used to improve materials engineering applications as diverse as etch and CMP.

3:00pm **PS+AP+SE-ThA3 Conformal Arsenic Doping using a Radial Line Slot Antenna Microwave Plasma Source**, **Hirokazu Ueda**, Tokyo Electron Limited, Japan, **P. Ventzek**, Tokyo Electron America, Inc., **M. Oka**, **Y. Kobayashi**, **Y. Sugimoto**, Tokyo Electron Ltd., **T. Nozawa**, Tokyo Electron Ltd., Japan, **S. Kawakami**, Tokyo Electron Ltd.  
**INVITED**

Doping and activation of non-planar topographic structures is important for the fabrication of functional FinFET and nanowire based devices to name a few. Conformal plasma arsenic doping of topographic (fin) structures was achieved using RLSA™ microwave plasmas with low temperature annealing. To show that the arsenic concentrations were identical at the fin top and sides, dopant concentrations were measured precisely by TEM and SEM EDX for both plasma doping and subsequent annealing steps. We found that doping using plasmas generated by lower RF bias operation coincident with high microwave power was key to obtaining perfectly conformal arsenic dose/profiles after annealing. The RLSA™ microwave plasma facilitates high enough electron density at the plasma generation region to supply enough reactive dopants for sufficient dose. The high plasma density plasma allows for operation in a low RF power and high process pressure regime. This regime yields ions with sufficient flux and energy for dopant integration into and redistribution around the topographic structure. At the same time low enough energy ions can be controllably accessed to ensure fin damage is eliminated. We also demonstrate optimized rf bias power of the microwave RLSA™ plasma enables additional control of dopant conformality post SPM wet cleaning step. The wet clean poses a significant challenge for dose retention as cleans tend to remove oxidized or otherwise disordered silicon material. The source of dose retention is shown to be related to dopant transport through a ternary (As-Si-O) oxide layer, segregation effects and the stable nature of the oxide. The presentation will include experimental and computational results related to dose conformality and retention. Comments related to the future of plasma doping technology including advanced materials, metrology and control will round out the presentation.

4:00pm **PS+AP+SE-ThA6 Practical Application of Atom Probe to Analysis of Ion Implantation**, **Ty Prosa**, CAMECA Instruments Inc.  
**INVITED**

Characterization of implanted dopants and impurity atoms within individual silicon nano-devices is critical to the semiconductor industry. While secondary ion mass spectrometry (SIMS) depth profiles achieve a high level of quantification with ion implanted standards in various matrices, atom probe tomography (APT) offers a unique combination of high analytical sensitivity coupled with high spatial resolution [1]. SIMS achieves its

sensitivity by analyzing relatively unconstrained sample volumes, analyzed areas often greater than several hundred square microns. Square microns of material cannot be analyzed by APT and so it can never compete with SIMS for sensitivity at the micron scale; however, the situation is very different at the nanoscale—the regime of individual device volumes. Within this regime APT has high, uniform, quantitative chemical sensitivity with sub-nanometer spatial sensitivity.

Understanding the precision and accuracy of APT when applied to ion implanted dopant profiles is essential for general adoption by the semiconductor industry. Three-dimensional atom positions are determined using a simple point-projection methodology [2]. Adopting best practices within the constraints of this methodology is necessary to allow uniform and unbiased determination of atom positions and depth profiles. Although the ultimate sensitivity of APT is determined by counting statistics, it is well known that counting statistics alone do not fully account for accuracy limitations. The free parameters available within the reconstruction process are often dominant in terms of total observed error.

During this presentation, a number of examples will be shown of APT applied to the analysis of dopant distributions in relevant structures. The focus will be ion implanted structures with discussion of best practice approaches to minimize error and remove bias by the practitioner. Material structures include a series of NIST Standard Reference Material implants into silicon [3] and additional implants into GaN-based materials.

[1] T.F. Kelly and D.J. Larson, *Annual Reviews of Materials Research* 42 (2012) 1.

[2] P. Bas et al., *Surf. Sci.* 87/88 (1995) 298.

[3] R.R. Greenberg et al., *Radioanal. Nucl. Chem.* 245 (2000) 57.

4:40pm **PS+AP+SE-ThA8 Optical Emission Spectroscopy to Determine Plasma Parameters in an Oxygen Inductively Coupled Plasma**, **Nathaniel Ly**, **J. Boffard**, **C.C. Lin**, **A.E. Wendt**, University of Wisconsin - Madison, **S. Radovanov**, **H. Persing**, **A. Likhanskii**, Applied Materials, Inc.

The success of ion implantation to precisely modify substrate properties requires control of the incident ion energies to achieve the desired depth of the implanted ions. Oxygen plasmas generally contain both  $O^+$  and  $O_2^+$  positive ions, and in plasma immersion ion implantation (PIII) of oxygen, the two will produce different concentration depth profiles due to their different energy/mass ratios. Predicting the overall profile thus requires knowledge of the relative fluxes of the two ion species. Motivated by the long term goal of a robust predictive model, here we combine experiment and numerical simulation to investigate the feasibility of using non-invasive optical emission spectroscopy (OES) to monitor plasma parameters in an oxygen inductively-coupled plasma. Initial experiments made use of a small admixture of argon with the oxygen to take advantage of established techniques involving argon OES. In addition to recording argon emissions, measurements of multiple  $O$ ,  $O_2$ ,  $O^+$ , and  $O_2^+$  emission intensities were made as a function of pressure (1-30 mTorr) and power (500-2000 W). An emission model makes use of available electron impact excitation cross sections for argon and atomic and molecular oxygen to relate measured emission spectra to corresponding plasma parameters, including electron temperature and the dissociation fraction of the neutral oxygen. Data taken while as a function of the percentage of argon in the Ar/O<sub>2</sub> mixture showed that even a very small admixture of argon significantly affected the oxygen plasma properties, and more recent experiments have thus focused on oxygen OES in a pure oxygen plasma. The CRTRS 2D/3D plasma code self-consistently and semi-implicitly solves for ICP power deposition and uses Poisson's equation to solve for the electrostatic potential and dynamics of electrons and ions in the drift-diffusion approximation (or full momentum equations). The code also solves for the electron temperature, and generation and quenching of excited states as well as their dynamics. The experimental results are used in combination with simulation predictions to understand the dependence of plasma parameters, including the relative fluxes of  $O^+$  and  $O_2^+$ , on the operating parameters.

The authors acknowledge support from NSF grant PHY-1068670.

5:00pm **PS+AP+SE-ThA9 Adhesion Improvement of Carbon Nitride Coatings on Steel Surfaces by Metal Ion Implantation using HiPIMS**, **Konstantinos Bakoglidis**, **G. Greczynski**, **S. Schmidt**, **L. Hultman**, Linköping University, Sweden

Carbon based thin films are materials with low friction and wear resistance. Deposition of C based thin films as coatings on steel substrates can enhance the tribological performance of steel surfaces. Adhesion of magnetron sputtered C based coatings on steel substrates is, however, often

insufficient, leading to film delamination or flaking after the deposition. Adhesion is essential when such films are exploited in tribological applications and can be improved by using ion etching of the steel surface prior to film deposition. Several ion etching techniques are used, among them metal ion etching, for ion implantation in order to prepare the steel surface for the C film deposition. Moreover, high power impulse magnetron sputtering (HiPIMS) offers high metal ionization conditions and effectively enhances ion implantation into the steel subsurface. In this study, we used four different metal targets, namely Al, Cr, Zr, W, in HiPIMS mode in Ar-based plasma with a pressure of 200 mPa, and under a negative applied bias voltage of 900 V, which was synchronized with the cathode pulse. All targets were operated with an energy per pulse of 15 J, with pulse width of 200  $\mu$ s, an etching time of 30 s, while the frequency was set at 100 Hz. A carbon nitride (CN<sub>x</sub>) thin film was deposited after each etching step, using a graphite target in DC mode, operated at 1400 W, in a N<sub>2</sub>/Ar gas mixture with a ratio of 0.16, and at a temperature of 150 °C, while the pressure was kept constant at 400 mPa. In all cases except Zr, a thin metal interlayer was obtained, with thicknesses < 20 nm, while adhesion of CN<sub>x</sub> films on steel surface was dramatically improved when W ions were used for the pre-treatment phase.

# Friday Morning, October 23, 2015

**Plasma Science and Technology**  
**Room: 210A - Session PS+SE-FrM**

**Atmospheric Pressure Plasma Processing II**  
**Moderator: Souvik Ghosh, Case Western Reserve University**

9:00am **PS+SE-FrM3 Scaling Atmospheric Pressure Plasma Sources for Manufacturing-Scale Applications, Steven Shannon, North Carolina State University** **INVITED**

Material processing using plasmas at atmospheric pressure presents one of the great areas of future growth for the Plasma Science and Technology Division of the AVS. Extension of plasma processing to atmospheric pressures (and ironically eliminating the need for "vacuum") provides two key advantages in processing. The first is the reduced cost and increased throughput that could be realized in equipment that does not require high vacuum design, load locks, etc. The second, and more significant, are the new applications that plasma science can now contribute to including water treatment, soft materials processing, processing of non-vacuum-friendly materials, and medicine.

Atmospheric plasma systems for manufacturing have the same high volume integration challenges that low pressure plasma systems do. These are scalability and throughput. These systems need to be able to process large areas (or volumes, depending on the application). This throughput scaling presents a challenge especially when some level of homogeneity in process both within a sample and from sample to sample are required. Maintaining this process uniformity over a large area is further complicated by the need to maintain a high rate of reactive specie production, especially when the standard solution of "turn up the power" results in typically undesirable instability and heating in these higher pressure discharges.

At NCSU, researchers have developed an atmospheric plasma source that seeks to address these scale-up concerns of size and reactant production. This coaxially driven source can be driven in the VHF range of frequencies (60MHz - 200MHz, with 162MHz used in the work shown here) with a plurality of feed gases not requiring noble gas dilution. The VHF heating combined with source circuit design produce a volume glow with power densities ranging from 1W/cm<sup>2</sup> to 20W/cm<sup>2</sup>. The unique source design enables operation of an RF driven / DC grounded electrode that enables delivery of gas and liquid precursors through the electrode surface. This enables the introduction of liquid precursors into the active plasma region while maintaining a stable volume glow. Multiple sources can be run in parallel for larger volume operation, and scalability has been demonstrated. Reactive specie production has been quantified for air plasmas and water plasmas (with water delivery from the powered electrode). The water electrode configuration yields OH concentrations over 10<sup>15</sup>/cm<sup>3</sup> in the active plasma region.

This work is supported by the NSF I/UCRC program through the Center for Lasers and Plasmas in Advanced Manufacturing, the NCSU Chancellor's Innovation Fund, and Advanced Energy Inc.

9:40am **PS+SE-FrM5 Improving of Harvest Period and Crop Yield of Arabidopsis Thaliana L. using Nonthermal Atmospheric Air Plasma, Kazunori Koga, T. Sarinont, T. Amano, H. Seo, N. Itagaki, M. Shiratani, Kyushu University, Japan**

Nonthermal atmospheric plasmas have been widely used for biomedical applications [1-3]. Growth enhancement of plants is one of the important applications of such plasmas. Here we have studied effects of atmospheric air plasma irradiation to seeds of *Arabidopsis thaliana L.* on the harvest period and crop yield. Experiments were carried out using a scalable DBD device [2, 3]. The device consisted of 20 electrodes of a stainless rod of 1 mm in outer diameter and 60 mm in length covered with a ceramic tube of 2 mm in outer diameter. The discharge voltage and current were 9.2 kV and 0.2 A. 20 seeds of *Arabidopsis thaliana L.* were set 3 mm below the electrodes. After 3 minutes plasma irradiation, they were grown on rockwool until the harvest stage. The harvest period is defined as time from the beginning of cultivation to the first seed production. To evaluate the growth enhancement ability of the plasma irradiation, the area of two primary leaves of eight plants, namely 16 leaves, was measured every three days. The whole experiment was repeated 3 times with similar results. Data were analyzed by two-way analysis of variance. The harvest period without and with plasma irradiation are 71.31±5.63 and 66.53±3.82 days. The seed weight without and with plasma irradiation are 0.0201±0.0024,

0.0225±0.0016 mg/seed. The leaf area after 28 days from the beginning of cultivation without and with plasma irradiation are 0.049±0.011 cm<sup>2</sup> and 0.064±0.014 cm<sup>2</sup>. These measured values without and with plasma irradiation are statistically significance different at  $\alpha=0.05$  ( $P<0.05$ ). Plasma irradiation brings about 7% shorter harvest period, 12% higher seed weights and 30% larger primary leaves, compared to those without plasma irradiation. Thus, plasma irradiation to seeds is a cost effective and environmental friendly method for improving of harvest period and crop yield of plants. The growth enhancement mechanism will be discussed in the presentation.

[1] J. Raiser and M. Zenker, J. Phys. D, **39**, 3520 (2006).

[2] T. Sarinont, et al., JPS Conf. Proc. **1**, 015078 (2014).

[3] S. Kitazaki, et al., Curr. Appl. Phys., **14**, S149 (2014).

10:00am **PS+SE-FrM6 Numerical Modelling of Atmospheric Pulsed Streamers over Water; Electrodynamics at the Interface, Alex Lindsay, S. Shannon, North Carolina State University, D.B. Graves, University of California at Berkeley**

There is significant interest in characterizing interactions between atmospheric plasmas and water for applications in medicine, water decontamination, distributed farming, etc. In one particular example members of the community are investigating replacement of invasive electroporation for drug delivery and gene therapy with low-power atmospheric plasma devices. Although the mechanism by which electric fields create conductive pathways for drug delivery into cells is generally known, the mechanism by which plasmas create those liquid-phase electric fields is an active area of research. Pioneering work in [1] has done much to advance our understanding, but more work remains. We wish to present modeling tools that are open to the community in the hope that this will enhance development of the tools, scrutiny and reproducibility of numerical results, and the pace at which plasma-liquid research is conducted. By developing open community tools, we hope to reduce the time-waste that comes from different groups re-inventing the wheel to study similar phenomena. With those motivations, we consider both finite-volume and finite-element discretizations of the Poisson and continuity equations governing electrodynamics in the gas and liquid phases. For a first pass, a local-field approximation is used to study streamer propagation in a point-to-plane configuration with water serving as the planar electrode. Different methods for stabilization (e.g. inconsistent vs. consistent, streamline and/or crosswind) as well as markers for mesh adaption (potential, electron density curvatures) are considered.

[1] Babaeva et al. J. Phys. D: Appl. Phys. **47** (2014) 235201

10:20am **PS+SE-FrM7 Application of Atmospheric Pressure Plasma treatment on Carbon Fiber Reinforced Plastics for Adhesive Bonding, Timo Hofmann, J. Schäfer, Bundeswehr Research Institute for Material, Fuels and Lubricants, Germany, T. Löbel, German Aerospace Center (DLR), T. Meer, Airbus Group Innovations, J. Rehbein, J. Holtmannspötter, Bundeswehr Research Institute for Material, Fuels and Lubricants, Germany**

The demand for environmentally friendly means of transportation has led to a strong increase in the use of carbon fiber reinforced plastics (CFRPs). Joining of CFRP structures is currently performed using rivets and bolts. In order to exploit further weight-saving potential, the usage of adhesive bonding is investigated.

An important key factor for the success of adhesive bonding is the surface pre-treatment of the adherents. In this contribution, CFRP surfaces were treated using Atmospheric pressure plasma jet (APPJ) as a method to clean the samples and to improve adhesion by creating surface functional groups.

We present a detailed investigation of the surface morphology and the composition of CFRPs before and after treatment with APPJ. The CFRP surfaces were examined using a combination of Field-Emission Scanning Electron Microscopy (FE-SEM), Atomic Force Microscopy (AFM), Energy-Dispersive X-ray spectroscopy (EDX), and X-Ray Photoelectron Spectroscopy (XPS). Destructive tests were carried out to determine the adhesive strength and the failure mode as a function of APPJ.

We demonstrate that APPJ-processes can be used to form structural and long term stable bonds. Our results show that through the combination of analytical techniques and destructive tests it is possible to develop an understanding of the processes at the surface and to optimize the plasma treatment process.

10:40am **PS+SE-FrM8 Atmospheric Plasma Deposition of Transparent Organosilicate Multifunctional Coatings on Plastics in Air, Siming Dong, Z. Zhao, R.H. Dauskardt**, Stanford University

Atmospheric plasma deposition is a versatile coating process that enables deposition on large and/or complex shapes in air. The low temperature plasma and solvent free process allows deposition on, and simultaneous functionalization of plastic substrates in a single step. Building on our previous studies, we demonstrate a highly efficient deposition method using two precursors, an inorganic tetraethoxysilane (TEOS) and an organic 1, 5-cyclooctadiene (CYC), to deposit multi-layer organosilicate transparent coatings on poly methyl methacrylate (PMMA) and silicon (Si) substrates with atmospheric plasma deposition in air. The coatings deposition rate, transparency, chemical composition and adhesion with the PMMA substrate were investigated. Using only the TEOS precursor, high density and elastic modulus coatings were deposited on PMMA but with poor adhesion. The addition of the organic CYC precursor allowed controlled incorporation of organic components into the coating molecular network which significantly improved adhesion. The deposition rate increased from ~65 nm/min for the single precursor to ~130 nm/min for the two precursor process. The coatings exhibited ~100% transmittance in the visible wavelength range. FTIR and Raman spectroscopy of the coatings showed that the organic component (-C-C-)n in the coatings can be incorporated to form an organosilicate molecular network. This incorporation increased the coating deposition rate and also resulted in mechanical plasticity in the coatings. The adhesion of coatings with PMMA increased from ~2 J/m<sup>2</sup> to ~10 J/m<sup>2</sup> and the Young's modulus ranged from 22GPa to 34GPa. Coatings structures including composition and coating thickness to achieve optimized hardness and adhesive properties are reported.

11:00am **PS+SE-FrM9 Atmospheric Plasma Deposition of Anti-Reflection Coatings on Silicon in Open Air, Michael Hovish, R.H. Dauskardt**, Stanford University

For many modern energy and sensing applications, multilayer optical coatings are an effective way to dramatically improve light collection. Traditionally, such multilayer coatings are deposited on hard substrates using vacuum depositions. Furthermore, traditional vacuum techniques are not easily scalable, due to high costs and poor integration into the manufacturing scheme. Atmospheric plasma deposition has received attention in materials processing due to the ability to deposit functional coatings at room temperature and in open air. Room temperature operation allows for a dynamic range of substrates, both organic and inorganic. In addition to these qualities, atmospheric plasma deposition is a solvent free technique, making it a competitive alternative to sol-gel methods. In our research program, we have successfully shown several material systems which are amenable to atmospheric plasma deposition, including multifunctional organosilicate and metal oxide films. In particular, the solvent-free deposition of metal oxide films at atmospheric pressure and near room temperature provides an attractive platform for the design and fabrication of optical coatings.

We have employed atmospheric plasma to deposit thin, anti-reflection coatings on silicon. Both TaO<sub>x</sub> and TiO<sub>x</sub> films were investigated as candidates for single layer anti-reflection coatings. Films were optimized for low reflection within the visible wavelengths of light. High purity helium gas was used to transport either tantalum ethoxide or titanium ethoxide vapor into the afterglow of a helium-nitrogen plasma. A high temperature precursor delivery system was used to prevent the condensation of precursor vapors en route to the afterglow. Within the afterglow, the metal-organic compounds undergo molecular fragmentation and redistribution onto the substrate. Deposition rates, chemical compositions, optical properties, and adhesion energies to the substrate were investigated as a function of plasma power and gas composition. Spectral reflectance at 10° from normal was measured to determine the anti-reflection properties of the coatings. Atmospheric plasma deposited films on silicon show excellent anti-reflection properties, with less than 3% reflection loss near 550 nm.

11:20am **PS+SE-FrM10 Polymer Thin Film Deposition using Atmospheric Pressure Single Plasma Jet or Plasma Jet Array from a Plasma Gun Device, Céline Vivien, IEMN CNRS/Université Lille 1, France, E. Robert, J.-M. Povesle, GREMI CNRS/Université d'Orléans, France**

Plasma Enhanced Chemical Vapour Deposition (PECVD) processes have been used for decades for surface processing in a wide range of industrial applications like semiconductor films, low-k films, barrier diffusion. Thin film deposition is especially of high interest for biomedical applications for the production of protective coatings, adhesion layers, hydrophilic or hydrophobic layers. Up to now, most of used processes are usually realized under low pressure. Actually, there is a great and increasing interest in the development of plasma sources operating at atmospheric pressure. The present work deals with plasma polymerisation of TMDSO and HMDSO with a Dielectric Barrier Discharge plasma jet at atmospheric pressure, the

Plasma Gun developed in GREMI. Depending on parameters like voltage, frequency, carrier gas and monomer injection, the deposited polymer appears either as a gel-like coating or a transparent film with fringes. Deposits are characterized by Fourier Transformed IR spectroscopy and contact angle measurements. The precursor used was introduced in both liquid or gaseous state, in case TMDSO and only gaseous state in case of HMDSO. The liquid flow rate was regulated by a peristaltic pump (Ismatec) while the vapour flow was ensured by bubbling nitrogen or oxygen with a fixed flow rate of 10 sccm. Microscope slides and polished Silicon wafer (100) were used as substrates. The polymerized coatings have been obtained at frequencies between 500Hz and 4 kHz, for applied voltages between 14 and 20 kV and exposure times from 1 to 10 minutes. The deposition were realized with plasma tube edge-to-substrate distances ranging from 3 to 12 mm. Profilometer measurements revealed thicknesses comprised between 500 nm and 1.5 µm at the middle of the deposit. Deposited films analyses clearly show the efficiency of this atmospheric plasma-type TMDSO and HMDSO polymerisation and their similarity with those usually realized under low pressure RPECVD. The most interesting deposited films are obtained when the monomer is introduced under gaseous state, the samples clearly showing a better homogeneity. The influence of the transport gas is not evidenced. More experiments and analyses need to be achieved to complete these preliminary results. It must be stressed that multi-spot deposition has been obtained from plasma multi-jet delivered by a single Plasma Gun.

11:40am **PS+SE-FrM11 XPS to Investigating Spatial and Temporal Modification of Polymeric Platforms for Micro-Fluidic Devices, Marshal Dhayal, CSIR Centre for Cellular and Molecular Biology (CCMB), India**

Spatial and temporal changes in surface chemical composition silicon (Si), carbon (C) and oxygen (O) of polydimethyl siloxane surfaces before and after plasma treatment were estimated from quantitative elemental analysis of X-ray photoelectron spectroscopy (XPS) wide scan spectra. Theoretical ratio of Si/C/O in repeating unit (-[Si-(CH<sub>3</sub>)-O]<sub>n</sub>-) of polydimethyl siloxane were calculated and were compared to experimentally obtained ratio for Si/C/O obtained from untreated and plasma treated surfaces used for micro-fluidic devices. The contact angle measurements have shown that surfaces treated by air plasma can recover up to about 50% of its hydrophobic nature in less than 30 min of air exposure. These plasma modified surfaces were functionalized with poly(ethylene glycol) (PEG) silane to obtain polydimethyl siloxane surface as hydrophilic in nature for micro fluidic application. The surface chemistry of PEG-functionalized polydimethyl siloxane substrate has been studied using XPS. These different types of surfaces were used fabricate micro-fluidic devices and effects of surface nature of micro channels on fluid velocity were observed in PEG grafted micro channel in polydimethyl siloxane base micro fluidic devices. The effect of different pH of the fluids on the fluid velocity in polydimethyl siloxane -based micro channel was also studied.

# Authors Index

**Bold page numbers indicate the presenter**

## — A —

Abbas, A.: EN+AS+EM+NS+SE+SS+TF-MoM10, 2  
Abel, A.J.: EN+AS+EM+SE+SS-TuM5, **10**  
Abudayyeh, O.K.: SE+EM+EN-MoA4, **9**  
Addou, R.:  
2D+EM+MG+NS+SE+SM+SS+TF-ThM6, **22**  
Afsari, S.:  
2D+EM+MG+NS+SE+SM+SS+TF-ThM2, 22  
Ager, J.W.: EN+AS+EM+SE+SS-TuM10, **11**  
Ahlgren, M.: SE+PS-TuA7, 16  
Alarcon Llado, E.: EN+AS+EM+SE+SS-TuM2, 10  
Al-Bataineh, S.: SE+PS+SM-TuM2, **12**  
Aldridge, T.V.: EN+EM+NS+SE+SS+TF-TuA9, 14  
Allain, J.P.: SE-TuP3, 18  
Amano, T.: PS+SE-FrM5, 26  
Anand, B.X.: EN+AS+EM+NS+SE+SS+TF-MoA1, 7  
Anders, A.: PS+2D+SE-WeM5, 20  
Antunez, P.D.:  
EN+AS+EM+NS+SE+SS+TF-MoM2, 1  
Archambault-Caron, M.: PS+SE-MoM9, 3  
Aretouli, K.E.:  
2D+EM+MG+NS+SE+SM+SS+TF-ThM5, 22  
Armstrong, S.: SE+PS-TuA2, 15  
Arndt, M.: SE+AS+NS+TR-MoM4, 5  
Ashfold, M.N.R.: PS+2D+SE-WeM3, **20**  
Aydil, E.S.: EN+AS+EM+NS+SE+SS+TF-MoA9, **8**  
Aydogan, P.: EN+AS+EM+NS+SE+SS+TF-MoM9, 2  
Azcatl, A.: PS+2D+SE-WeM12, **21**

## — B —

Bakoglidis, K.D.: PS+AP+SE-ThA9, **24**  
Balasubramanian, K.: SE+AS+NS+TR-MoM9, 6  
Barankova, H.: SE+PS+SM-TuM5, 12  
Bardos, L.: SE+PS+SM-TuM5, **12**  
Barnes, T.M.:  
EN+AS+EM+NS+SE+SS+TF-MoM10, 2  
Barroso, D.:  
2D+EM+MG+NS+SE+SM+SS+TF-ThM1, **22**  
Bartels, L.:  
2D+EM+MG+NS+SE+SM+SS+TF-ThM1, 22  
Bartis, E.A.J.: PS+SE-MoM5, 3  
Baxter, J.B.: EN+AS+EM+NS+SE+SS+TF-MoA5, 7; EN+AS+EM+SE+SS-TuM5, 10  
Beach, J.D.: EN+AS+EM+NS+SE+SS+TF-MoM10, 2  
Bearden, B.E.:  
EN+AS+EM+NS+SE+SS+TF-MoA1, 7  
Beier, O.: SE+PS+SM-TuM3, 12  
Benck, J.D.: EN+AS+EM+SE+SS-TuM3, 10  
Bhattacharya, P.: EN+EM+NS+SE+SS+TF-TuA4, 14  
Bilici, M.A.: PS+SE-MoM8, **3**  
Bluck, T.: SE+PS-TuA11, 17  
Boffard, J.: PS+AP+SE-ThA8, 24  
Bolt, P.J.: EN+AS+EM+NS+SE+SS+TF-MoM8, 1  
Bolvardi, H.: SE+AS+NS+TR-MoM2, 4  
Borget, E.:  
2D+EM+MG+NS+SE+SM+SS+TF-ThM2, 22  
Boyle, C.R.: PS+SE-MoM8, 3

Brenning, N.: PS+2D+SE-WeM10, 20  
Britto, R.: EN+AS+EM+SE+SS-TuM3, 10  
Brooks, A.:  
2D+EM+MG+NS+SE+SM+SS+TF-ThM1, 22  
Brown, D.W.: SE+PS-TuA11, 17  
Bultman, J.: PS+2D+SE-WeM11, 20  
Burghaus, U.:  
2D+EM+MG+NS+SE+SM+SS+TF-ThM10, 23

## — C —

Cairns, E.: EN+AS+EM+SE+SS-TuM13, 11  
Carlström, C.F.: SE+PS-TuA7, 16  
Cavallaro, A.: SE+PS+SM-TuM2, 12  
Chabal, Y.J.: EN+AS+EM+NS+SE+SS+TF-MoA1, 7  
Chagarov, E.:  
EN+AS+EM+NS+SE+SS+TF-MoM1, 1  
Chakthranont, P.: EN+AS+EM+SE+SS-TuM3, 10  
Chen, C.: EN+EM+NS+SE+SS+TF-TuA9, 14  
Chen, M.W.:  
2D+EM+MG+NS+SE+SM+SS+TF-ThM11, **23**  
Chen, Y.T.: PS+2D+SE-WeM13, 21  
Chen, Z.: EN+EM+NS+SE+SS+TF-TuA9, 14  
Chervin, C.N.: EN+EM+NS+SE+SS+TF-TuA7, 14  
Chessa, J.: SE-TuP4, 18  
Chintalapalle, R.V.:  
EN+AS+EM+NS+SE+SS+TF-MoA8, 8;  
SE-TuP4, 18  
Chirita, V.: SE+AS+NS+TR-MoM3, 4  
Choi, B.D.: EN+AS+EM+NS+SE+SS+TF-MoM6, 1  
Chong, K.S.L.: SE+PS+SM-TuM11, 13  
Clemens, B.M.: SE+EM+EN-MoA5, **9**  
Clendenning, S.: EN+EM+NS+SE+SS+TF-TuA9, 14  
Coley, W.:  
2D+EM+MG+NS+SE+SM+SS+TF-ThM1, 22  
Cormier, P.-A.: SE+EM+EN-MoA3, 8  
Crumlin, E.J.: EN+EM+NS+SE+SS+TF-TuA10, 15  
Cui, L.: SE+PS+SM-TuM4, **12**

## — D —

Dalmau-Mallorqui, A.:  
EN+AS+EM+SE+SS-TuM2, 10  
Daniel, R.: SE+PS+SM-TuM3, 12  
Dauskardt, R.H.: PS+SE-FrM8, 27; PS+SE-FrM9, 27; SE+PS+SM-TuM4, 12  
Dervaux, J.: SE+EM+EN-MoA3, 8  
Deutsch, T.: EN+AS+EM+SE+SS-TuM12, 11  
Dhayal, M.: PS+SE-FrM11, **27**  
Diercks, D.R.:  
EN+AS+EM+NS+SE+SS+TF-MoM10, 2  
Dimoulas, A.:  
2D+EM+MG+NS+SE+SM+SS+TF-ThM5, **22**  
Diroll, B.T.: EN+AS+EM+NS+SE+SS+TF-MoA5, 7  
Doeff, M.: EN+EM+NS+SE+SS+TF-TuA1, **14**  
Dong, S.: PS+SE-FrM8, **27**  
Doscher, H.: EN+AS+EM+SE+SS-TuM12, 11  
Dubois, G.: SE+PS+SM-TuM4, 12  
Dumcenco, D.:  
2D+EM+MG+NS+SE+SM+SS+TF-ThM11, 23

## — E —

Edström, D.: SE+AS+NS+TR-MoM3, **4**  
Ehiasarian, A.P.: SE+PS-TuA7, 16  
Eichfeld, S.M.:  
2D+EM+MG+NS+SE+SM+SS+TF-ThM6, 22  
Eichhorn, B.: EN+EM+NS+SE+SS+TF-TuA10, 15  
Empante, T.:  
2D+EM+MG+NS+SE+SM+SS+TF-ThM1, 22  
Eriksson, F.: SE+AS+NS+TR-MoM8, 5  
— F —  
Falta, J.:  
2D+EM+MG+NS+SE+SM+SS+TF-ThM12, 23  
Feng, H.: SE+EM+EN-MoA9, **9**  
Feng, P.X.-L.: PS+SE-MoM11, 4  
Flege, J.L.:  
2D+EM+MG+NS+SE+SM+SS+TF-ThM12, 23  
Fonctuberta i Morral, A.:  
EN+AS+EM+SE+SS-TuM2, 10  
Fong, K.D.: EN+AS+EM+SE+SS-TuM3, 10  
Fordham, J.L.:  
EN+AS+EM+NS+SE+SS+TF-MoA5, 7  
Förster, S.:  
2D+EM+MG+NS+SE+SM+SS+TF-ThM12, **23**  
Franz, R.: SE+PS-TuA10, **17**; SE-TuP7, 18  
Frau, E.: EN+AS+EM+SE+SS-TuM2, **10**  
Frijters, C.: EN+AS+EM+NS+SE+SS+TF-MoM8, 1

## — G —

Gagnon, H.: PS+SE-MoM9, 3  
Galindo, J.: EN+AS+EM+NS+SE+SS+TF-MoM5, 1  
Gall, D.: SE+AS+NS+TR-MoM9, 6  
Gapp, N.: SE+EM+EN-MoA4, 9  
Gardner, D.S.: EN+EM+NS+SE+SS+TF-TuA9, **14**  
Gaulding, E.A.:  
EN+AS+EM+NS+SE+SS+TF-MoA5, 7  
Ghosh, S.: PS+SE-MoM11, **4**  
Giamini, S.A.:  
2D+EM+MG+NS+SE+SM+SS+TF-ThM5, 22  
Ginger, D.S.: EN+AS+EM+NS+SE+SS+TF-MoA7, 7  
Glatz, S.A.: SE-TuP6, **18**  
Go, D.B.: PS+SE-MoM8, 3  
Gobina, E.: SE+PS+SM-TuM12, 13  
Grant, J.T.: SE+EM+EN-MoA7, 9  
Graves, D.B.: PS+SE-FrM6, 26  
Greber, T.:  
2D+EM+MG+NS+SE+SM+SS+TF-ThM12, 23  
Greczynski, G.: PS+AP+SE-ThA9, 24; SE+AS+NS+TR-MoM8, 5; SE+PS-TuA1, **15**  
Greene, J.E.: SE+AS+NS+TR-MoM3, 4; SE+PS-TuA1, 15  
Gudmundsson, J.T.: PS+2D+SE-WeM10, **20**  
Guertel, M.J.: SE+AS+NS+TR-MoM9, 6  
Guglietta, G.W.:  
EN+AS+EM+NS+SE+SS+TF-MoA5, 7  
Guillot, S.: EN+EM+NS+SE+SS+TF-TuA3, **14**  
Guo, J.-H.: EN+AS+EM+SE+SS-TuM13, 11  
Guo, Q.Y.: SE+AS+NS+TR-MoM10, **6**  
Gustafson, J.L.: EN+EM+NS+SE+SS+TF-TuA9, 14

## — H —

Hahn, C.J.: EN+AS+EM+SE+SS-TuM3, 10  
Hahn, R.: SE+AS+NS+TR-MoM11, 6  
Haight, R.A.: EN+AS+EM+NS+SE+SS+TF-MoM1, 1;  
EN+AS+EM+NS+SE+SS+TF-MoM2, 1  
Hammers, R.J.: EN+EM+NS+SE+SS+TF-TuA3, 14  
Hammer, R.:  
2D+EM+MG+NS+SE+SM+SS+TF-ThM12, 23  
Han, S.M.: SE+EM+EN-MoA4, 9  
Hannah, E.C.: EN+EM+NS+SE+SS+TF-TuA9, 14  
Hänninen, T.: SE+PS-TuA9, 16  
Hawranek, G.: SE+PS-TuA10, 17  
Hayes, G.: SE+EM+EN-MoA5, 9  
He, A.Y.: SE+PS+SM-TuM11, 13  
Hellstern, T.R.: EN+AS+EM+SE+SS-TuM3, 10  
Hemminger, J.C.: EN+AS+EM+SE+SS-TuM6, 11  
Henderson, W.A.: EN+EM+NS+SE+SS+TF-TuA4, 14  
Heo, S.: EN+AS+EM+NS+SE+SS+TF-MoM6, 1  
Hinkle, C.L.: PS+2D+SE-WeM12, 21  
Hodges, D.R.:  
EN+AS+EM+NS+SE+SS+TF-MoM5, 1  
Hofmann, T.: PS+SE-FrM7, 26  
Högberg, H.: SE+AS+NS+TR-MoM8, 5;  
SE+PS-TuA9, 16  
Holmlid, L.: EN+AS+EM+SE+SS-TuM1, 10  
Holtmannspötter, J.: PS+SE-FrM7, 26  
Holybee, B.: SE-TuP3, 18  
Holzwarth III, C.W.:  
EN+EM+NS+SE+SS+TF-TuA9, 14  
Hovish, M.Q.: PS+SE-FrM9, 27  
Hsieh, C.Y.: SE+PS+SM-TuM10, 13  
Hsieh, J.H.: SE-TuP1, 18; SE-TuP2, 18  
Hsu, C.C.: PS+SE-MoM6, 3  
Hu, J.: PS+2D+SE-WeM11, 20  
Huang, C.:  
2D+EM+MG+NS+SE+SM+SS+TF-ThM1, 22  
Huang, L.: SE+AS+NS+TR-MoM9, 6  
Huang, Y.H.: PS+SE-MoM6, 3  
Hubert, J.: SE+PS+SM-TuM1, 12  
Hultman, L.: PS+AP+SE-ThA9, 24;  
SE+AS+NS+TR-MoM3, 4;  
SE+AS+NS+TR-MoM8, 5; SE+PS-TuA1, 15; SE+PS-TuA9, 16  
Hunold, O.: PS+2D+SE-WeM13, 21

## — I —

Illiberi, A.: EN+AS+EM+NS+SE+SS+TF-MoM8, 1  
Itagaki, N.: PS+SE-FrM5, 26

## — J —

Jäger, E.: SE+PS+SM-TuM3, 12  
Jan, A.: SE+EM+EN-MoA5, 9  
Janakiraman, S.:  
EN+AS+EM+NS+SE+SS+TF-MoA6, 7  
Jantschner, O.: SE+PS+SM-TuM3, 12  
Jaramillo, T.F.: EN+AS+EM+SE+SS-TuM3, 10  
Jensen, J.: SE+PS-TuA9, 16  
Jin, W.: EN+EM+NS+SE+SS+TF-TuA9, 14  
Johnson, N.: EN+AS+EM+NS+SE+SS+TF-MoM9, 2  
Jones, J.G.: SE+EM+EN-MoA7, 9  
Ju, H.X.: EN+AS+EM+NS+SE+SS+TF-MoA7, 7; EN+AS+EM+SE+SS-TuM13, 11

## — K —

Kakalios, J.: EN+AS+EM+NS+SE+SS+TF-MoA9, 8

Kaminski, P.M.:  
EN+AS+EM+NS+SE+SS+TF-MoM11, 2  
Kang, H.J.: EN+AS+EM+NS+SE+SS+TF-MoM6, 1  
Kao, P.K.: PS+SE-MoM6, 3  
Kava, D.: EN+AS+EM+NS+SE+SS+TF-MoM5, 1  
Kawakami, S.: PS+AP+SE-ThA3, 24  
Kawase, A.: EN+AS+EM+SE+SS-TuM13, 11  
Kelaidis, N.:  
2D+EM+MG+NS+SE+SM+SS+TF-ThM5, 22  
Kelly, M.W.: PS+2D+SE-WeM3, 20  
Kibsgaard, J.: EN+AS+EM+SE+SS-TuM3, 10  
Kim, J.: 2D+EM+MG+NS+SE+SM+SS+TF-ThM1, 22  
Kim, M.J.: PS+2D+SE-WeM12, 21  
Kis, A.: 2D+EM+MG+NS+SE+SM+SS+TF-ThM11, 23  
Klee, V.:  
2D+EM+MG+NS+SE+SM+SS+TF-ThM1, 22  
Knoll, A.J.: PS+SE-MoM5, 3  
Kobayashi, Y.: PS+AP+SE-ThA3, 24  
Koga, K.: PS+SE-FrM5, 26  
Koller, C.M.: SE+AS+NS+TR-MoM11, 6;  
SE-TuP6, 18  
Kolozsvári, S.: SE+AS+NS+TR-MoM11, 6;  
SE-TuP6, 18; SE-TuP7, 18  
Konstantinidis, S.: SE+EM+EN-MoA3, 8  
Koyn, Z.: SE-TuP3, 18  
Kozen, A.C.: EN+EM+NS+SE+SS+TF-TuA11, 15  
Kudriavtsev, V.: SE+PS-TuA11, 17  
Kummel, A.C.:  
EN+AS+EM+NS+SE+SS+TF-MoM1, 1;  
EN+AS+EM+NS+SE+SS+TF-MoM2, 1  
Kwon, J.: EN+AS+EM+SE+SS-TuM6, 11

## — L —

Lai, Y.H.: SE-TuP2, 18  
Lanigan, D.: EN+AS+EM+NS+SE+SS+TF-MoA10, 8  
Lau, K.K.S.: EN+AS+EM+NS+SE+SS+TF-MoA6, 7; SE+PS+SM-TuM10, 13  
Lee, C.: 2D+EM+MG+NS+SE+SM+SS+TF-ThM1, 22  
Lee, C.S.: SE+PS+SM-TuM11, 13  
Lee, D.H.: EN+AS+EM+NS+SE+SS+TF-MoM6, 1  
Lee, H.I.: EN+AS+EM+NS+SE+SS+TF-MoM6, 1  
Lei, M.K.: SE+PS-TuA12, 17  
Leighton, C.: EN+AS+EM+NS+SE+SS+TF-MoA9, 8  
Leijten, T.: EN+AS+EM+NS+SE+SS+TF-MoA3, 7  
Lerche, M.: SE-TuP4, 18  
Lerouge, S.: PS+SE-MoM9, 3  
Lewin, E.: SE+AS+NS+TR-MoM1, 4  
Li, C.: SE-TuP2, 18  
Li, J.: EN+AS+EM+NS+SE+SS+TF-MoM10, 2  
Li, M.: EN+AS+EM+NS+SE+SS+TF-MoA9, 8  
Li, S.: EN+AS+EM+NS+SE+SS+TF-MoA5, 7  
Li, X.: SE+PS+SM-TuM11, 13  
Li, Y.L.: SE+EM+EN-MoA1, 8  
Liao, S.J.: SE-TuP2, 18  
Likhanskii, A.: PS+AP+SE-ThA8, 24  
Lin, C.C.: PS+AP+SE-ThA8, 24  
Lin, F.: EN+EM+NS+SE+SS+TF-TuA1, 14  
Lin, J.: SE+PS-TuA8, 16  
Lin, Y.C.: SE-TuP2, 18

Lin, Y.-C.:  
2D+EM+MG+NS+SE+SM+SS+TF-ThM6, 22  
Lindsay, A.: PS+SE-FrM6, 26  
Liu, L.-H.: EN+AS+EM+NS+SE+SS+TF-MoA1, 7  
Liu, Q.: EN+EM+NS+SE+SS+TF-TuA10, 15  
Liu, S.L.: SE-TuP1, 18  
Liu, Y.: EN+EM+NS+SE+SS+TF-TuA9, 14  
Löbel, T.: PS+SE-FrM7, 26  
Loke, Y.C.: SE+PS+SM-TuM11, 13  
Long, J.W.: EN+EM+NS+SE+SS+TF-TuA7, 14  
Lopez-Sanchez, O.:  
2D+EM+MG+NS+SE+SM+SS+TF-ThM11, 23  
Lu, D.: EN+EM+NS+SE+SS+TF-TuA4, 14  
Lu, I.: 2D+EM+MG+NS+SE+SM+SS+TF-ThM1, 22  
Lu, N.: PS+2D+SE-WeM12, 21  
Luan, P.: PS+SE-MoM5, 3  
Lucas, S.: SE+EM+EN-MoA3, 8  
Lundin, D.: PS+2D+SE-WeM10, 20  
Ly, N.: PS+AP+SE-ThA8, 24

## — M —

Malko, A.V.: EN+AS+EM+NS+SE+SS+TF-MoA1, 7  
Mankelevich, Y.A.: PS+2D+SE-WeM3, 20  
Manno, M.: EN+AS+EM+NS+SE+SS+TF-MoA9, 8  
Mares, P.M.: SE+PS-TuA3, 16  
Markus, I.: EN+EM+NS+SE+SS+TF-TuA1, 14  
Marquez-Velasco, J.:  
2D+EM+MG+NS+SE+SM+SS+TF-ThM5, 22  
Martens, R.L.: SE+AS+NS+TR-MoM10, 6  
Martinez, G.: SE-TuP4, 18  
Mayrhofer, P.H.: SE+AS+NS+TR-MoM11, 6; SE+AS+NS+TR-MoM4, 5;  
SE+AS+NS+TR-MoM5, 5; SE-TuP6, 18  
McGehee, M.D.:  
EN+AS+EM+NS+SE+SS+TF-MoA3, 7  
McLain, J.T.: SE+PS-TuA2, 15  
Meer, T.: PS+SE-FrM7, 26  
Meinel, K.:  
2D+EM+MG+NS+SE+SM+SS+TF-ThM12, 23  
Mendez Martin, F.: SE+PS-TuA10, 17  
Mertens, J.: SE+PS+SM-TuM1, 12  
Meysing, D.M.:  
EN+AS+EM+NS+SE+SS+TF-MoM10, 2  
Michael, M.K.: SE+EM+EN-MoA1, 8  
Minea, T.: PS+2D+SE-WeM10, 20  
Mitterer, C.: SE+PS+SM-TuM3, 12  
Mitzi, D.B.: EN+AS+EM+NS+SE+SS+TF-MoM1, 1  
Moon, B.K.: EN+EM+NS+SE+SS+TF-TuA9, 14  
Mork, F.: EN+AS+EM+NS+SE+SS+TF-MoA9, 8  
Moskovkin, P.: SE+EM+EN-MoA3, 8  
Mulligan, C.P.: SE+AS+NS+TR-MoM9, 6  
Muratore, C.: PS+2D+SE-WeM11, 20  
Murphy, N.R.:  
EN+AS+EM+NS+SE+SS+TF-MoA8, 8;  
SE+EM+EN-MoA7, 9  
Murray, C.B.:  
EN+AS+EM+NS+SE+SS+TF-MoA5, 7  
Music, D.: PS+2D+SE-WeM13, 21;  
SE+AS+NS+TR-MoM2, 4

## — N —

Naghbi, S.:  
2D+EM+MG+NS+SE+SM+SS+TF-ThM1, 22



- Naguib, M.:  
2D+EM+MG+NS+SE+SM+SS+TF-  
ThM3, **22**
- Nam, J.G.: EN+AS+EM+NS+SE+SS+TF-  
MoM6, **1**
- Nandasiri, M.I.: EN+EM+NS+SE+SS+TF-  
TuA4, **14**
- Nash, K.: SE-TuP3, **18**
- Nelson, C.: SE+EM+EN-MoA4, **9**
- Nguyen, A.:  
2D+EM+MG+NS+SE+SM+SS+TF-  
ThM1, **22**
- Nisol, B.: PS+SE-MoM9, **3**
- Nozawa, T.: PS+AP+SE-ThA3, **24**
- Nwogu, N.C.: SE+PS+SM-TuM12, **13**
- **O** —
- O'Brien, L.: EN+AS+EM+NS+SE+SS+TF-  
MoA9, **8**
- Oehrlein, G.S.: PS+SE-MoM5, **3**
- Oka, M.: PS+AP+SE-ThA3, **24**
- Olafsson, S.: EN+AS+EM+SE+SS-TuM1,  
**10**
- Oniszczyk, A.W.: SE+PS-TuA7, **16**
- Opasanont, B.: EN+AS+EM+SE+SS-TuM5,  
**10**
- Ozsdolay, B.D.: SE+AS+NS+TR-MoM9, **6**
- **P** —
- Pachicano, J.: SE-TuP3, **18**
- Pala, I.R.: EN+EM+NS+SE+SS+TF-TuA7,  
**14**
- Parameshwaran, V.: SE+EM+EN-MoA5, **9**
- Park, G.S.: EN+AS+EM+NS+SE+SS+TF-  
MoM6, **1**
- Park, J.B.: EN+AS+EM+NS+SE+SS+TF-  
MoM6, **1**
- Parker, J.F.: EN+EM+NS+SE+SS+TF-  
TuA7, **14**
- Patel, A.M.: EN+AS+EM+SE+SS-TuM5, **10**
- Patscheider, J.: SE+AS+NS+TR-MoM1, **4**
- Peeters, F.J.J.: PS+SE-MoM10, **4**
- Pena-Hueso, A.: EN+EM+NS+SE+SS+TF-  
TuA3, **14**
- Peng, W.N.: EN+AS+EM+NS+SE+SS+TF-  
MoA1, **7**
- Persing, H.: PS+AP+SE-ThA8, **24**
- Persson, P.O.A.: PS+2D+SE-WeM13, **21**
- Petrov, I.: SE+AS+NS+TR-MoM3, **4**;  
SE+PS-TuA1, **15**
- Pfuch, A.: SE+PS+SM-TuM3, **12**
- Piotrowicz, P.: PS+2D+SE-WeM2, **20**
- Pitchford, L.C.: PS+SE-MoM3, **2**
- Polcik, P.: SE+AS+NS+TR-MoM4, **5**;  
SE+PS-TuA10, **17**
- Poodt, P.: EN+AS+EM+NS+SE+SS+TF-  
MoM8, **1**
- Pouvesle, J.-M.: PS+SE-FrM10, **27**
- Preciado, E.:  
2D+EM+MG+NS+SE+SM+SS+TF-  
ThM1, **22**
- Prosa, T.J.: PS+AP+SE-ThA6, **24**
- **Q** —
- Qin, X.: PS+2D+SE-WeM12, **21**
- **R** —
- Rachbauer, R.: SE-TuP6, **18**
- Radovanov, S.: PS+AP+SE-ThA8, **24**
- Raman, P.: SE+PS-TuA2, **15**
- Ramiasa, M.: SE+PS+SM-TuM2, **12**
- Ramm, J.: SE+AS+NS+TR-MoM11, **6**
- Rebello de Figueiredo, M.: SE-TuP7, **18**
- Reese, M.O.: EN+AS+EM+NS+SE+SS+TF-  
MoM10, **2**
- Reeves, J.B.: SE+EM+EN-MoA5, **9**
- Rehbein, J.: PS+SE-FrM7, **26**
- Renau, A.: PS+AP+SE-ThA1, **24**
- Reniers, F.A.B.: SE+PS+SM-TuM1, **12**
- Rezek, J.R.: SE+PS-TuA3, **16**
- Riedl, H.: SE-TuP6, **18**
- Riposan, A.: SE+PS-TuA11, **17**
- Robert, E.: PS+SE-FrM10, **27**
- Robinson, J.A.:  
2D+EM+MG+NS+SE+SM+SS+TF-  
ThM6, **22**
- Rockett, A.: EN+AS+EM+NS+SE+SS+TF-  
MoM9, **2**
- Rolison, D.R.: EN+EM+NS+SE+SS+TF-  
TuA7, **14**
- Rubloff, G.W.: EN+EM+NS+SE+SS+TF-  
TuA11, **15**
- Rumphorst, R.F.: PS+SE-MoM10, **4**
- Ruzic, D.N.: PS+2D+SE-WeM2, **20**; SE+PS-  
TuA2, **15**
- **S** —
- Safriet, A.: PS+2D+SE-WeM11, **20**
- Saifullah, M.S.M.: SE+PS+SM-TuM11, **13**
- Sampat, S.C.:  
EN+AS+EM+NS+SE+SS+TF-MoA1, **7**
- Samuelsson, M.: SE+AS+NS+TR-MoM8, **5**
- Sana, C.O.: EN+AS+EM+NS+SE+SS+TF-  
MoM5, **1**
- Sangiiovanni, D.G.: SE+AS+NS+TR-MoM3,  
**4**
- Sankaran, R.M.: PS+SE-MoM11, **4**; PS+SE-  
MoM8, **3**
- Sardashti, K.: EN+AS+EM+NS+SE+SS+TF-  
MoM1, **1**;  
EN+AS+EM+NS+SE+SS+TF-MoM2, **1**
- Sarinont, T.: PS+SE-FrM5, **26**
- Sauter, A.J.: EN+AS+EM+NS+SE+SS+TF-  
MoA6, **7**
- Say, W.C.: SE-TuP1, **18**
- Schäfer, J.: PS+SE-FrM7, **26**
- Schmidt, J.: SE+PS+SM-TuM3, **12**
- Schmidt, S.: PS+AP+SE-ThA9, **24**; SE+PS-  
TuA9, **16**
- Schneider, J.M.: PS+2D+SE-WeM13, **21**;  
SE+AS+NS+TR-MoM2, **4**
- Schwarz, A.: EN+EM+NS+SE+SS+TF-  
TuA4, **14**
- Seidl, W.M.: SE+AS+NS+TR-MoM4, **5**
- Seo, H.: PS+SE-FrM5, **26**
- Shahriar, S.: EN+AS+EM+NS+SE+SS+TF-  
MoM5, **1**
- Shannon, S.: PS+SE-FrM3, **26**; PS+SE-  
FrM6, **26**
- Shchelkanov, I.A.: SE+PS-TuA2, **15**
- Shchelkanov, I.A.: PS+2D+SE-WeM2, **20**
- Shetty, A.: SE-TuP3, **18**
- Shiratani, M.: PS+SE-FrM5, **26**
- Shumlas, S.L.:  
2D+EM+MG+NS+SE+SM+SS+TF-  
ThM2, **22**
- Sivapragasam, N.:  
2D+EM+MG+NS+SE+SM+SS+TF-  
ThM10, **23**
- Smith, C.: SE+PS-TuA11, **17**
- Smolin, Y.Y.:  
EN+AS+EM+NS+SE+SS+TF-MoA6, **7**
- Snyders, R.: SE+EM+EN-MoA3, **8**
- Sorosh, M.: EN+AS+EM+NS+SE+SS+TF-  
MoA6, **7**
- Spange, S.: SE+PS+SM-TuM3, **12**
- Sproul, W.D.: SE+PS-TuA8, **16**
- Srivastava, S.: SE-TuP3, **18**
- Strongin, D.R.:  
2D+EM+MG+NS+SE+SM+SS+TF-  
ThM2, **22**
- Sugimoto, Y.: PS+AP+SE-ThA3, **24**
- Sun, L.: SE+EM+EN-MoA7, **9**
- Suzer, S.: EN+AS+EM+NS+SE+SS+TF-  
MoM9, **2**
- **T** —
- Tengdelius, L.: SE+AS+NS+TR-MoM8, **5**
- Thenuwara, A.C.:  
2D+EM+MG+NS+SE+SM+SS+TF-  
ThM2, **22**
- Thimsen, E.: EN+AS+EM+NS+SE+SS+TF-  
MoA10, **8**
- Thompson, G.B.: SE+AS+NS+TR-MoM10,  
**6**
- Tomialia, D.A.: EN+EM+NS+SE+SS+TF-  
TuA4, **14**
- Torregrosa, I.G.: EN+AS+EM+SE+SS-  
TuM5, **10**
- Trautmann, M.:  
2D+EM+MG+NS+SE+SM+SS+TF-  
ThM12, **23**
- Truscott, B.S.: PS+2D+SE-WeM3, **20**
- Tsipas, P.:  
2D+EM+MG+NS+SE+SM+SS+TF-  
ThM5, **22**
- Tsoutsou, D.:  
2D+EM+MG+NS+SE+SM+SS+TF-  
ThM5, **22**
- Turner, J.: EN+AS+EM+SE+SS-TuM12, **11**
- **U** —
- Ueda, H.: PS+AP+SE-ThA3, **24**
- Usrey, M.: EN+EM+NS+SE+SS+TF-TuA3,  
**14**
- **V** —
- van de Sanden, M.C.M.: PS+SE-MoM10, **4**
- Vandencastelee, N.: SE+PS+SM-TuM1, **12**
- Vargas, M.: EN+AS+EM+NS+SE+SS+TF-  
MoA8, **8**
- Vasilev, K.: SE+PS+SM-TuM2, **12**
- Ventzek, P.: PS+AP+SE-ThA3, **24**
- Vernisse, L.:  
2D+EM+MG+NS+SE+SM+SS+TF-  
ThM2, **22**
- Vivien, C.: PS+SE-FrM10, **27**
- Vlcek, J.V.: SE+PS-TuA3, **16**
- Voevodin, A.A.: PS+2D+SE-WeM11, **20**
- von Son, G.:  
2D+EM+MG+NS+SE+SM+SS+TF-  
ThM1, **22**
- Vukajlovic, J.: EN+AS+EM+SE+SS-TuM2,  
**10**
- **W** —
- Waite, A.R.: PS+2D+SE-WeM11, **20**
- Wallace, R.M.:  
2D+EM+MG+NS+SE+SM+SS+TF-  
ThM6, **22**; PS+2D+SE-WeM12, **21**
- Walls, J.M.: EN+AS+EM+NS+SE+SS+TF-  
MoM10, **2**;  
EN+AS+EM+NS+SE+SS+TF-MoM11,  
**2**
- Walter, J.: EN+AS+EM+NS+SE+SS+TF-  
MoA9, **8**
- Wan, L.: SE+AS+NS+TR-MoM10, **6**
- Wang, C.P.: EN+EM+NS+SE+SS+TF-  
TuA9, **14**
- Wang, Q.: PS+2D+SE-WeM12, **21**
- Wattendorf, M.D.:  
EN+EM+NS+SE+SS+TF-TuA7, **14**
- Wendt, A.E.: PS+AP+SE-ThA8, **24**
- Wertheimer, M.R.: PS+SE-MoM9, **3**
- Whitwick, M.B.:  
2D+EM+MG+NS+SE+SM+SS+TF-  
ThM11, **23**
- Widdra, W.:  
2D+EM+MG+NS+SE+SM+SS+TF-  
ThM12, **23**
- Wilt, D.M.: SE+EM+EN-MoA4, **9**
- Wolden, C.A.:  
EN+AS+EM+NS+SE+SS+TF-MoM10,  
**2**
- Womack, G.: EN+AS+EM+NS+SE+SS+TF-  
MoM11, **2**
- Wrobel, J.W.: SE+EM+EN-MoA1, **8**
- Wu, Y.L.: PS+2D+SE-WeM2, **20**

— **X** —

Xenogiannopoulou, E.:  
2D+EM+MG+NS+SE+SM+SS+TF-  
ThM5, 22  
Xia, A.: SE-TuP7, 18  
Xiao, J.: EN+EM+NS+SE+SS+TF-TuA4, 14

— **Y** —

Yang, R.: PS+SE-MoM11, 4  
Yang, R.B.: SE+PS+SM-TuM11, 13

Yang, Y.: PS+2D+SE-WeM5, 20  
Yang, Y.J.: PS+SE-MoM6, 3  
Ye, Y.F.: EN+AS+EM+SE+SS-TuM13, 11  
Young, J.: EN+AS+EM+SE+SS-TuM12, 11  
Yu, Y.: EN+EM+NS+SE+SS+TF-TuA10, 15

— **Z** —

Zhang, X.: EN+AS+EM+NS+SE+SS+TF-  
MoA9, 8  
Zhao, Z.: PS+SE-FrM8, 27

Zhou, X.: PS+2D+SE-WeM5, 20  
Zhu, H.:  
2D+EM+MG+NS+SE+SM+SS+TF-  
ThM6, 22  
Zhu, J.F.: EN+AS+EM+NS+SE+SS+TF-  
MoA7, 7; EN+AS+EM+SE+SS-TuM13,  
11  
Zorman, C.A.: PS+SE-MoM11, 4